# The Fluid Mechanics of Floating and Sinking

Dominic Joseph Robert Vella

Trinity College

*For the 'lady u like'*

# Preface

The research described in this thesis was performed in the Institute of Theoretical Geophysics, Department of Applied Mathematics and Theoretical Physics at the University of Cambridge between October 2004 and May 2007 and was supervised by Professor Herbert Huppert. No part of this thesis has been submitted for any qualification other than the degree of Doctor of Philosophy at the University of Cambridge.

This thesis is the result of my own work and includes nothing which is the outcome of work done in collaboration, except where specifically indicated in the text and acknowledgements.

The work described in this thesis is believed to be original, except where reference is made to the work of others. In particular, the results of sections 2.2, 2.5 and 3.4.1 constitute review material.

<div align="right">Cambridge, August 2007</div>

# ACKNOWLEDGEMENTS

First and foremost, I must express my gratitude to Herbert Huppert, my supervisor, for his helpful advice, many useful suggestions, and physical insight.

Many others have helped in various ways over the years: Paul Metcalfe's continual encouragement and technical support are particularly appreciated as is Robert Whittaker's willingness to talk about science. Thanks also go to Mahadevan for first suggesting I work on floating objects and to Ho-Young Kim for providing me with the experimental data presented in §2.3.

I am grateful to John Lister for supplying the numerical code he used to solve the viscous gravity current on a slope problem (Lister, 1992). A modified version of this code was used in Chapter 6 to study a gravity current in a porous medium above an impermeable sloping boundary.

Herbert Huppert, Paul Metcalfe, Anja Slim, Andrew Wells, and my parents have made many useful comments on earlier drafts of this thesis in its various incarnations. I have undoubtedly managed to introduce many more glitches since then.

The LaTeX style file used for this thesis is based on that supplied by Dirk Notz — thanks Dirk. As well as those already mentioned, I would like to thank all of the members of the ITG, past and present, who have made being here so rewarding.

On a more personal note, thanks to Julia Wolf (for making me lots of cups of chai), Chris Heaton (for making me realize that I'm not that good at squash) and, most importantly, Lydia Luke (for making me happy).

# Abstract

This thesis is concerned with the fluid mechanics of floating and sinking. More specifically, the majority of this thesis considers the role played by surface tension in allowing dense objects to float.

We first derive the conditions under which objects can float at an interface between two fluids. We obtain the conditions on density and size for various objects to float and show that being 'super-hydrophobic' does not generally help small, dense objects to float. Super-hydrophobicity does, however, dramatically reduce the energy required to remove an object from the interface. We then show that two floating objects can sink if they come into close proximity with one another. We extend this to show that a raft consisting of many interfacial objects can become arbitrarily large without sinking, providing that its density is below a critical value. Above this critical value, there is a threshold size at which sinking occurs.

We then consider the surface tension dominated impact of an object onto a liquid–gas interface. We determine a similarity solution, valid shortly after impact, for the shape of the interface and study the asymptotic properties of the capillary waves generated by impact. We also show how the interfacial deformation slows down the impacting body. We use a boundary integral simulation to study the motion at later times and determine the conditions under which the object either sinks or is trapped by the surface. We find that for an object of a given weight there is a threshold impact speed above which it sinks.

We study the waterlogging of a floating porous body as a model for the waterlogging of the pumice 'rafts' that often form on bodies of open water after a volcanic eruption. We study the inflow of water that is driven by capillary suction and hydrostatic pressure imbalances, and determine the time taken for this inflow to cause the object to sink.

Finally, we study the effects of a natural slope on the spreading of carbon dioxide sequestered into aquifers. We use laboratory models and numerical techniques to study the spreading of the resulting gravity current. Initially the current spreads axisymmetrically, while at later times it spreads predominantly along any slope in the overlying cap rock. We show that in industrial settings the time scale over which this asymmetry develops is typically a few years. This effect may have important practical implications since the current propagates faster in the asymmetric state.

# Summary of Frequently Used Quantities

| Variable | Meaning | Definition | Typical Value |
|---|---|---|---|
| $\alpha$ | time exponent | | 1 |
| $\beta$ | complex velocity potential | (4.28) | |
| | strip half-width | | |
| $\gamma, \gamma_{AB}$ | interfacial tension | | $0.0728 \ \mathrm{N\,m^{-1}}$ |
| $\delta, \delta', \epsilon$ | small quantity | | $\delta \ll \epsilon$ |
| $\varepsilon$ | numerical error | | |
| $\phi$ | interfacial inclination | figure 2.4 | |
| | porosity | | 0.8 |
| $\varphi, \Phi$ | velocity potential | | |
| $\psi$ | streamfunction | | |
| | angular position of contact line | figure 2.4 | |
| $\chi$ | indicator function on raft | (3.14) | |
| $\lambda$ | Lagrange multiplier | (3.13) | |
| $\mu$ | dynamic viscosity | | $1 \ \mathrm{mPa\,s}$ |
| $\nu$ | ratio of velocity scales | (6.21) | 1 |
| $\theta$ | contact angle | figure 2.2 | |
| | slope angle | figure 6.1 | $1°$ |
| $\rho, \rho_B$ | density of lower liquid | | $1 \ \mathrm{g\,cm^{-3}}$ (water) |
| $\rho_A$ | density of upper fluid | | $1 \ \mathrm{mg\,cm^{-3}}$ (air) |
| $\rho_s$ | density of solid object | | $8 \ \mathrm{g\,cm^{-3}}$ (steel) |
| $\tau$ | strip thickness | figure 3.3 | 0.5 mm |
| $\xi, \eta$ | rescaled $x, y$ co-ordinates | (4.17) | |
| $\Delta$ | centre–centre separation | figure 3.1 | |
| $\Pi \ (\Pi_e)$ | (effective) strength of surface tension | (5.4), (5.10) | |
| $d$ | depth of floating body | figure 5.2 | |
| $g \ (g')$ | (reduced) acceleration due to gravity | (6.5) | $9.81 \ \mathrm{m\,s^{-2}}$ |
| $k$ | permeability of a porous medium | | $10^{-9} \ \mathrm{m^2}$ |
| $\ell_c$ | capillary length | (2.7) | 2.7 mm |
| $l_s$ | strip length | | 7 cm |
| $m$ | mass per unit length | | |
| $n$ | exponent in governing equation | (6.24) | 1 (Darcy) |
| | | | 3 (lubrication) |
| $q$ | volume flux | (6.6) | |
| $t^*$ | time scale for asymmetric spreading | (6.7) | |
| $B$ | Bond number | (2.10) | |

| Variable | Meaning | Definition | Typical Value |
|---|---|---|---|
| $D$ | solid to liquid density ratio | (2.11), (5.8) | 2.3 (pumice) |
| $F$ | Froude number of impact | (4.10) | |
| $H(X,T)$ | deflection of interface | | |
| $H_0$ $(H_*)$ | height of object centre (contact line) | figure 2.4 | |
| $L$ | raft half-length | (3.23) | |
| | level of floating body in liquid | (5.15) | |
| $R_0$ | radius of object | | $R_0 \lesssim 1$ |
| $S$ | arc length | | |
| $T_s$ | time to reach sinking density | | |
| $V$ | downslope current speed | (6.8) | |
| $W$ | weight per unit length | (4.9) | |
| $W_A$ | work of adhesion | (2.28) | |
| $We$ | Weber number of impact | (4.1) | $We \lesssim 1$ |
| $X_n$ | downslope nose position | figure 6.1 | |
| $Y_{\max}$ | cross-slope current extent | figure 6.1 | |
| $\mathcal{A}$ | aspect ratio | | |
| $\mathcal{B}$ | bending stiffness of raft | (3.50) | |
| $\mathcal{C}$ | contour | | |
| $\mathcal{D}$ | density ratio of a thin strip | (3.8) | |
| $\mathcal{M}$ | modified strip density | (3.26) | |

# Contents

# Introduction

> Nature will bear the closest inspection.
> She invites us to lay our eye level with
> her smallest leaf, and take an insect view
> of its plain.
>
> *(Henry David Thoreau)*

## 1.1 Motivation

In both biology and engineering, small objects are commonly trapped at the interface between a liquid and a gas: insects walk on water, mineral ores are refined by froth flotation, and gas bubbles are prevalent at the surface of liquids. However, these trapped objects are rarely at rest. For example, over a period of time ranging from several seconds to minutes, long-lived bubbles floating in a glass of a sparkling drink spontaneously move towards one another and are pulled towards the edge of the glass (see figure 1.1).

The fluid mechanics that governs such systems is both interesting in its own right and important in a range of applications. Take, for example, the bubble rafts used by Bragg & Nye (1947) as a microscopic model for the atomic structure of crystals: there is an attractive interaction between the 'atoms' in a bubble raft (due to the deformation of the interface) and a short range repulsion, which arises from contact between the bubbles themselves (Nicolson, 1949). These forces are precisely those that govern the clustering of bubbles shown in figure 1.1. A bubble raft is little more than the surface of a sparkling drink, albeit with a better controlled bubble size.

1

**Figure 1.1:** *The interactions between bubbles floating at the surface of a glass of cider. Bubbles sufficiently near the wall of the glass cluster at the edge; the remainder cluster near the centre. Image taken by James Butler.*

More recently, attention has shifted to using these capillary interactions as a mechanism to drive self-assembly (see the reviews by Whitesides & Boncheva, 2002; Whitesides & Grzybowski, 2002, for example). The goal of this program is to be able to float a range of carefully designed components on the surface of water and allow their mutual attraction/repulsion to spontaneously assemble a much more intricate device. To date, this approach has been limited to exploring pattern formation in laboratory systems rather than manufacturing industrial components. In particular, the focus has been on the spontaneous formation of intricate patterns using small, chemically treated plates floating at a liquid–fluid interface. Figure 1.2 shows some examples of the patterns that can be formed relatively simply in such systems.

These experiments on capillary-driven self-assembly have generated a great deal of interest in the interactions between floating objects (see Mansfield *et al.*, 1997; Grzybowski *et al.*, 2001; Vella & Mahadevan, 2005, for example). Surprisingly, a much more natural question has, for the most part, been neglected: *when* can small objects float in the first place? For the purposes of self-assembly, this general question prompts several more specific questions: What size and density of object can float at an interface? Can a hydrophobic object float at higher densities than a hydrophilic object? Do the interactions between floating objects affect their ability to float?

In other applications, the presence of an object at the interface may be only temporary. In such situations, it is important to know the time scale for which the object can be
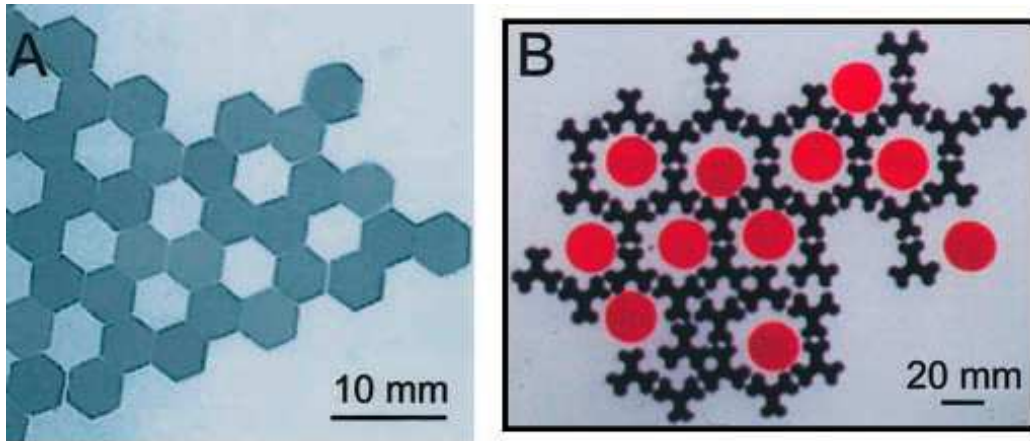
**Figure 1.2:** *Two-dimensional structures self-assembled using the capillary interactions between objects floating at the interface between perfluorodecalin ($C_{10}F_{18}$) and water. A: Hexagonal plates (dark blue) have been treated so that their edges are alternately hydrophilic and hydrophobic. The attractive interaction forces between hydrophilic edges dominate those between hydrophobic edges, leading to the formation of an open network (see Bowden* et al.*, 1997, for more details). B: More intricate patterns are formed by using a mixture of (red) circular plates and (black) shamrock-shaped plates (see Choi* et al.*, 2000, for more details). Images taken from Whitesides & Boncheva (2002).*

expected to remain at the interface: How long do the bubbles in a bath of molten glass persist before bursting? How quickly does a floating object become waterlogged and then sink?

Liquid–fluid interfaces are also important in the natural world, where many species of arthropod are able to walk on the surface of water (Bush & Hu, 2006). In nature, however, insects are seldom content to stand still on the interface and also test its dynamic strength by leaping around in fights for territory and mates. The resulting impacts with the surface are qualitatively different from those studied in the literature (Birkhoff & Zarantonello, 1957; Korobkin & Pukhnachov, 1988), which are unaffected by the surface tension of the interface. In these biological situations, the surface tension often dominates the inertial hydrodynamic forces generated by impact. It is therefore natural to ask when are impacting objects trapped by the surface? How high can a water-walking insect jump without piercing the surface?

Even insects that do not spend their entire life on the surface of water encounter its properties at some point during their life cycle. Mosquitoes, for example, lay their eggs at the surface of stagnant water (Christophers, 1945). When these eggs hatch, the larvae move to living just below the surface of the water. They breath using a siphon, which pierces the surface. In normal circumstances, their weight is supported by the surface tension force acting on this siphon; they dangle from the surface using the siphon. However, they often detach from the surface (Wigglesworth, 1966). The use of this siphon is therefore

subject to much the same physics as the floating and sinking of other objects and poses similar questions. This thesis is concerned with providing a framework for answering these questions by considering a number of straightforward and physically instructive situations.

## 1.2 Structure of the thesis

In this thesis we study the fluid mechanics of floating and sinking for bodies at the interface between a liquid and a lighter overlying fluid. We study a collection of problems in this area, focusing particularly on the role of the interfacial (or surface) tension.

Chapter 2 is devoted to the conditions under which a single object can float in equilibrium at a liquid–fluid interface. We begin by discussing the generalization of Archimedes' principle to incorporate the vertical force from surface tension (a result due to Keller, 1998). We then calculate conditions on the density and size for which a horizontal cylinder or a sphere will float at the interface. In particular, we quantify the extent to which small objects may be more dense than the underlying liquid and yet remain afloat because of the force contribution from surface tension. We also show that the surface properties of an object, its *hydrophobicity*, can only influence the conditions for floating in certain geometries. For example, a long, thin cylinder cannot support significantly larger loads if it is made more hydrophobic. A small sphere, on the other hand, can support larger loads if it is very hydrophobic. We also discuss the possible implications of this result for water-walking arthropods.

In Chapter 3 we extend our work on the flotation of a single object to consider the conditions for multiple objects to float at an interface. We show that the interaction between several floating bodies can jeopardize their ability to float: two small, dense objects may float when well separated but then sink as their separation is decreased. We then generalize the problem of two floating bodies by considering a continuum 'raft' of infinitely many touching strips and consider the conditions on the size and density of the raft for which floating is possible. Counter-intuitively, we show that, provided the raft density is below a threshold value, it may grow arbitrarily large without sinking. However, for raft densities above this threshold value, there is a critical size above which the raft cannot float and hence sinks.

Having explored floating in equilibrium in Chapters 2 and 3, the remainder of the thesis is concerned with the *dynamics* of sinking. In Chapter 4 we consider surface tension dominated impact. We study the model problem of a line mass impacting a liquid surface. For early times, the interfacial deformations caused by impact are described by a similarity solution allowing us to calculate the leading order slowing of the line mass. Using a

boundary integral simulation, we are able to follow the motion at later times until either the line mass sinks or it is trapped by the surface. We also quantify how the impact speed of a line mass can cause it to sink. We find that, for a given impact speed, there is a critical weight above which the mass sinks into the bulk fluid. Below this critical weight the mass is captured by the interface and floats.

In Chapter 5 we consider a much slower manifestation of sinking: the waterlogging of porous floating objects. This work is motivated by the observation that pumice fragments ejected during volcanic eruptions are frequently found floating in bodies of open water several months after the initial eruption. The most famous example of this was the 1883 eruption of Krakatoa in which pumice fragments were washed up on East African beaches many months later. We model the waterlogging process using the theory of flow in porous media and determine the time taken for the object to become sufficiently waterlogged to sink.

A very different manifestation of buoyancy and density differences is the subject of Chapter 6. We investigate the propagation of a gravity current in a porous medium at an inclined plane via a series of scaling analyses, numerical computations, and laboratory experiments. Under normal circumstances, we show that the current spreads axisymmetrically at short times but spreads predominantly downslope at later times. We determine the time scale over which this asymmetry develops and the relevant scalings for the extent of the current as a function of time. This asymmetry has potential implications for industrial applications, specifically for the geological storage of carbon dioxide in aquifers.

Finally, in Chapter 7, we summarize our findings and discuss some avenues for future research in these areas. We consider some interesting extensions to the problems discussed in the earlier chapters and also discuss how the techniques developed to date may be of use in related problems.

The theoretical development at the beginning of Chapter 3 relies on the concepts and notation developed in Chapter 2. Otherwise the chapters are self-contained and include an introduction to the relevant literature as well as a discussion putting our results into context.

# An Isolated Floating Object

[A dense Ebony chip] will float when it is coupled to so much air as to form with that a composite body less heavy than as much water as would fill the space which the said occupies in the water...

*(Galileo Galilei, Discourse on Floating Bodies, 1612)*

**Synopsis**

We consider the equilibrium floating of a two-dimensional horizontal cylinder and of a sphere at the interface between two fluids in the situation for which the objects are primarily supported by surface tension. We derive conditions on the density and radius of these objects for them to be able to float at the interface. We find that for a given object radius there is a maximum floating density and discuss the role played by the contact angle in determining this maximum density. For cylinders with a small radius compared to the capillary length, we find that the maximum floating density is independent of contact angle at leading order in the particle radius. However, for spheres the contact angle determines the maximum floating density at leading order in the particle radius. The theoretical predictions are found to be in good quantitative agreement with the experimental results of H.-Y. Kim and D.-G. Lee. These concepts suggest that water-walking arthropods may have evolved 'super-hydrophobic' legs to enable them to lift their legs clear of the water surface, rather than to support their weight.
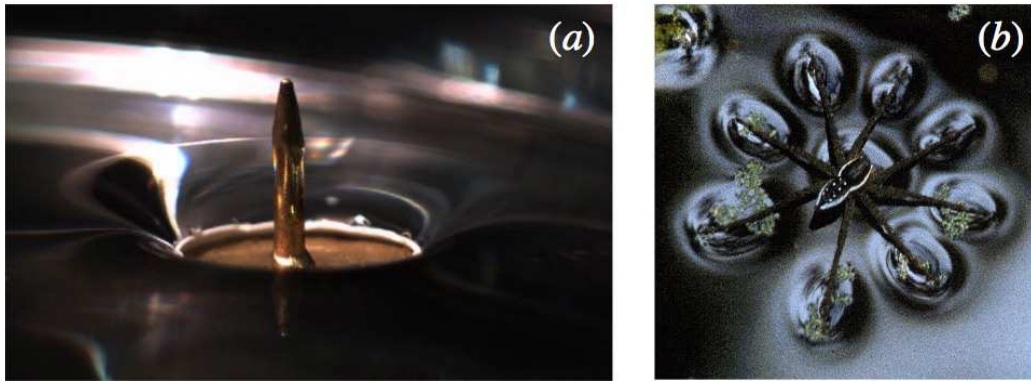
**Figure 2.1:** *The large deformations produced by interfacial objects. (a) The vertical component of surface tension is sufficient to balance the weight of objects much denser than the underlying liquid, such as an upturned drawing pin floating on water. (b) Large interfacial deformations allow creatures such as the water spider (*Dolomedes triton*) to walk on water (image courtesy of Robert B. Suter of Vassar College).*

## 2.1 Introduction

A common demonstration of the effects of surface tension is to float a metal drawing pin on water (see figure 2.1a). Even though the pin's density is much greater than that of water, it remains afloat because the vertical force contribution from surface tension is sufficient to balance its excess weight. This effect is exploited by water-walking arthropods, which rely on surface tension to support their weight (Bush & Hu, 2006). These creatures can cause very large interfacial deformations, as demonstrated by the specimen of the fishing spider *Dolomedes triton* pictured in figure 2.1b. In this chapter, we study how large these deformations can be in equilibrium by considering the question *what is the maximum load that an interface is able to support*?

Although it seems natural to investigate the conditions for which small, dense objects are able to float at a liquid-vapour interface, there has been little discussion of this problem in the literature. Most of the work in this area has focused on very small particles for which the weight of the particle is negligible in comparison to the surface tension force on the particle. In these situations, the particle may detach from the interface because of thermal fluctuations (Binks & Horozov, 2006), rather than sinking in the sense that interests us here.

A number of authors have considered the problem of equilibrium for various floating objects when gravity is important. Rapacchietta *et al.* (1977) and Rapacchietta & Neumann (1977) considered the equilibrium of a cylinder and a sphere, respectively, and observed that as the radius of an object decreases, the maximum density it can have without sinking increases. A similar observation was made by Hesla & Joseph (2004) for a circular disk.
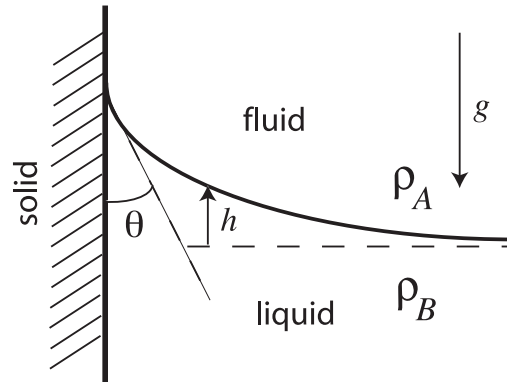
**Figure 2.2:** *Definition of the contact angle $\theta$, interface deformation $h$ and fluid densities $\rho_A$ and $\rho_B$.*

However, neither group explicitly calculated the maximum density that a floating object can have over a range of radii. Only Mansfield *et al.* (1997) determined this condition explicitly in their study of thin, two-dimensional strips.

In addition to the radius and density of an object, its surface properties might be expected to influence its ability to float. For our purposes, these surface properties are characterized by the contact angle between the solid and liquid–fluid interface (measured in the sense defined in figure 2.2). This angle is a property of the three phases that meet at the contact line and is denoted by $\theta$. The influence of the contact angle on the ability of a floating object to support a load has recently acquired particular significance after Gao & Jiang (2004) claimed that the impressive load bearing capacity observed in the legs of water striders (also known as pond skaters) is due to their 'super-hydrophobicity'. Here we present the first systematic study of this problem combining theoretical and experimental analyses.

This chapter is organised as follows. In §2.2 we discuss the generalisation of Archimedes' principle to incorporate the vertical force due to surface tension and reproduce a proof of this result due to Keller (1998). We then consider the equilibrium of an infinite cylinder floating horizontally at an interface in §2.3 and give conditions on its radius, density and contact angle for floating in equilibrium to be possible. We consider the same problem for a sphere in §2.4 and briefly discuss the stability of equilibrium in §2.5. In §2.6 we calculate the energy required to lift a horizontal cylinder clear of the interface and discuss the biological implications of our analysis before giving concluding remarks in §2.7.

A paper based on the work described in this chapter has been published in *Langmuir* (Vella, Lee & Kim, 2006*a*). The experimental results presented in §2.3 were obtained by Duck-Gyu Lee and Ho-Young Kim.

## 2.2 The contribution of surface tension

The quotation at the beginning of this chapter clearly shows that Galileo believed that small, dense objects could float because of the substantial volume of liquid displaced in what we now call the *menisci*. This hypothesis is easily rationalized because the liquid has no knowledge of the precise shape of the object away from the wetted surface. The liquid must therefore supply a vertical force equal to the total weight of displaced liquid, by the familiar Archimedes' principle. At the same time, the notion of an interfacial tension suggests that the vertical force supplied by the external liquid must be the result of this tension acting around the contact line. Keller (1998) was the first to show that these two physical pictures are, in fact, equivalent. Since our consideration of when objects can float will rely heavily on this equivalence, we repeat the proof given by Keller in this section.

Consider an irregularly shaped object floating at an interface, as in figure 2.3. The contact line, $\mathcal{C}$, is given in terms of arc length $s$ by $\boldsymbol{x} = \boldsymbol{r}(s)$ and the normal to the liquid interface (pointing from liquid to fluid) is $\boldsymbol{n}$. At the contact line, the surface tension $\gamma_{AB}$ acts perpendicular to both the normal to the interface and the tangent to the contact line. Summing the contributions of this force around the closed loop of the contact line, $\mathcal{C}$, we find that the total force on the object due to surface tension, $\boldsymbol{F}_{st}$, is

$$\boldsymbol{F}_{st} = \gamma_{AB} \int_{\mathcal{C}} \dot{\boldsymbol{r}}(s) \times \boldsymbol{n} \; \mathrm{d}s. \tag{2.1}$$

Since we shall be interested primarily in the vertical component of this force, we take the scalar product of (2.1) with the vertical unit vector, $\boldsymbol{k}$. Now, the projection of $\mathcal{C}$ onto the $x - y$ plane (denoted by $\mathcal{C}_{\pi}$) has inward pointing normal $\boldsymbol{\nu}$ and a different arc length, $s'$.
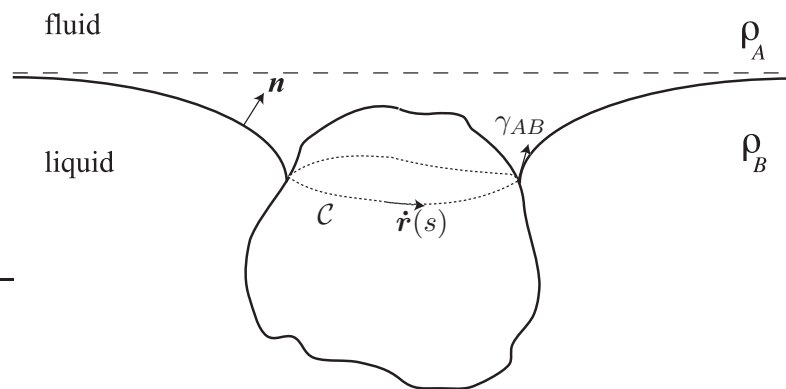


***Figure 2.3:*** *Schematic diagram of an irregularly shaped object floating at a liquid–fluid interface. The notation here is that used in the proof of the generalized Archimedes' principle. The contact line, $\mathcal{C}$, is given in terms of arc length $s$ by $\boldsymbol{x} = \boldsymbol{r}(s)$.*

Geometry then gives $\boldsymbol{k} \times \dot{\boldsymbol{r}} \, \mathrm{d}s = \boldsymbol{\nu} \, \mathrm{d}s'$ and so we have that

$$\boldsymbol{k} \cdot \boldsymbol{F}_{st} = \gamma_{AB} \int_{\mathcal{C}_\pi} \boldsymbol{n} \cdot \boldsymbol{\nu} \, \mathrm{d}s'. \tag{2.2}$$

Denoting the projection of the wetted surface onto the $x - y$ plane by $W_\pi$, the divergence theorem applied on $\mathbb{R}^2 \setminus W_\pi$ gives

$$\boldsymbol{k} \cdot \boldsymbol{F}_{st} = \gamma_{AB} \int_{\mathbb{R}^2 \setminus W_\pi} \boldsymbol{\nabla} \cdot \boldsymbol{n} \, \mathrm{d}A. \tag{2.3}$$

To progress further, we must relate $\gamma_{AB} \boldsymbol{\nabla} \cdot \boldsymbol{n}$, the curvature pressure due to surface tension, to the deflection of the contact line. In equilibrium, the curvature pressure is precisely balanced by the hydrostatic pressure in the liquid. If fluids of density $\rho_A$ and $\rho_B$ ($\rho_A < \rho_B$) meet at the interface, then the pressure just beneath the interface is $(\rho_A - \rho_B)gh$, where $h$ is the displacement of the interface from horizontal (see figure 2.2). Mathematically, the balance between the hydrostatic and curvature pressures may be expressed by the Laplace–Young equation (Finn, 1986)

$$(\rho_B - \rho_A)gh = -\gamma_{AB} \boldsymbol{\nabla} \cdot \boldsymbol{n}, \tag{2.4}$$

where $\boldsymbol{n}$ is the unit vector normal to the interface. Substituting this result into (2.3), we obtain

$$\boldsymbol{k} \cdot \boldsymbol{F}_{st} = -(\rho_B - \rho_A)g \int_{\mathbb{R}^2 \setminus W_\pi} h \, \mathrm{d}A. \tag{2.5}$$

Physically, (2.5) shows that the vertical force contributed by surface tension is simply the (modified) weight of liquid displaced in the menisci exterior to the object.

For small objects, such as the spider's legs shown in figure 2.1b, the vertical contribution of surface tension dominates the contribution from the more conventional Archimedean upthrust caused by the excluded volume of the body itself. However, for large, thin objects (such as the drawing pin of figure 2.1a) the situation is more subtle. In this case, there is also a substantial volume of fluid displaced directly above the object itself. It is a relatively simple matter to show that the vertical force contribution due to hydrostatic pressure, $\boldsymbol{k} \cdot \boldsymbol{F}_{hp}$, is given by

$$\boldsymbol{k} \cdot \boldsymbol{F}_{hp} = -(\rho_B - \rho_A)g \int_{W_\pi} h \, \mathrm{d}A, \tag{2.6}$$

which is simply the (modified) weight of water that would fill the hatched region in figure 2.4 for a circular cylinder lying horizontally at the interface. Combining this with the physical interpretation of (2.5), we see that the total vertical force acting on an interfacial object is indeed the modified weight of liquid that its presence at the interface displaces

— just as Galileo intuited.

The generalization of Archimedes' principle shows that the vertical surface tension force on an object can dominate the hydrostatic pressure force when the typical scale of the object is small compared to the length scale over which interfacial deformations decay. Interfacial deformations are governed by the Laplace–Young equation (2.4), which has an intrinsic length scale:

$$\ell_c \equiv [\gamma_{AB}/(\rho_B - \rho_A)g]^{1/2}. \tag{2.7}$$

The length scale $\ell_c$ is known as the *capillary length*. For a pure air–water interface $\ell_c \approx$ 2.7 mm. On this basis we expect that dense objects may float at an interface provided that their typical size $r_0 \lesssim \ell_c$. The remainder of this chapter is concerned with quantifying this concept and deriving the conditions for flotation.

## 2.3  A horizontal cylinder

We begin our discussion of flotation by considering a cylinder of radius $r_0$, density $\rho_s$, and infinite length floating horizontally at the interface between two fluids of densities $\rho_A$ and $\rho_B$ with $\rho_A < \rho_B$. The setup is shown in figure 2.4. This two-dimensional geometry makes the analysis of floating tractable and is also relevant in situations of practical interest, such as the experiments on water strider legs of Gao & Jiang (2004). To remain afloat, the cylinder must satisfy a condition of vertical force balance. In particular, its weight must be balanced by the total weight of fluid that it displaces, which depends on the interfacial



**Figure 2.4:** *Dimensional notation used for the problem of a single cylinder floating horizontally at the interface between two fluids. Dimensionless variables are represented by uppercase letters in the text.*

inclination, angular position and vertical height of the contact line, denoted by $\phi, \psi$ and $h_*$, respectively. This vertical force balance may be written

$$\pi(\rho_s - \rho_A)r_0^2 g = 2\gamma_{AB}\sin\phi + (\rho_B - \rho_A)gr_0^2\left(-2\frac{h_*}{r_0}\sin\psi + \psi - \sin\psi\cos\psi\right). \quad (2.8)$$

In (2.8), the left hand side represents the weight (per unit length) of the cylinder reduced by the weight of fluid A that it displaces. The right hand side of (2.8) represents the forces that counteract the weight of the cylinder: the vertical component of surface tension, $\gamma_{AB}$, (first term) and the modified weight of fluid B that would fill the hatched area in figure 2.4 (second term).

To pursue a systematic study of the conditions under which a cylinder may float, (2.8) must first be re-written in non-dimensional terms. Because we are interested in situations where both surface tension and gravity are important, it is natural to non-dimensionalize tensions by $\gamma_{AB}$ and lengths by the capillary length, $\ell_c$, as defined in (2.7). We shall use uppercase letters to denote non-dimensional versions of dimensional quantities so that $R_0 \equiv r_0/\ell_c$, $H_* \equiv h_*/\ell_c$ and so on. The force balance condition (2.8) can then be written as

$$\pi BD = 2\sin\phi - 2H_* B^{1/2}\sin\psi + B(\psi - \sin\psi\cos\psi), \quad (2.9)$$

where

$$B \equiv (\rho_B - \rho_A)gr_0^2/\gamma_{AB} = R_0^2 \quad (2.10)$$

is the *Bond number* of the cylinder and measures the relative importance of buoyancy to surface tension. Also,

$$D \equiv (\rho_s - \rho_A)/(\rho_B - \rho_A) \quad (2.11)$$

is the non-dimensional density of the cylinder measured relative to the exterior fluids.

Dividing (2.9) through by $\pi B$, we find an expression relating the density of a cylinder to its configuration, given by the three variables $\psi, H_*$ and $\phi$. This is convenient because we are able to eliminate two of these variables, $\psi$ and $H_*$ say, to give $D = D(\phi)$. From this expression, it is then straightforward to determine the maximum possible value of $D$ for given $B$ and $\theta$ simply by varying $\phi$.

To see that $D = D(\phi)$, we note first that the circular geometry of the situation ensures that

$$\psi = \phi + \pi - \theta \quad (2.12)$$

allowing us to eliminate $\psi$ easily. To eliminate $H_*$, we note that in two dimensions the Laplace–Young equation (2.4) reads

$$\frac{H_{XX}}{\left(1 + H_X^2\right)^{3/2}} = H. \quad (2.13)$$
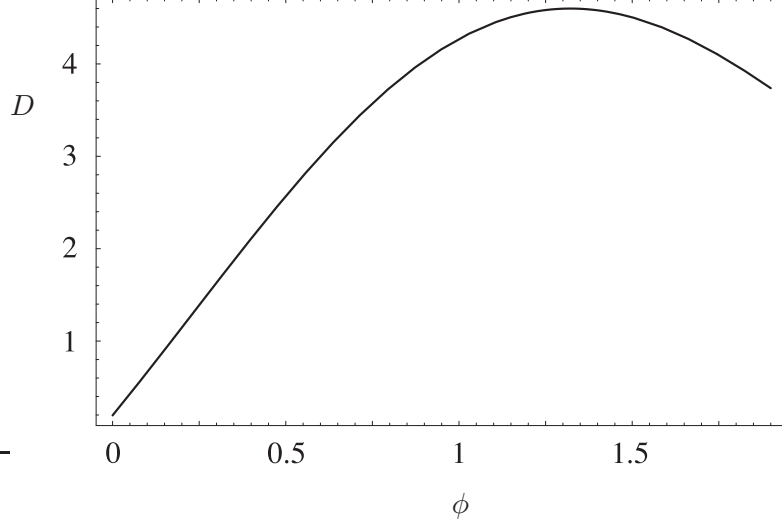
**Figure 2.5:** *Variation of D with the interfacial inclination, $\phi$. At some critical value of $\phi$, the cylinder density D is maximized; cylinders with a density larger than this must sink. Here, $B = 0.25$ and $\theta = 2\pi/3$.*

Integrating this equation once and using the boundary condition that $H(\pm\infty) = 0$, we find that

$$1 - \tfrac{1}{2}H^2 = \left(1 + H_X^2\right)^{-1/2}. \tag{2.14}$$

At the contact line this gives

$$\cos\phi = 1 - \tfrac{1}{2}H_*^2, \tag{2.15}$$

which may be interpreted physically as the horizontal force balance condition at the contact line (Mansfield *et al.*, 1997). For our purposes (2.15) is more conveniently written

$$H_* = -2\sin(\phi/2), \tag{2.16}$$

allowing us to eliminate $H_*$ from (2.9). Using (2.12) and (2.16) to eliminate $\psi$ and $H_*$ respectively, we find that

$$D(\phi) = \frac{2}{\pi B}\sin\phi - \frac{4}{\pi B^{1/2}}\sin\tfrac{\phi}{2}\sin(\phi-\theta) + \tfrac{1}{\pi}\left[\phi + \pi - \theta - \tfrac{1}{2}\sin 2(\phi-\theta)\right]. \tag{2.17}$$

Equation (2.17) gives the dimensionless cylinder density required to produce a certain interfacial inclination $\phi$ for given values of $\theta$ and $B$. As shown in figure 2.5, the function $D(\phi)$ has a maximum value, $D_{\max}$, for some $\phi = \phi_c$. Furthermore, $\phi_c < \pi/2$ so that the interface shape $h(x)$ is single-valued — the interface does not curve back on itself as is observed in models for the floating of a thin disk (Hesla & Joseph, 2004). A floating cylinder has this desirable property[1] because of its circular geometry. As $\phi$ increases

---

[1]It is desirable for the maximum density to occur for some $\phi_c < \pi/2$ since menisci that curve back on
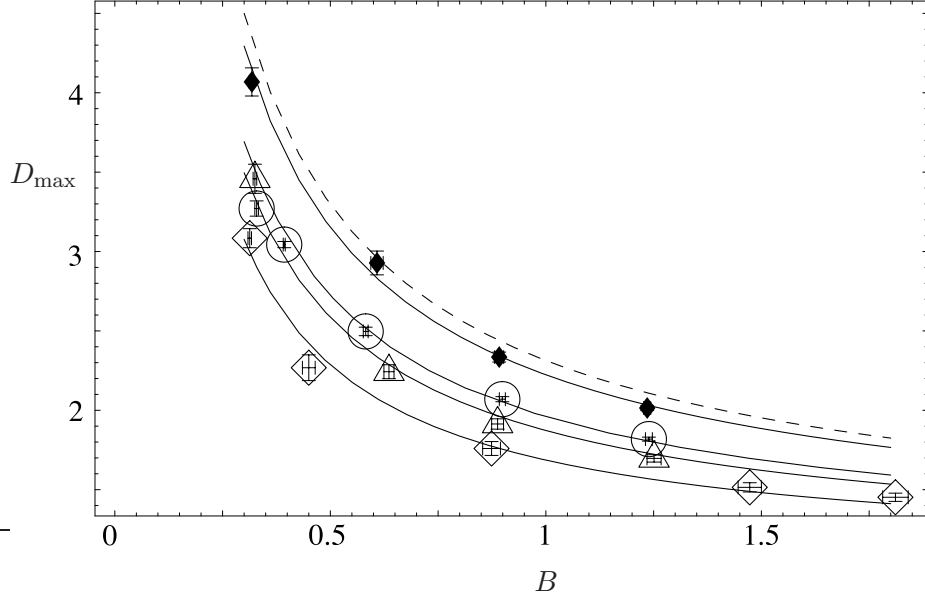
**Figure 2.6:** *Dependence of $D_{\max}$ on the Bond number, $B = R_0^2$, for cylinders with different values of the contact angle $\theta$. Theoretical predictions (solid lines) compare favourably with the experimental results of D.-G. Lee and H.-Y. Kim (points). $\theta = 72°$: $\diamond$, $\theta = 93°$: $\triangle$, $\theta = 104°$: $\bigcirc$, $\theta = 143°$: $\blacklozenge$. The dashed line shows the theoretical prediction for $\theta = 180°$.*

towards $\pi/2$, the contact line moves along the upper surface of the cylinder increasing $\psi$ and $|H_*|$ but decreasing $R_0 \sin \psi$. The product $H_* R_0 \sin \psi$ therefore has a minimum value at some point, and $D$ is forced to take a maximum value *before* the meniscus becomes vertical.

Instead of plotting $D(\phi)$, Rapacchietta *et al.* (1977) treated (2.17) as a quadratic equation for $R_0 = B^{1/2}$ and determined numerically $R_0(\phi)$ for given values of $D$ and $\theta$. They observed that $R_0(\phi)$ has a maximum and calculated this maximum for a few values of $\theta$ and $D$. Given the particularly simple form of (2.17), this seems an unnecessarily complicated approach. Here, we extend the work of Rapacchietta *et al.* (1977) by plotting the value of $D_{\max}$ as a function of $B$ for a variety of values of $\theta$, yielding the results shown in figures 2.6 and 2.7. These results are compared with the experimental measurements made by the group of H.-Y. Kim at Seoul National University in figure 2.6, and show good agreement between theory and experiment.

The experimental and theoretical results presented in figure 2.6 show that the effect of increasing the contact angle $\theta$ *is* measurable — for fixed $B$, increasing $\theta$ increases the maximum load that can be supported by a floating cylinder. However, for $B \ll 1$, the numerical results presented in figure 2.7 suggest that the influence of $\theta$ is negligible, provided that $\theta > \pi/2$. This is simple to understand physically. For small Bond numbers,

themselves ($\phi > \pi/2$) have not been observed experimentally and appear to be unstable.
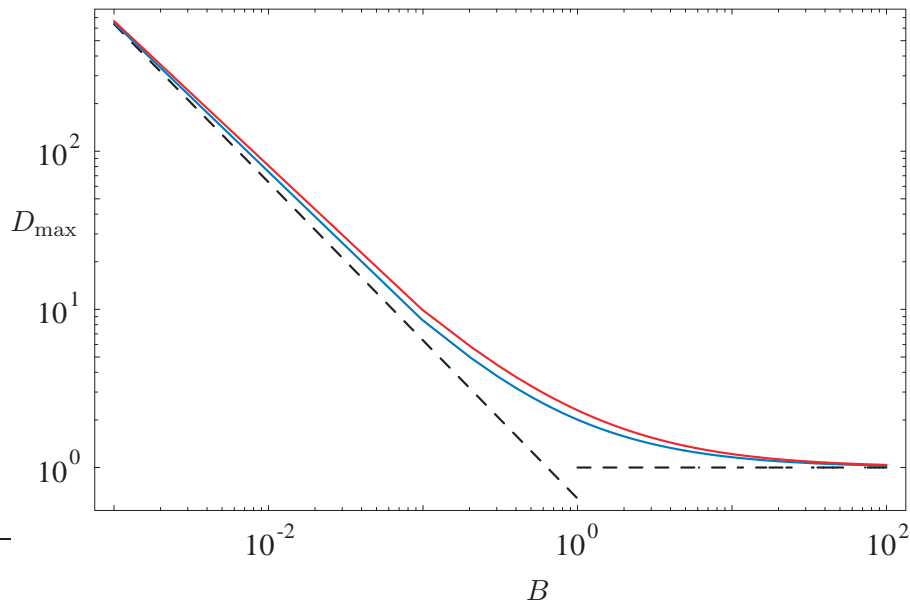
**Figure 2.7:** *Dependence of $D_{\max}$ on the Bond number, $B \equiv R_0^2$, for cylinders with two different values of $\theta$ over a wide range of Bond numbers. Theoretical predictions for $\theta = 109°$ (blue) and $\theta = 167°$ (red) compare well with the asymptotic results (2.18) for $B \ll 1$ and $D_{\max} \approx 1$ for $B \gg 1$ (dashed lines).*

the weight of liquid displaced in the excluded volume of the cylinder is small in comparison to the weight of liquid displaced in the exterior menisci. The restoring force is supplied almost exclusively by surface tension. The maximum vertical force supplied by surface tension is obtained when the interface is vertical at the contact line. We therefore expect that variations in the contact angle will vary the *position* of the contact line on the cylinder at this maximum but *not* the maximum force that can be generated by surface tension (as shown in figure 2.8), which is simply proportional to the length of the contact line (Hu, Chan & Bush, 2003). From this physical argument, or by considering (2.9), we find the asymptotic result that
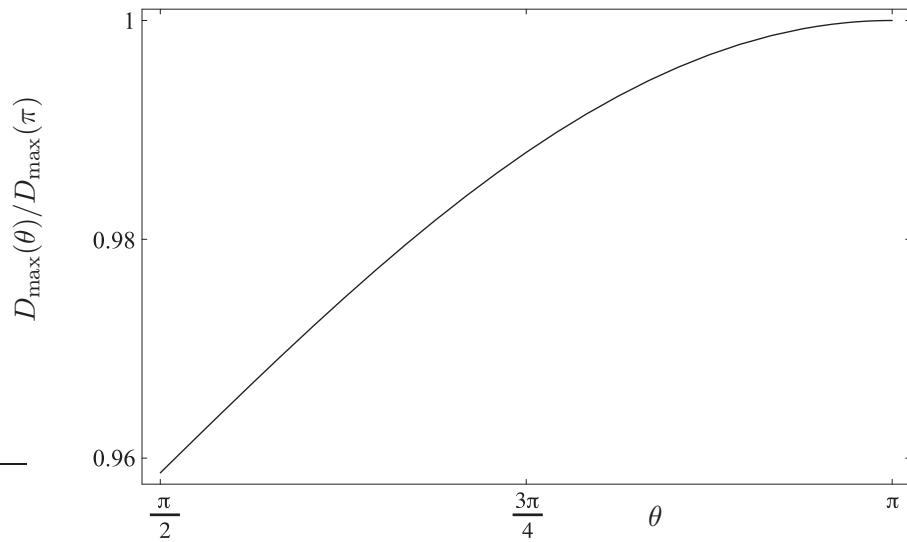
$$D_{\max} \approx 2/(\pi B), \tag{2.18}$$

for $B \ll 1$, which agrees well with the numerical results presented in figure 2.7.

This point is highlighted by figure 2.9, in which the maximum cylinder density is plotted as a function of $\theta$ for fixed $B = 10^{-3}$ (this value of $B$ is typical of a water strider leg). Figure 2.9 shows that as $\theta$ varies in the interval $[\pi/2, \pi]$ the maximum floating density varies by less than 5%.

Note that (2.18) is independent of $\theta$ but assumes that $\theta > \pi/2$. For $\theta < \pi/2$, there is no physical solution with a vertical meniscus: this would require $\psi \left(= 3\pi/2 - \theta\right) > \pi$ and the two contact lines on the cylinder to merge. Instead, the maximum vertical force is

$$\theta \approx \pi \qquad\qquad\qquad \theta \approx \pi/2$$
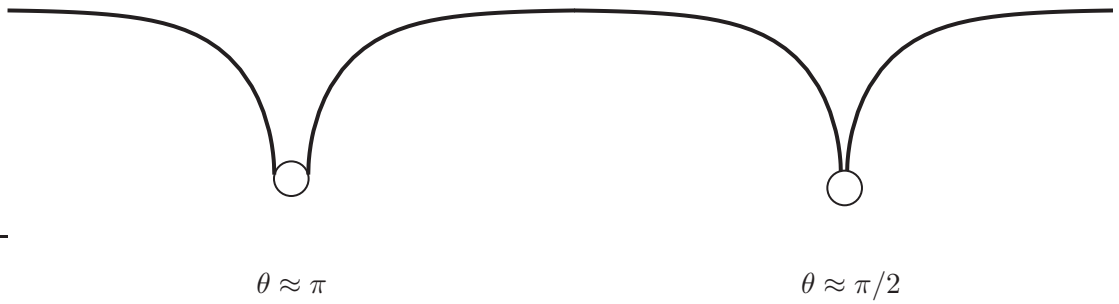
**Figure 2.8:** *For small cylinders, $B \ll 1$, the restoring force is provided almost exclusively by surface tension; the maximum being attained when the meniscus is vertical at the contact line. Therefore, the value of the contact angle $\theta$ does not significantly alter the maximum vertical force obtainable but merely the position of the contact line on the cylinder where this maximum is attained.*



**Figure 2.9:** *Dependence of $D_{\mathrm{max}}$ on the contact angle $\theta$ for $B = 10^{-3}$.*

obtained when $\psi = \pi$, so that $\phi = \theta$. This gives us the asymptotic result

$$D_{\max} \approx 2\sin\theta/(\pi B). \tag{2.19}$$

While the simple physical picture developed above is almost intuitive, it appears to be at odds with the conclusions of Gao & Jiang (2004). Gao & Jiang (2004) measured the force that a single water strider leg (for which $\theta \approx 167°$) can support without sinking. They then compared this to the force that can be supported by a glass fibre of similar dimensions (length 9 mm, radius $\sim 45$ $\mu$m), which was treated to render it non-wetting (in particular, the reported contact angle is $\theta = 109°$). While our analysis suggests that these two fibres should be able to support similar loads (see figures 2.7 and 2.9), Gao & Jiang (2004) found that the water strider leg could support a force of around 150 dynes while the glass fibre could support only 20 dynes. They attributed this difference to the large difference in contact angle between the two — at odds with our picture, from which one would expect both to be able to support a load of $\sim 140$ dynes. The theoretical prediction of 140 dynes is in reasonable agreement with experiments on the water-strider leg. It therefore seems that it is the poor supporting capability of the glass fibre that is anomalous and needs to be understood. For a fibre of these dimensions to support as little force as 20 dynes, the asymptotic result (2.19) suggests that it would have to have a contact angle of around 10°. Since untreated glass is generally highly hydrophilic, this simple estimate suggests that the discrepancy may have been due to an imperfection in the hydrophobic coating.

## 2.4 A sphere

The preceding analysis and physical argument suggest that the contact angle has only a limited influence on the weight or density of an object that can float at an interface. The complete picture is, however, more complicated. The importance, or otherwise, of the contact angle in fact depends on the geometry of the floating object. In this section, we show that even when $\theta > \pi/2$, the precise value of the contact angle can be of some consequence by considering the conditions for a sphere to float in equilibrium.

Balancing the sphere's weight with the vertical contribution of surface tension and the Archimedean upthrust we find that the vertical force balance condition for a sphere has the dimensional form

$$\frac{4\pi}{3}(\rho_s - \rho_A)r_0^3 g = (\gamma\sin\phi)(2\pi r_0\sin\psi) + (\rho_B - \rho_A)\Big[ \quad \frac{\pi}{3}r_0^3(2 - 3\cos\psi + \cos^3\psi)$$
$$- \pi h_*(r_0\sin\psi)^2\Big]. \tag{2.20}$$

In the right hand side of (2.20), the first term is the vertical force supplied by surface tension and the second term is the vertical force from hydrostatic pressure acting around the wetted perimeter of the sphere. Note that the vertical contribution from surface tension in this case depends on the length of the contact line, which is $2\pi r_0 \sin\psi$.

We may non-dimensionalize (2.20) as before, yielding

$$\tfrac{4}{3}DR_0^3 = 2R_0 \sin\psi \sin\phi + R_0^3 \left( -\frac{H_*}{R_0} \sin^2\psi + \tfrac{2}{3} - \cos\psi + \tfrac{1}{3}\cos^3\psi \right). \qquad (2.21)$$

In precisely the same manner as for the horizontal cylinder considered earlier, (2.21) may be considered as an equation for the density of the sphere, $D$, as a function of its position, parametrized by $H_*, \phi$ and $\psi$. The quantities $H_* = H(R_0 \sin\psi)$, $\phi$ and $\psi$ are again related via the meniscus shape at the contact line and geometry. While the geometrical relationship $\psi = \phi + \pi - \theta$ still holds, there is no analogue of the horizontal force balance condition (2.16). Instead, $H_*$ must be determined by solving the Laplace–Young equation for the interface shape $H(R)$. In the axisymmetric geometry appropriate here, this takes the form (Finn, 1986)

$$H = \frac{1}{R} \left( \frac{R H_R}{(1 + H_R^2)^{1/2}} \right)_R, \qquad (2.22)$$

where $()_R$ denotes differentiation with respect to $R$. Equation (2.22) is to be solved with the boundary conditions

$$H_R(R_0 \sin\psi) = \tan\phi, \qquad H(\infty) = 0. \qquad (2.23)$$

Since (2.22) does not admit a first integral in closed form, this problem was solved numerically using the MATLAB routine `bvp4c`. The resulting value of $H_*$ was then used to determine $D(\phi)$ for given values of $\theta$ and $R_0$. As in the cylindrical case, the analogue of $D(\phi)$ was also plotted by Rapacchietta & Neumann (1977). The behaviour of $D_{\max}$ for $R_0 \ll 1$ was also given, without discussion, by Scheludko *et al.* (1976). In figure 2.10 we present, for the first time, a plot of $D_{\max}$ over a wide range of values of $R_0$.

For $R_0 \ll 1$, we again expect that the weight of the sphere will be balanced almost exclusively by the vertical component of surface tension. However, we might reasonably worry about whether the value of $H_*$ decreases sufficiently rapidly for the term involving $H_*$ in (2.21) to be unimportant in this balance. These fears are alleviated by an asymptotic result derived by Lo (1983) in the context of determining the meniscus surrounding a vertical needle. Lo (1983) showed that for $R_0 \ll 1$

$$H_* \approx -R_0 \sin\phi \left( \Gamma_{em} + \log\frac{R_0 \sin\psi(1 + \cos\phi)}{4} \right), \qquad (2.24)$$
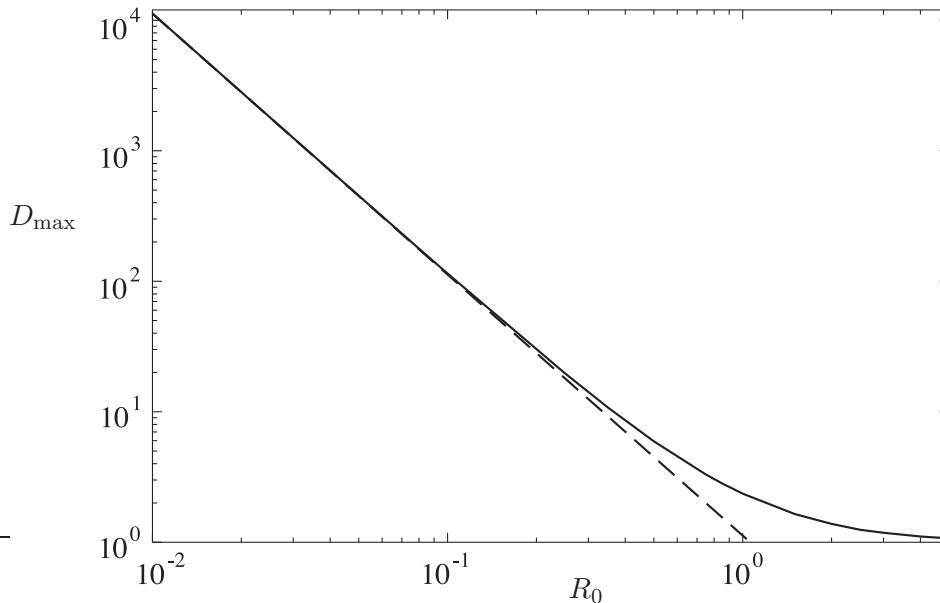
**Figure 2.10:** *The numerically determined dependence of the maximum sphere density, $D_{\max}$, on radius for a sphere with contact angle $\theta = 2\pi/3$. The dashed line shows the asymptotic result (2.26) for this value of $\theta$.*

where $\Gamma_{em} = 0.5772...$ is the *Euler-Mascheroni* constant. We may thus write

$$D(\phi) = \frac{3}{2R_0^2} \sin\phi \sin(\theta - \phi) + \mathcal{O}(\log R_0), \qquad (2.25)$$

which has a maximum value of

$$D_{\max} \approx \frac{3}{2R_0^2} \sin^2 \frac{\theta}{2} \qquad (2.26)$$

at $\phi = \theta/2$. This result agrees well with the numerical results shown in figure 2.10 and works equally well for other values of $\theta$. A result equivalent to (2.26) was given by Scheludko *et al.* (1976), though they did not discuss their result further.

The result in (2.26) is interesting because it is the leading order behaviour of $D_{\max}$ for $R_0 \ll 1$ and yet contains a $\theta$ dependence — even when $\theta > \pi/2$. This is in stark contrast to what we found for infinite length cylinders in §2.3, where a dependence on $\theta$ is only seen when $\theta < \pi/2$ or in the higher order corrections when $\theta > \pi/2$. Additionally, this maximum is attained when the meniscus makes an angle $\phi = \theta/2$ with the horizontal, in contrast to the near vertical deformation ($\phi = \pi/2$) that is typical of the maximum density cylinders. Both of these differences are consequences of the geometry in this situation: as the position of the contact line is varied, there is a competition between maximizing the inclination of the meniscus at the contact line (large values of $\phi$) and maximizing the contact line length (requiring $\psi \approx \pi/2$, i.e. $\phi \approx \theta - \pi/2$). This competition leads to the

selection of an intermediate value of $\phi$ at which $D$ is maximized, and so introduces some dependence on $\theta$. It is therefore entirely natural for the corresponding value of $D_{\max}$ to depend on $\theta$.

Finally, we note that this sensitivity to $\theta$ can be used as an experimental method for determining the contact angle of a material. Conventionally, such measurements are made optically, which is not practical for small objects. Instead, Preuss & Butt (1998) measured the force required to pull a 5 $\mu$m sphere from a surface using the tip of an atomic force microscope (AFM). From this force they were then able to infer (correct to within $1°$) the value of the contact angle, $\theta$.

## 2.5 Stability of equilibrium

For both cylinders and spheres, typical plots of the density as a function of the position (such as figure 2.5) show that for a given value of $D < D_{\max}$ there are, in general, two possible equilibrium configurations for a floating object. Given this scenario, we expect that one of these equilibria will be stable and the other unstable. This has previously been shown to be the case using calculations of the free energy of the objects (Rapacchietta *et al.*, 1977; Rapacchietta & Neumann, 1977). For completeness, we explain their result in physical terms using the ideas of force balance familiar from the preceding discussions and considering small displacements away from equilibrium based on the general form of figure 2.5.

We consider the two cases $\phi < \phi_c$ and $\phi > \phi_c$ in turn, where $D_{\max} = D(\phi_c)$. In the former case, $D'(\phi) > 0$ so that increasing $\phi$ slightly (which corresponds to pushing the object down into the liquid) increases the vertical force provided by the liquid, and the object is subject to a net vertical restoring force. Similarly, decreasing $\phi$ slightly decreases the vertical force that the liquid applies on the object and so its weight acts to return it to the equilibrium position. It is thus clear that this equilibrium position is *stable*. By repeating the above argument in the case where $\phi > \phi_c$, the reader will readily verify that this equilibrium position is *unstable* and therefore unobservable experimentally.

## 2.6 Lifting a leg out of water

In §2.3 I showed that the load bearing capacity of a thin cylinder is not significantly affected by the value of the contact angle, provided that $\theta > \pi/2$. It is therefore somewhat surprising that the legs of water striders are one of the most hydrophobic surfaces known,

with a typical contact angle of $\theta \approx 167°$ (Gao & Jiang, 2004). If such a high degree of hydrophobicity does not significantly reduce the chances of a stationary insect drowning, it is natural to ask *why are their legs so hydrophobic?* In this section I propose an answer to this question by showing that the energy required to remove a floating hydrophobic cylinder from an interface depends very sensitively on the contact angle of the cylinder: super-hydrophobic cylinders require relatively little work to remove them from an interface. This suggests that the very large contact angle of a water strider's legs may be an adaptation to facilitate walking and jumping on the surface of water.

### 2.6.1  A model calculation

We begin by again considering the cylinder pictured in figure 2.4. This time, a vertical force, $F_{\text{pull}}$, is applied to this cylinder in such a way that the cylinder is always in equilibrium: we imagine that the cylinder is lifted from the interface quasi-statically. For this to be the case, $F_{\text{pull}}$ must satisfy the vertical force balance condition, namely

$$F_{\text{pull}} = \pi BD - 2\sin\phi + 2H_*R_0\sin\psi - B(\psi - \sin\psi\cos\psi), \qquad (2.27)$$

where we retain the non-dimensional notation used in §2.3. The energy required to remove the cylinder from the interface, or *work of adhesion*, $W_A$ is then given by

$$W_A = \int F_{\text{pull}} \, \mathrm{d}H_0, \qquad (2.28)$$

where $H_0$ denotes the height of the cylinder's centre above the water surface. The limits of integration here are taken to be the value of $H_0$ for which $F_{\text{pull}} = 0$ and the value of $H_0$ for which $\psi = 0$ (where the two contact lines intersect at the base of the cylinder and the cylinder detaches from the surface). The integral in (2.28) is more easily computed by changing the integration variable to be the interfacial inclination, $\phi$. Using the relations $H_* = -2\sin(\phi/2)$ and $H_0 = H_* + R_0\cos\psi$ we have

$$W_A = \int_{\phi^*}^{\theta - \pi} F_{\text{pull}}(\phi) \left[ R_0 \sin(\phi - \theta) - \cos(\phi/2) \right] \, \mathrm{d}\phi. \qquad (2.29)$$

Here, $\phi^*$ is the interfacial inclination when the cylinder is freely floating, so that $F_{\text{pull}}(\phi^*) = 0$. The upper limit of integration in (2.29) corresponds to the detachment of the cylinder from the surface, which occurs when $\psi = 0$.

The integral in (2.29) may readily be evaluated numerically for different values of the Bond number $B$, density $D$ and contact angle $\theta$ of the cylinder. Figure 2.11 shows the dependence of $W_A$ on $\theta$ for a cylinder with values of $B$ and $D$ typical of a water strider
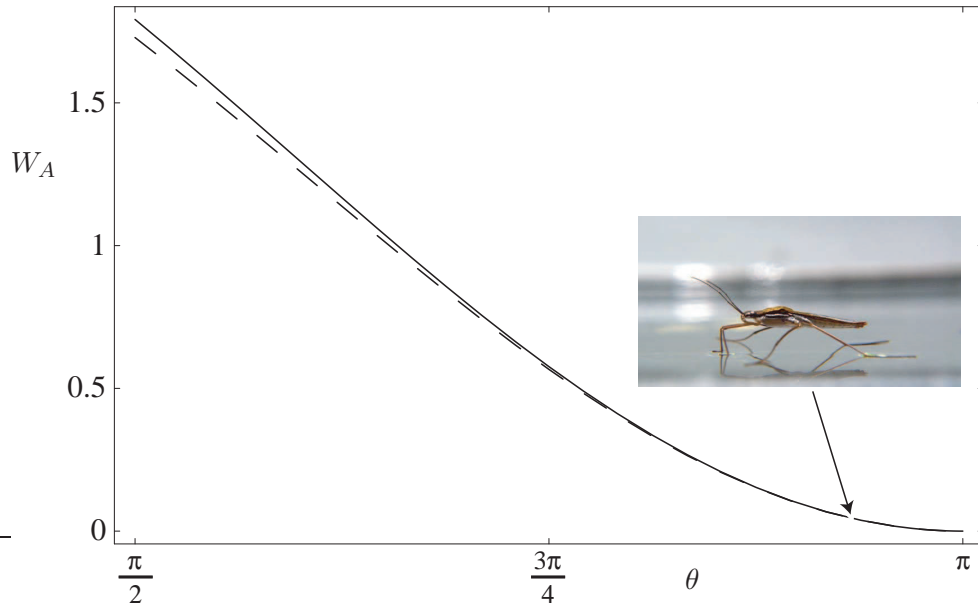
**Figure 2.11:** *The work per unit length required to remove a cylinder from an interface (or work of adhesion, $W_A$) as a function of the contact angle of the cylinder, $\theta$. The numerically computed values (solid line) compare favourably with the leading order asymptotics for $B \ll 1$ (2.30) (dashed line). Here $B = 10^{-3}$ and $D = 1.1$. The arrow illustrates the value of $\theta$ measured on the legs of water striders (Gao & Jiang, 2004). Image of water strider downloaded from:* `http://www-math.mit.edu/~ dhu/Striderweb/striderweb.html`.

leg. This demonstrates that the work of adhesion for a super-hydrophobic cylinder is much smaller than the work of adhesion for a cylinder with $\theta \approx \pi/2$.

For cylinders with small radius, $B \ll 1$, and $D = \mathcal{O}(1)$ the integral in (2.29) may be simplified considerably. To leading order in $B$ these simplifications give

$$W_A \approx \int_0^{\theta - \pi} (-2 \sin \phi) \times (-\cos(\phi/2)) \, \mathrm{d}\phi = \tfrac{8}{3} \left(1 - \sin^3 \tfrac{\theta}{2}\right), \qquad (2.30)$$

which compares very favourably with the numerical results plotted in figure 2.11.

### 2.6.2 Relevance to water striders

This section began with the question *why are the legs of water striders so hydrophobic?* It is therefore appropriate to consider whether the preceding model calculation helps to answer this question. From numerical evaluation of the integral (2.29) for $B = 10^{-3}$ and $D = 1.1$, we find that $W_A(167°) \leq 0.03 W_A(90°)$. In words, every time a water strider lifts one of its legs from the water surface, it makes an energy saving of over 97% by having $\theta = 167°$ rather than $\theta = 90°$. It is also interesting to note that the observed contact angle

occurs in the region where $W_A(\theta)$ flattens out (see figure 2.11), so that further increases in $\theta$ would only reduce $W_A$ slightly.

Given these observations, it seems that minimizing the energy required to remove a leg from the water's surface may be an evolutionary selection pressure driving water striders to develop super-hydrophobic leg coatings. However, this is only likely to be the case if a substantial amount of energy would be required to pull a leg with $\theta = 90°$ out of water. Using a typical wetted leg length of $l = 1.5$ cm (Hu *et al.*, 2003) and $\theta = 90°$, this energy is $w_A \sim 5 \times 10^{-6}$ J. To provide some sense of proportion, $w_A$ may be compared to the energy required for a water strider to jump. Typically, a water strider weighs $10^{-4}$ N and can jump to a vertical height of 5 cm (Hu, 2006). It seems reasonable to take the energy required for such a jump, $w_J \sim 5 \times 10^{-6}$ J, as an indication of the energy scale at which these insects operate. Now $w_A \sim w_J$ and the energy required to remove a leg from the water's surface is comparable to that expended in a jump. However, with $\theta = 167°$, $w_A \ll w_J$ and relatively little energy is expended in removing the insect's legs from the surface. From this simple analysis, it seems plausible that the evolutionary pressure driving insects to develop super-hydrophobic legs is, in fact, the energy required to remove their legs from the surface.

## 2.7 Discussion

In this chapter, we have quantified the conditions under which a single, isolated object may float at an interface. For a small two-dimensional object, the maximum force contribution that surface tension can supply is obtained when the meniscus is vertical, and so an object may float if its weight is less than $\gamma_{AB}$ times the contact line length. For axisymmetric objects the picture is more complicated because the contact line length depends on the position of the contact line on the object and hence on the interfacial inclination.

Much of the previous work in this area has been motivated by insects living at the air–water interface (Hu *et al.*, 2003; Gao & Jiang, 2004). However, these ideas may be more generally applicable in both biology and in the various engineering settings in which flotation finds application (Whitesides & Grzybowski, 2002). One interesting possibility is provided by the continual sinking motion of phytoplankton — small creatures that live beneath the surface of water. Since these marine organisms rely on photosynthesis (and hence light) as their energy source, it seems surprising that they are usually negatively buoyant. Vogel (2004) suggested that this negative buoyancy may be an evolutionary adaptation designed to prevent the individual phytoplankters becoming trapped by surface tension at the sea surface. While Vogel (2004) reports that the surface properties of these objects are not known, we may estimate their density on the basis of their reported sinking

speeds of $\sim 4$ $\mu\mathrm{m\,s^{-1}}$ and diameter of 10 $\mu$m. Assuming them to be spherical in shape, we estimate that $D \lesssim 1.07$ (similar to the value reported by Peperzak $et$ $al.$, 2003). This value is so close to unity that a sphere of this size and density would only be able to avoid becoming trapped at an interface if its contact angle $\theta \lesssim 0.2°$. Because this is such a small value, it seems very unlikely that the negative buoyancy of phytoplankton is an adaptation to ensure that they do not become trapped at the water surface.

# Equilibrium Conditions for Multiple Floating Objects

### Synopsis

We study the effect of interactions between objects supported at a fluid interface primarily by the interfacial tension. We show that two objects that float when well separated may sink as the separation between them is decreased. We then examine the equilibrium of a raft of thin strips floating at an interface, which may be thought of as the continuum limit of many touching, floating objects. We derive a governing equation for the shape taken by these rafts and consider the question of whether, for fixed raft density, there is a maximum spatial extent that a raft may have. We find that rafts of sufficiently low density may have infinite spatial extent, but that above a critical raft density, all rafts sink if they are sufficiently large. We compare our numerical and asymptotic results with some simple table-top experiments, and find good quantitative agreement.

## 3.1 Introduction

Although isolated objects may float at an interface because of the vertical force contribution from the meniscus, floating objects do not remain isolated for long. Indeed, the deformation of the interface that allows them to float also causes these objects to come into contact and form clusters — an effect that has been documented extensively (see, for example, Mansfield *et al.*, 1997; Kralchevsky & Nagyama, 2000; Vella & Mahadevan, 2005). These "capillary flotation forces" are important in practical settings such as the self-assembly of metallic components into macroscopic structures (Whitesides & Grzybowski, 2002). In this engineering setting an object should not only float when isolated at the interface but also after it has come into contact with other interfacial objects, and portions of the meniscus that support it have been eliminated.

In this chapter, we show how interactions between floating objects can lead to sinking via a series of model calculations that shed light on the physical and mathematical concepts at work in such situations. For simplicity, the calculations presented here are purely two-dimensional, though the same physical ideas apply to three-dimensional problems. In §3.2 and §3.3 we consider two different problems that illustrate how the interactions between two floating objects affect their ability to float. We then consider the continuum limit of many touching objects, together forming a flexible raft, in §3.4. We discuss how a non-zero bending stiffness alters the shape of such a raft as well as its ability to float in §3.5 and present some concluding remarks in §3.6.

A paper based on the work described in this chapter has been published in the *Journal of Fluid Mechanics* (Vella, Metcalfe & Whittaker, 2006c). Paul Metcalfe and Robert Whittaker were involved in discussions about this work.

## 3.2 Two horizontal cylinders

Perhaps the most natural way to characterize the effects of interaction is to ask how the maximum vertical load that can be supported by two floating cylinders varies as the distance between them is altered. In this section, we shall consider the maximum load rather than the maximum density to highlight the effect of varying the cylinder radius as well as the cylinder separation.

We consider two parallel cylinders of infinite length lying horizontally at the interface between two fluids of densities $\rho_A < \rho_B$, as shown in figure 3.1. We assume that these cylinders are non-wetting so that the contact angle satisfies $\theta > \pi/2$. Non-dimensionalizing lengths by $\ell_c$ and forces per unit length by $\gamma_{AB}$, we wish to determine the maximum weight
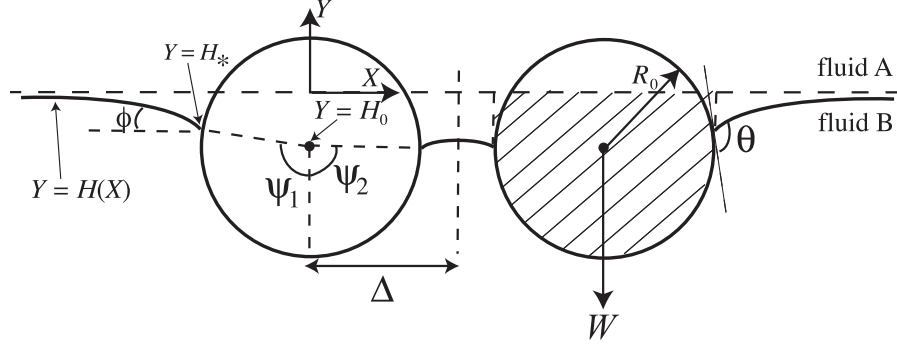
**Figure 3.1:** *Cross-section of two parallel, horizontal cylinders lying at an interface with a non-dimensional centre–centre separation of $2\Delta$. Each cylinder is subject to a non-dimensional vertical load $W$ per unit length.*

per unit length, $W$, that can be supported by each of two identical cylinders with radius $R_0$ and centre–centre separation $2\Delta$.

To remain afloat each individual cylinder must satisfy a condition of vertical force balance: their weight (or other load) must be balanced by the vertical contributions of surface tension and the hydrostatic pressure acting on the wetted surface of the cylinder. We assume that an external horizontal force is applied to the centre of the cylinders to maintain their separation distance and so do not consider the balance of horizontal forces explicitly. (By applying this force at the centre, there is then also no net torque on the cylinders.)

The force balance on each cylinder in this case is similar to the force balance on an isolated cylinder given by (2.9) in §2.3. However, because the situation is not symmetric about the centreline of the cylinder, we calculate the force exerted on each half of the cylinder separately. Using the notation of figure 3.1, the vertical force balance condition may be written $W = U_1 + U_2$, where

$$U_i \equiv -\sin(\theta + \psi_i) - H_0 R_0 \sin \psi_i + \tfrac{1}{2}R_0^2(\psi_i + \sin \psi_i \cos \psi_i) \quad (i = 1, 2), \qquad (3.1)$$

are the contributions to the vertical upthrust provided by the deformation on each half of the cylinder separately. $H_0$ is the height of the cylinders' centres *above* the undeformed free surface. Physically, the first term on the right hand side of (3.1) is the vertical component of surface tension. The second and third terms quantify the vertical resultant of hydrostatic pressure acting on the wetted perimeter of the cylinder, which is given by the weight of water that would fill the dashed area in figure 3.1. This is just the generalization of Archimedes' principle discussed in §2.2. Note that the difference in the third term of (3.1) when compared to (2.9) is a consequence of using $H_0(= H_* + R_0 \cos \psi_1)$ rather than $H_*$ in the second term of (3.1).

The angles $\psi_1$ and $\psi_2$ are determined by the interfacial shape, which is governed by the Laplace–Young equation (2.4). Just as for the isolated cylinder studied in §2.3, the

geometrical condition $\phi = \theta + \psi_1 - \pi$ and the horizontal force balance condition (2.16), allow $\psi_1$ to be eliminated from (3.1) in favour of $H_0(= H_* + R_0 \cos \psi_1)$ and $\theta$. However, (2.16) only holds when the meniscus extends to infinity — there is not an analogous result for the meniscus confined between the two cylinders. Instead, we must use numerical methods to determine $\psi_2$ for different values of $H_0$.

For the interior meniscus, I simultaneously obtained $\psi_2$ and the meniscus shape $H(X)$ by using the MATLAB routine `bvp4c` to solve the nonlinear eigenproblem

$$H_{XX} = H(1 + H_X^2)^{3/2},$$
$$H_X(R_0 \sin \psi_2) = \tan(\theta + \psi_2),$$
$$H(R_0 \sin \psi_2) = H_0 - R_0 \cos \psi_2,$$
$$H_X(\Delta) = 0,$$

$$(3.2)$$

on $[R_0 \sin \psi_2, \Delta]$, for given $H_0$, $R_0$ and $\Delta$.

With the angles $\psi_1$ and $\psi_2$ calculated, $W(H_0)$ can be determined from (3.1), and the maximum load that can be supported, $W_{\max}$, found numerically by varying $H_0$. Of particular interest is the dependence of $W_{\max}$ on the cylinder separation, which is shown for several values of the Bond number, $B$, in figure 3.2. This plot includes the limiting case $B = 0$, corresponding to the application of two line forces to the interface.

The results presented in figure 3.2 show that as the distance between the two cylinders decreases, the maximum vertical load that can be supported by each cylinder decreases. Physically, this result is intuitive since even though the interior meniscus is not completely eliminated in this instance, the vertical force that this meniscus can exert on the cylinder is diminished by the symmetry requirement $H_X(\Delta) = 0$: the meniscus cannot achieve so great a deflection at the contact line because it must be horizontal midway between the two cylinders. In particular, for small $B$ and $\Delta$ the total weight that can be supported by each cylinder is around half of that which can be supported by an isolated cylinder. This corresponds to the simple physical picture developed in Chapter 2: for small Bond number, the restoring force is supplied primarily by the deformation of the meniscus. When the interior meniscus is eliminated, the contact line length per cylinder, and hence the force that surface tension can provide, are halved. From this we expect that very dense objects that float when isolated at an interface might sink as they approach one another. Because floating objects move towards one another due to capillary flotation forces (see Mansfield *et al.*, 1997, for example), it seems likely that this effect may be ubiquitous for dense objects floating at an interface and may also have practical implications.

For $B = 0$ we can compute the asymptotic form of $W_{\max}$ for $\Delta \ll 1$ by noting that for small separations the interior meniscus has small gradients. The Laplace–Young equation (2.4) may then be approximated by $H_{XX} = H$, which has the solution $H(X) =$
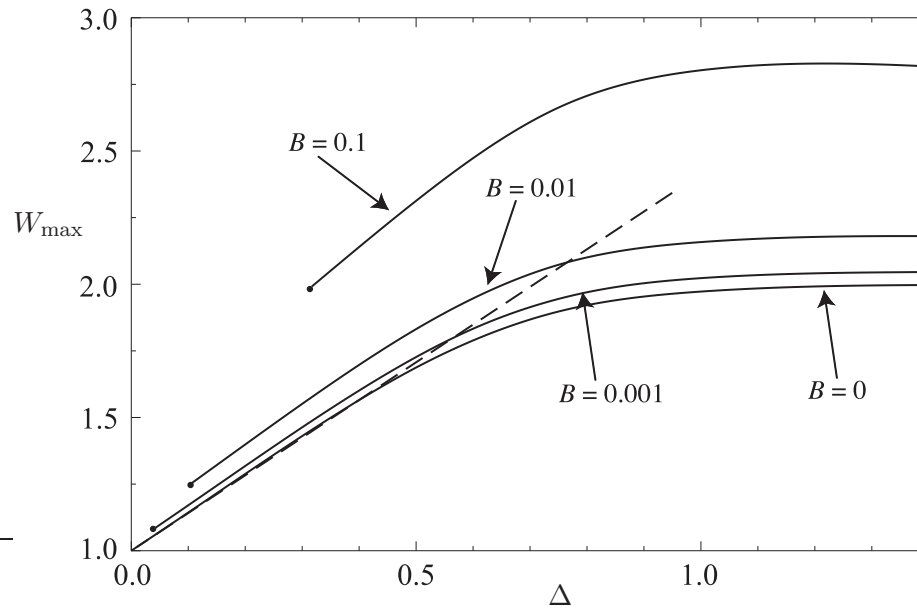
**Figure 3.2:** *Numerical results for the maximum load that can be supported by a single cylinder in the presence of another a distance $2\Delta$ away for several values of the Bond number, $B = R_0^2$. Here $\theta = 2\pi/3$. The dashed line shows the linear approximation (3.3) for the limiting case $B = 0$, valid when $\Delta \ll 1$. Note that the cylinders touch when $\Delta = B^{1/2}$: full circles in the graph indicate that the limit $\Delta \to B^{1/2}$ is not singular.*

$H_0 \cosh(X - \Delta)/\cosh\Delta$. Thus, the total vertical force provided by the menisci on each line force is

$$W = -H_0\big[\tanh\Delta + (1 - H_0{}^2/4)^{1/2}\big],$$

which is extremized when $(H_0{}^2 - 2)/(4 - H_0{}^2)^{1/2} = \tanh\Delta$. Choosing the real root of this quartic corresponding to a maximum in $W$ and making consistent use of $\Delta \ll 1$, $W_{\max}$ can be expanded as a series in $\Delta$ to obtain

$$W_{\max} = 1 + \sqrt{2}\Delta + \mathcal{O}(\Delta^2), \tag{3.3}$$

which compares favourably with the numerically computed results presented in figure 3.2.

## 3.3 Two touching strips

Although the scenario considered in the previous section may be relevant in practical situations, it does not lend itself to particularly simple experimental validation. To allow for such a comparison, we now consider the equilibrium of two infinitely long, shallow strips of dimensional thickness $\tau$, width $2b$, and density $\rho_s$, floating with their long edges in contact so that the interior meniscus is completely eliminated. These strips may tilt
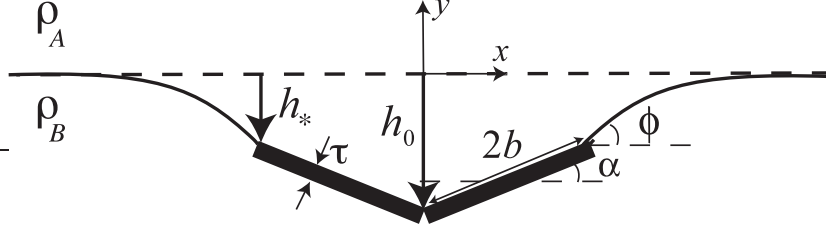
***Figure 3.3:*** *Cross-section of two shallow, touching strips floating at a liquid–fluid interface.*

at an angle $\alpha$ to the horizontal, as shown schematically in figure 3.3. The touching strips must each satisfy the vertical force balance condition to remain afloat. In dimensional terms, this requires that

$$2(\rho_s - \rho_A)g\tau b = \gamma \sin\phi - (\rho_B - \rho_A)g2b\cos\alpha\,[h_0 + b\sin\alpha]\,. \tag{3.4}$$

Here we are no longer bound by a contact angle condition, but instead assume that the meniscus is pinned to the uppermost corners of the strips. The strip's angle of inclination to the horizontal, $\alpha$, is determined by the balance of torques. (Singh & Hesla, 2004, show that this condition is satisfied automatically for shapes with circular cross-section and constant contact angle.) Equating moments about the point of contact (thereby eliminating the need to calculate the tension force that the strips exert on one another) and balancing vertical forces, we obtain the (dimensional) torque balance condition

$$2(\rho_s - \rho_A)gb^2\tau\cos\alpha = 2\gamma b\sin(\phi - \alpha) - (\rho_B - \rho_A)g\int_0^{2b}(h_0 + s\sin\alpha)s\,\mathrm{d}s. \tag{3.5}$$

Upon non-dimensionalizing lengths by $\ell_c$ and letting $\beta \equiv b/\ell_c$, the equilibrium conditions (3.4) and (3.5) become

$$\mathcal{D}\beta = \tfrac{1}{2}\sin\phi - \beta\cos\alpha(H_0 + \beta\sin\alpha), \tag{3.6}$$

$$\mathcal{D}\beta\cos\alpha = \sin(\phi - \alpha) - \beta(H_0 + \tfrac{4}{3}\beta\sin\alpha), \tag{3.7}$$

where

$$\mathcal{D} \equiv \frac{\rho_s - \rho_B}{\rho_B - \rho_A}\frac{\tau}{\ell_c} \tag{3.8}$$

is the appropriate ratio of the density of the strips to the densities of the surrounding fluids.

The approach we use to determine the maximum floating density $\mathcal{D}$ for a given strip width $\beta$ is similar to that used in our earlier analyses. After eliminating $\mathcal{D}$ between
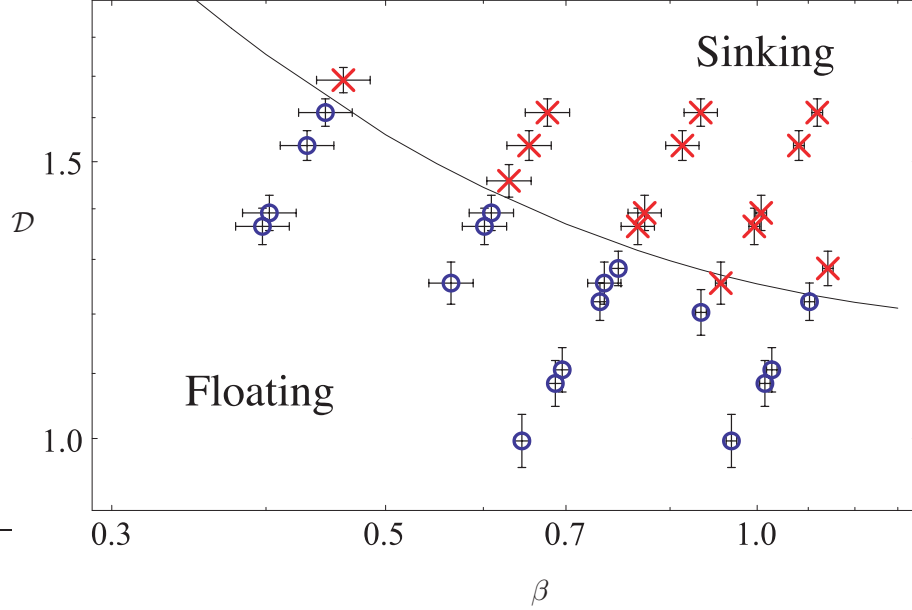
***Figure 3.4:*** *Numerically computed values of* $\mathcal{D}_{\max}$ *as the half-width of the strips,* $\beta$, *is varied (solid line). Experimental results (as described in text) are shown by red* $\times$ *(strips that sink) and blue* $\bigcirc$ *(strips that float). The vertical error bars represent an estimate for the error in the effective value of* $\mathcal{D}$ *caused by end effects, as discussed in the text.*

(3.6) and (3.7) and using the horizontal force balance condition (2.16) with the relation $H_* = H_0 + 2\beta \sin\alpha$ to eliminate $\phi$, we obtain a single equation for $\alpha$ given particular values of $\beta$ and $H_0$. Thus, for fixed $\beta$ and a given value of $H_0$, we may solve for $\alpha$ and deduce the corresponding value of $\mathcal{D}(H_0)$ from (3.6). By varying $H_0$ we are then able to calculate the maximum value of $\mathcal{D}$ for which equilibrium is possible. The numerical results of this calculation are presented in figure 3.4.

Also shown in figure 3.4 are experimental results showing points in $(\beta, \mathcal{D})$ parameter space for which two identical strips remained afloat or sank upon touching. I performed these experiments with strips of stainless-steel shim of length $l_s = 69\,\mathrm{mm}$ and thickness 0.4 or 0.5 mm, for which $\rho_s = 7905\,\mathrm{kg\,m^{-3}}$. These were floated on aqueous solutions of 0%, 10% or 25% methanol in air (so that $\rho_A \ll \rho_B$), allowing a wide range of values of $\beta$ and $\mathcal{D}$ to be probed. The strips were then allowed to come into contact naturally via the mutually attractive flotation force (Mansfield *et al.*, 1997). The data are plotted with horizontal and vertical error bars. The former indicate the uncertainty in the measurement of the strip widths. The latter indicate a simple estimate of the uncertainty in the additional vertical force contribution due to the menisci at the two strip ends (since the strips are of finite length). This contribution acts to decrease the effective density, $\mathcal{D}^*$, of the strips slightly, though it may be shown that

$$\mathcal{D}^* \gtrsim \mathcal{D} - \frac{2\ell_c}{l_s}, \tag{3.9}$$

where $l_s$ is the length of the strip. This estimate allows us to bound the contribution of surface tension acting at the ends and is used to produce the vertical error bars in figure 3.4.

As can be seen in figure 3.4, the agreement between our experiments and theory is generally very good. It seems likely that the small deviations might be caused by the dynamic nature of the experiment — since the strips are floated near to one another and then allowed to come into contact via the mutually attractive capillary forces, the system is *not* in equilibrium and so our static calculations are only of limited validity. Furthermore, elongated floating objects are subject to an instability by which small deviations from parallel grow in time: as the objects approach one another they 'zip up' rather than remain parallel (Vella *et al.*, 2004*b*). The experiment is therefore slightly three-dimensional in nature making accounting for such dynamic effects even more difficult.

## 3.4 The floating of a flexible raft

By adding additional strips to a floating pair of strips, a flexible raft is formed. An example of such a raft is shown in figure 3.5. Given the analysis of the preceding sections it is natural to expect that as the raft is lengthened in this manner, there will come a point where its weight (which scales with its total length) exceeds the force that can be supplied by surface tension (which is constant) and so the raft should sink. The situation is complicated by the fact that the raft bows in its middle, displacing a considerable amount of liquid in this region, as pointed out by Saif (2002). Apart from this qualitative description, Saif (2002) did not consider this problem in detail and so we now address the question of whether, for a raft of given weight per unit length, there is a maximum raft length before sinking occurs.

We tackle this problem by treating the raft as a two-dimensional continuum body, shown schematically in figure 3.6, and formulating an equation for the deformation of such a raft. This generalizes the linear analysis of Mansfield *et al.* (1997), which we briefly summarize below, and allows us to consider situations in which interfacial deformations are no longer small, including the existence of a threshold length for sinking. For simplicity, we neglect the intrinsic bending stiffness of the raft, although Vella *et al.* (2004*a*) have shown that interfacial rafts have some resistance to bending. We consider the effects of non-zero bending stiffness in §3.5.

### 3.4.1 Linear theory

The problem of determining the shape of a raft of small objects floating at an interface was considered briefly in the limit of small deformations by Mansfield *et al.* (1997). By requiring that the excess hydrostatic pressure balances the weight of the raft elements, they found that the raft shape is governed by

$$H_{XX} - H = \mathcal{D}, \tag{3.10}$$

where $\mathcal{D}$ is as defined in (3.8). This may be solved with the boundary condition that the raft should join smoothly onto the meniscus where they meet at $X = L$. The meniscus itself satisfies the linearized version of the Laplace–Young equation (2.4), so that the complete interfacial deformation is given by

$$H = \begin{cases} \mathcal{D}\big(e^{-L}\cosh X - 1\big), & |X| < L \\ H_* \exp(L - |X|), & |X| > L, \end{cases} \tag{3.11}$$
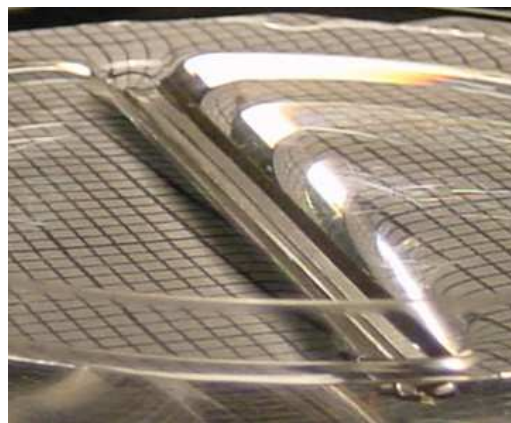
where

$$H_* = \frac{\mathcal{D}}{2}\big(e^{-2L} - 1\big) \tag{3.12}$$

is the height of the contact line.

### 3.4.2 Nonlinear theory

When deformations are no longer assumed to be small, two approaches may be used to determine a governing equation for the shape $\big[X(S), H(S)\big]$ of the raft and the surrounding meniscus as a function of arc length $S$. The first of these, a balance of forces argument, is



***Figure 3.5:*** *Photograph of a four-strip raft floating on water. Here the strips are made of stainless steel shim and are around* 7 cm *long and* 2 mm *wide.*
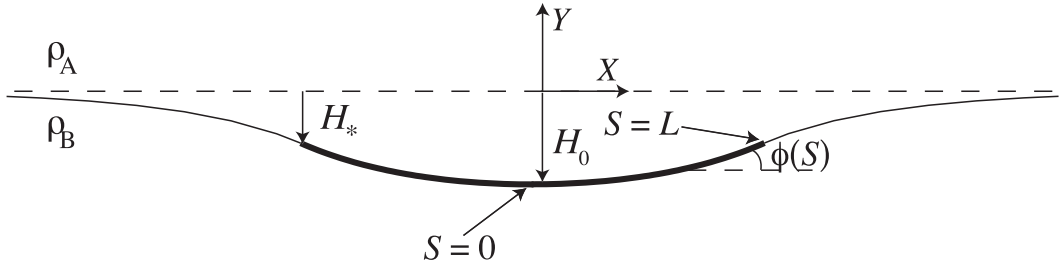
**Figure 3.6:** *Schematic illustration of a two-dimensional flexible raft floating at an interface.*

natural but relies on our assuming that the elements of the raft are able to exert a tension force upon one another — something that arises much more naturally from a variational approach. Here we use the latter approach, though the balance of forces argument is given in Appendix 3.A at the end of this chapter.

The variational principle states that raft shapes must minimize the energy of the system over variations in $H(S)$ and $X(S)$, subject to the constraint that $X_S^2 + H_S^2 = 1$ (which follows from the definition of arc length). Introducing a Lagrange multiplier $\lambda(S)$ associated with this constraint, we find that equilibrium raft shapes extremize

$$\mathcal{E} \equiv \int_{-\infty}^{\infty} \left\{ X_S(H^2/2 - 1) + \chi \mathcal{D}H + (1 - \chi) + \lambda(S)\left[(X_S^2 + H_S^2)^{1/2} - 1\right] \right\} \mathrm{d}S, \qquad (3.13)$$

where $\mathcal{D}$ was defined in (3.8) and

$$\chi(S) \equiv \begin{cases} 1, & |S| \leq L \\ 0, & |S| > L, \end{cases} \qquad (3.14)$$

is the indicator function of the raft.

The first two terms in the integral (3.13) correspond to the gravitational energy of the displaced fluid and the raft, the third term is the surface energy of the uncovered liquid area, and the final term ensures that the constraint $X_S^2 + H_S^2 = 1$ is satisfied. Note that a small increase in the distance between two infinitesimal raft elements such that $X_S^2 + H_S^2 > 1$ increases the energy of the system so that the Lagrange multiplier $\lambda(S)$ may be interpreted physically as the tension in the raft/meniscus. That the raft can support a tension at all may seem counterintuitive. It is a consequence of the attractive capillary interaction that would exist between two infinitesimally separated raft elements.

The requirement that $\mathcal{E}$ be stationary with respect to variations in $H(S)$ and $X(S)$ yields, via the Euler–Lagrange equation, the following differential equations for $X$ and $H$

$$HX_S + \chi\mathcal{D} - (\lambda H_S)_S = 0, \tag{3.15}$$

$$\left(\tfrac{1}{2}H^2 - 1 + \lambda X_S\right)_S = 0, \tag{3.16}$$

while variations with respect to $\lambda$ ensure that $(X_S^2 + H_S^2)^{1/2} = 1$. The differential form of this constraint, $X_S X_{SS} + H_S H_{SS} = 0$, allows us to eliminate $\lambda$ from (3.15) and (3.16) to give

$$\lambda_S = \chi\mathcal{D}H_S. \tag{3.17}$$

The boundary term at $S = \pm\infty$ gives $\lambda(\infty) = 1$, so that we may integrate (3.17) to give $\lambda = 1 + \chi\mathcal{D}(H - H_*)$. Substituting this into (3.15), and using $X_S = \cos\phi$ and $H_S = \sin\phi$, we find that raft shapes are given by the solution of the nonlinear eigenproblem

$$X_S = \cos\phi, \quad H_S = \sin\phi, \quad \phi_S = \frac{H + \mathcal{D}\cos\phi}{1 + \mathcal{D}(H - H_*)}, \tag{3.18}$$

$$X(0) = 0, \quad \phi(0) = 0, \quad \phi(L) = -2\arcsin(H_*/2), \quad H(L) = H_*,$$

as is also found via the balance of force argument given in Appendix 3.A. This system of equations was solved to find the raft shape and $H_*$ using the MATLAB routine `bvp4c`. The results of this computation may be verified by calculation of the quantity

$$P(\phi) \equiv \tfrac{1}{2}H^2 - 1 + \left[1 + \mathcal{D}(H - H_*)\right]\cos\phi, \tag{3.19}$$

which is conserved and equal to 0, as may be readily shown by considering the first integral of (3.16).

It is important to consider how the governing equation (3.18) compares to (3.10), which is valid in the limit of small deformations. For small deformations, we have that $\phi_S \approx H_{XX}$. Substituting this into (3.18) and linearizing the resultant, we recover (3.10). Mansfield *et al.* (1997) derived (3.10) to determine typical raft profiles. Here, we wish to determine whether a maximum raft length, $2L_{\max}$, exists and if so find its value for a raft of given density $\mathcal{D}$. To investigate this, small deformation theory is inadequate since sinking is an essentially nonlinear phenomenon.

Although the formulation in terms of arc length that we have used so far is convenient for numerical solutions of the governing equations (3.18), the formulation of the problem in Cartesian co-ordinates is also valuable. Substituting $\cos\phi = (1 + H_X^2)^{-1/2}$ into (3.19), we find that

$$H_X^2 = \left(\frac{1 + \mathcal{D}(H - H_*)}{1 - \tfrac{1}{2}H^2}\right)^2 - 1, \tag{3.20}$$

from which the symmetry of the raft about $X = 0$ immediately gives that

$$H_* = H_0 + \frac{H_0^2}{2\mathcal{D}} = \frac{1}{2\mathcal{D}}(H_0 + \mathcal{D})^2 - \tfrac{1}{2}\mathcal{D}, \tag{3.21}$$

where $H_0 \equiv H(0)$. This in turn ensures that $H_* \geq -\mathcal{D}/2$. The condition that $H_X^2$ be non-negative ensures that $H_0 \geq -\mathcal{D}$, so that the centre of the raft may extend down only to the level at which a raft element displaces its own weight in water; this is the neutral buoyancy level for the raft elements.

In the spirit of our earlier calculations, we treat $H_0$ and $\mathcal{D}$ as parameters giving rise to a particular raft semi-length $L(H_0, \mathcal{D})$. To calculate $L(H_0, \mathcal{D})$, we change variable from $S$ to $H$ in $L = \int_0^L \, dS$ giving

$$L = \int_{H_0}^{H_*} \frac{1 + \mathcal{D}(H - H_*)}{\left\{ \left[ 1 + \mathcal{D}(H - H_*) \right]^2 - \left[ 1 - \tfrac{1}{2}H^2 \right]^2 \right\}^{1/2}} \, dH. \tag{3.22}$$

Letting $H = H_0 + H_0^2 y / 2\mathcal{D}$, we find that

$$L(H_0, \mathcal{D}) = \frac{H_0^2}{2\mathcal{D}} \int_0^1 \frac{2 + H_0^2(y - 1)}{\left\{ \left[ 2 + H_0^2(y - 1) \right]^2 - \left[ 2 - (H_0 + yH_0^2/2\mathcal{D})^2 \right]^2 \right\}^{1/2}} \, dy. \tag{3.23}$$

Computation of the integral (3.23) allows us to consider the behaviour of $L$ for a given value of $\mathcal{D}$ as $H_0$ is varied and, in particular, to determine whether a maximum value of $L$ exists for that value of $\mathcal{D}$. We note that the integrand in (3.23) has an integrable singularity at $y = 0$. This singularity may be handled in numerical computations of $L$ by using the asymptotic result

$$H \approx H_0 + \frac{\mathcal{D} + H_0}{2 - H_0^2} X^2, \tag{3.24}$$

which is valid for $X \ll 1$.

Finally, we note that the tension at the midpoint of the raft is given by $1 - H_0^2/2$, so that the raft goes into compression if $H_0 \leq -\sqrt{2}$. Physically this is unrealistic, corresponding to a divergence in $\phi_S$ (or $H_X$). If $\mathcal{D} < \sqrt{2}$, this situation is avoided automatically since $H_0 \geq -\mathcal{D} > -\sqrt{2}$ but for $\mathcal{D} \geq \sqrt{2}$ we must consider this possibility. We therefore consider the two cases $\mathcal{D} < \sqrt{2}$ and $\mathcal{D} \geq \sqrt{2}$ separately.

### 3.4.3 The case $\mathcal{D} < \sqrt{2}$

When $\mathcal{D} < \sqrt{2}$, the centre of the raft may reach its neutral buoyancy depth $H_0 = -\mathcal{D}$ without going into compression. Numerical computation of the integral (3.23) suggests

that rafts grow arbitrarily long as $H_0 \searrow -\mathcal{D}$ (see figure 3.8). To show that this is the case, we consider the asymptotic behaviour of the integral (3.23) in the limit $\epsilon \equiv \mathcal{D} + H_0 \ll 1$. (Note that $\epsilon \geq 0$, since $H_0 \geq -\mathcal{D}$.) We then may write, to leading order in $\epsilon$,

$$L(\epsilon - \mathcal{D}, \mathcal{D}) \approx \frac{\mathcal{D}}{2} \int_0^1 \frac{2 + \mathcal{D}^2(y-1)}{\left\{ \mathcal{M}^2\mathcal{D}^2 y^2 + \mathcal{D}^4 y^3/2 - \mathcal{D}^4 y^4/16 + 4\mathcal{D}\epsilon\mathcal{M}^2 y \right\}^{1/2}} \, dy, \qquad (3.25)$$

where

$$\mathcal{M} \equiv (1 - \mathcal{D}^2/2)^{1/2}. \qquad (3.26)$$

This integral can be evaluated asymptotically by splitting the range of integration into two sub-regions $[0, \delta]$ and $[\delta, 1]$, where $\delta$ is unspecified save for the condition that $\epsilon \ll \delta \ll 1$ (see Hinch, 1990). This gives

$$L(\epsilon - \mathcal{D}, \mathcal{D}) \approx \int_\delta^1 \frac{1 + \mathcal{D}^2(y-1)/2}{\left\{ \mathcal{M}^2 y^2 + \mathcal{D}^2 y^3/2 - \mathcal{D}^2 y^4/16 \right\}^{1/2}} \, dy + \int_0^{\delta/\epsilon} \frac{\mathcal{M}\mathcal{D} \, du}{\left\{ \mathcal{D}^2 u^2 + 4u\mathcal{D} \right\}^{1/2}}$$

$$\equiv I_1 + I_2, \qquad (3.27)$$

where in $I_2$ we have used the substitution $y = \epsilon u$. Each of these integrals can be evaluated analytically and the results simplified using the assumption that $\epsilon \ll \delta \ll 1$ to give

$$\begin{aligned} I_1 = -\mathcal{M} \log \delta \quad &+ \quad \mathcal{M} \log \left( \frac{8\mathcal{M}^2}{\sqrt{2}\mathcal{M}(7 + \mathcal{M}^2)^{1/2} + 4 - \mathcal{D}^2} \right) \\ &- \quad 2\mathcal{D} \arctan \left( \frac{\mathcal{D}(3\mathcal{M} - \sqrt{2}(7 + \mathcal{M}^2)^{1/2})}{3\mathcal{D}^2 + \sqrt{2}\mathcal{M}(7 + \mathcal{M}^2)^{1/2}} \right) + \mathcal{O}(\delta) \qquad (3.28) \end{aligned}$$

and

$$I_2 = -\mathcal{M} \log \frac{\epsilon}{\mathcal{D}} + \mathcal{M} \log \delta + \mathcal{O}(\delta). \qquad (3.29)$$

Adding these results, the leading order terms in $\delta$ cancel, yielding:

$$\begin{aligned} L = -\mathcal{M} \log \left( \frac{\epsilon}{\mathcal{D}} \right) \quad &+ \quad \mathcal{M} \log \left( \frac{8\mathcal{M}^2}{\sqrt{2}\mathcal{M}(7 + \mathcal{M}^2)^{1/2} + 4 - \mathcal{D}^2} \right) \\ &- \quad 2\mathcal{D} \arctan \left( \frac{\mathcal{D}(3\mathcal{M} - \sqrt{2}(7 + \mathcal{M}^2)^{1/2})}{3\mathcal{D}^2 + \sqrt{2}\mathcal{M}(7 + \mathcal{M}^2)^{1/2}} \right). \qquad (3.30) \end{aligned}$$

This result is compared favourably with the numerical results in figure 3.7. In particular, notice that $L$ diverges logarithmically as $H_0 \searrow -\mathcal{D}$ (i.e. as $\epsilon \to 0$) so that rafts of arbitrary length are possible. It is also interesting to note that (3.30) may be inverted to give an
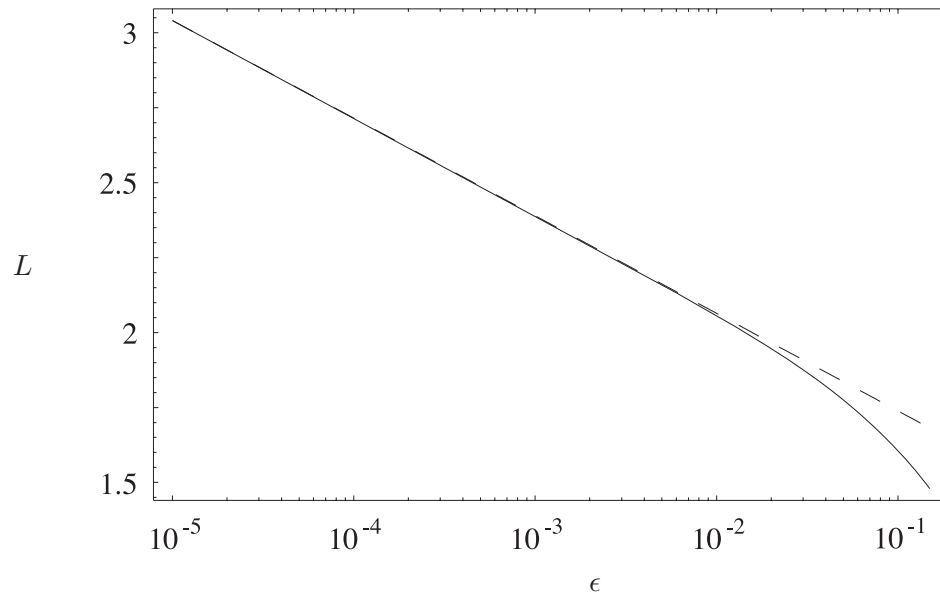
**Figure 3.7:** *Numerical results of the calculation of $L$ as a function of $\epsilon \equiv H_0 + \mathcal{D}$ (solid line) compared to the asymptotic result (3.30) for $\epsilon \ll 1$ (dashed line). Here $\mathcal{D} = 1.4$.*

estimate of $H_0 = -\mathcal{D} + \epsilon$ for given values of $\mathcal{D}$ and $L$ — a useful result when calculating raft shapes for large $L$.

That a raft of sufficiently low density can grow arbitrarily large in horizontal extent without sinking seems surprising at first. However, as new material is added to the raft, it may be accommodated at its neutral buoyancy level without the raft going into compression. Therefore, the ability of the raft to remain afloat is not jeopardized when new material is added and these low density rafts may grow arbitrarily long without sinking.

### 3.4.4 The case $\mathcal{D} \geq \sqrt{2}$

In this case, the raft cannot reach its neutral buoyancy level without going into compression, invalidating the argument just given to explain why, with $\mathcal{D} < \sqrt{2}$, rafts may be arbitrarily large. We thus expect that a maximum raft length does exist, and further, that the limiting raft has $H_0 = -\sqrt{2}$. Numerical computation of $L$ as a function of $H_0$ indicates that a critical half-length $L_{\max}$ does exist, but that it is not attained with exactly this value of $H_0$. Instead, there is a competition between the raft sinking deep into the liquid (to support its weight by increased hydrostatic pressure) and having its ends a large distance apart (i.e. lower pressure but over larger horizontal distances), and some compromise is reached. Given the abrupt change in behaviour observed as $\mathcal{D}$ increases past $\sqrt{2}$, we are particularly interested in the nature of this transition. My numerical computations suggested that for $\eta^2 \equiv \mathcal{D} - \sqrt{2} \ll 1$, $L_{\max}$ occurs when $H_0 = -\sqrt{2} + c\eta^2$

for some constant $c$. Motivated by this observation, we let $H_0 = -\sqrt{2} + c\eta^2$ and find, to leading order in $\eta$, that

$$L(c\eta^2 - \sqrt{2}, \sqrt{2} + \eta^2) \approx \int_0^1 \frac{y/\sqrt{2} + c\eta^2}{\left\{ 2c(c+1)\eta^4 y + (3c+2)\eta^2 y^2/\sqrt{2} + y^3/2 - y^4/16 \right\}^{1/2}} \, dy. \tag{3.31}$$

This integral may also be evaluated by splitting the domain of integration into two regions $[0, \delta']$ and $[\delta', 1]$ where $\eta^2 \ll \delta' \ll 1$. This gives

$$L \approx \int_{\delta'}^1 \frac{y \, dy}{\left\{ y^3 - y^4/8 \right\}^{1/2}} + \eta \int_0^{\delta'/\eta^2} \frac{(c + u/\sqrt{2}) \, du}{\left\{ u^3/2 + (3c+2)u^2/\sqrt{2} + 2c(c+1)u \right\}^{1/2}}$$

$$\equiv I_1 + \eta I_2, \tag{3.32}$$

where in $I_2$ we have used the substitution $y = \eta^2 u$. The integrals $I_1$ and $I_2$ can be evaluated analytically and expanded to give their leading order dependence on $\delta'$:

$$I_1 = 2\sqrt{2} \arctan\left( \frac{\sqrt{7}}{3} \right) - 2\delta'^{1/2} + \mathcal{O}(\delta'^{3/2}), \tag{3.33}$$

and

$$I_2 = \frac{2^{3/4} c}{c + 1^{1/2}} \, \Pi \left[ 1; \arcsin\left( \frac{\delta'}{\delta' + \sqrt{2}\eta^2 c} \right)^{1/2}, \frac{c+2}{2(c+1)} \right]$$

$$\approx 2\frac{\delta'^{1/2}}{\eta} + \frac{2^{3/4} c}{(c+1)^{1/2}} \left[ \mathrm{K}\left( \frac{c+2}{2(c+1)} \right) - \frac{2(c+1)}{c} \mathrm{E}\left( \frac{c+2}{2(c+1)} \right) \right], \tag{3.34}$$

where

$$\Pi(n; \phi, k) \equiv \int_0^\phi (1 - n\sin^2\theta)^{-1} (1 - k^2\sin^2\theta)^{-1/2} \, d\theta \tag{3.35}$$

is the incomplete elliptic integral of the third kind and $\mathrm{K}(k) \equiv \int_0^{\pi/2} (1 - k^2\sin^2\phi)^{-1/2} d\phi$ and $\mathrm{E}(k) \equiv \int_0^{\pi/2} (1 - k^2\sin^2\phi)^{1/2} d\phi$ are the complete elliptic integrals of the first and second kinds, respectively (see §17.2 and §17.3 of Abramowitz & Stegun, 1964, for example). Adding these expressions, the leading order terms in $\delta'$ cancel giving $L$ to leading order in $\eta$ as

$$L = 2\sqrt{2} \arctan\left( \frac{\sqrt{7}}{3} \right) + \eta \frac{2^{3/4} c}{(c+1)^{1/2}} \left[ \mathrm{K}\left( \frac{c+2}{2(c+1)} \right) - \frac{2(c+1)}{c} \mathrm{E}\left( \frac{c+2}{2(c+1)} \right) \right] + \mathcal{O}(\eta^2). \tag{3.36}$$

The coefficient of $\eta$ in (3.36) has a maximum for fixed $\eta$ at $c = c^*$, where $c^*$ satisfies

$$\mathrm{K}\left(\frac{c^* + 2}{2c^* + 2}\right) = 2\mathrm{E}\left(\frac{c^* + 2}{2c^* + 2}\right).$$ (3.37)

Solving this equation numerically, we find that $c^* \approx 0.5332$, and so obtain the asymptotic expression

$$L_{\max} = 2\sqrt{2}\arctan\left(\tfrac{\sqrt{7}}{3}\right) - 3.1525\left(\mathcal{D} - \sqrt{2}\right)^{1/2} + \mathcal{O}\left(\mathcal{D} - \sqrt{2}\right),$$ (3.38)

which compares very favourably with the numerically computed values of $L_{\max}$ presented in figure 3.8b.

For the limiting case $\mathcal{D} = \sqrt{2}$, the above analysis breaks down because then $\eta = 0$ and we lose the freedom to vary $H_0$. However, by letting $\epsilon = c\eta^2$ (so that $H_0 = \epsilon - \sqrt{2}$) we may write $c\eta = c^{1/2}\epsilon^{1/2}$. Taking the limit $\eta \to 0$ of (3.36) with $\epsilon \ll 1$ fixed (i.e. $c \to \infty$) we find

$$L(\epsilon) = 2\sqrt{2}\arctan\left(\tfrac{\sqrt{7}}{3}\right) + \epsilon^{1/2}2^{3/4}\left[\mathrm{K}(\tfrac{1}{2}) - 2\mathrm{E}(\tfrac{1}{2})\right] + \mathcal{O}(\epsilon).$$ (3.39)

This has a maximum value of $2\sqrt{2}\arctan(\sqrt{7}/3)$ at $\epsilon = 0$, which is the same value as that found from (3.38) in the limit $\mathcal{D} \searrow \sqrt{2}$. It is also reassuring to note that, as $\mathcal{D} \nearrow \sqrt{2}$ with $\epsilon$ fixed, the expression in (3.30) also gives $L \approx 2\sqrt{2}\arctan(\sqrt{7}/3)$.

For completeness, we consider finally the limit $\mathcal{D} \gg 1$, although this limit is unlikely to be experimentally attainable. To leading order in $\mathcal{D}^{-1}$, the integral for $L(H_0, \mathcal{D})$ is given by

$$L(H_0, \mathcal{D}) \approx \mathcal{D}^{-1}\int_{1-H_0^2/2}^{1}\frac{u}{(u^2 - (1 - H_0^2/2)^2)^{1/2}}\,\mathrm{d}u = \mathcal{D}^{-1}H_0(1 - H_0^2/4)^{1/2}.$$ (3.40)

This has a maximum value of $\mathcal{D}^{-1}$ at $H_0 = -\sqrt{2}$ so that in the limit $\mathcal{D} \gg 1$, $L_{\max} \approx \mathcal{D}^{-1}$. This is precisely as we should expect physically, because large density objects can only float when the contribution of surface tension dominates that of the buoyancy due to excluded volume. In particular, the maximum vertical force from surface tension (which is 2 in non-dimensional terms) must balance the weight of the raft (which is $2L\mathcal{D}$). This asymptotic result compares favourably with the the numerical results presented in figure 3.8a.

### 3.4.5 Comparison with experiment

A direct comparison between the theoretical results outlined so far and experimental results is difficult because we have modelled the raft as a perfectly flexible continuum body

*(a)*

*(b)*
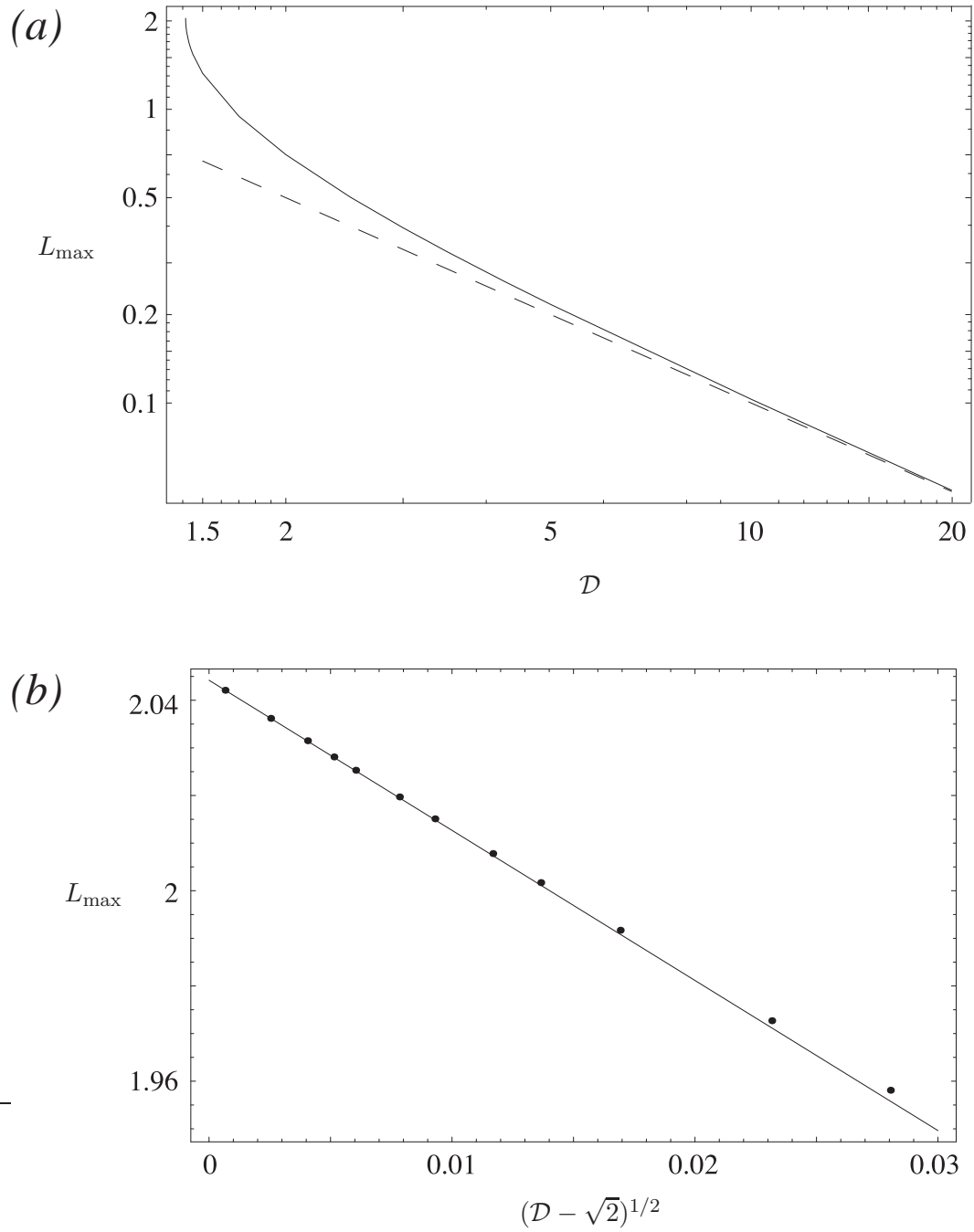
**Figure 3.8:** *(a) Numerical results from the calculation of $L_{\max}$ as a function of the density ratio $\mathcal{D} \geq \sqrt{2}$ (solid line), together with the large $\mathcal{D}$ asymptotic result $L_{\max} \approx 1/\mathcal{D}$ (dashed line). (b) Rescaled graph comparing the numerically computed values (points) of $L_{\max}$ with the asymptotic expansion (3.38) (solid line).*
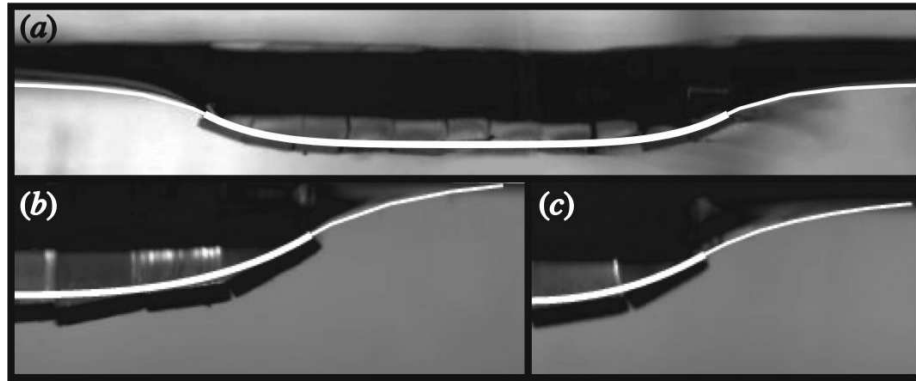
**Figure 3.9:** *Comparison between experimental realization of a two-dimensional raft (viewed through the side of a transparent tank) and the theoretically predicted shape (superimposed white line). The rafts float at an air–water interface and have various values of $\mathcal{D}$ and $L$: (a) a complete raft with $\mathcal{D} = 1.02$, $L = 4.03$ (b) one half of a raft with $\mathcal{D} = 1.27$, $L = 2.57$ and (c) one half of a raft with $\mathcal{D} = 1.27$, $L = 1.47$. The typical width of each individual strip is 2 mm. The black region apparently above the raft is in fact a reflection of the black base of the confining tank from the meniscus at the edge of the tank.*

of infinite extent along its axis of symmetry. Despite these limitations, the theoretical raft shapes calculated via this model are in good agreement with simple experiments in which I laid thin strips of stainless steel shim side-by-side at an air–water interface, as shown in figure 3.9. This agreement is good even when the raft consists of only a small number of strips and we might not expect the continuum approximation to be valid.

Although this agreement is encouraging, our main interest lies more in whether there is a maximum length for such a raft to remain afloat, as predicted by the model. Practical considerations make it difficult to produce strips of stainless-steel shim narrower than about 2 mm in the workshop, so the comparisons we are able to draw between our model and experiments can only be semi-quantitative. In spite of these limitations, we find that for stainless steel strips of length 69 mm and thickness 0.5 mm the maximum raft semi-length is $4 - 6$ mm for an aqueous solution of 25% methanol (so that $1.645 \geq \mathcal{D} \geq 1.580$) and $6 - 8$ mm for 15% methanol (so that $1.494 \geq \mathcal{D} \geq 1.424$). These results are certainly consistent with the corresponding theoretical results of 4.6 mm $\leq L_{\max} \leq$ 4.8 mm and 6.5 mm $\leq L_{\max} \leq$ 7.2 mm, respectively. Here the length was increased by floating additional strips near the raft and allowing them to come into contact via the mutually attractive capillary flotation forces until the raft was no longer stable and sank. With $\mathcal{D} = 1.02$ and $\mathcal{D} = 1.27$, we were able to add many strips without any sign of the raft sinking, indicating that this process might be continued indefinitely. The experimental and theoretical results can be summarized on a regime diagram such as that shown in figure 3.10. This shows the regions of $(\mathcal{D}, L)$ space for which sinking and floating occur and shows very good agreement between experiment and theory.
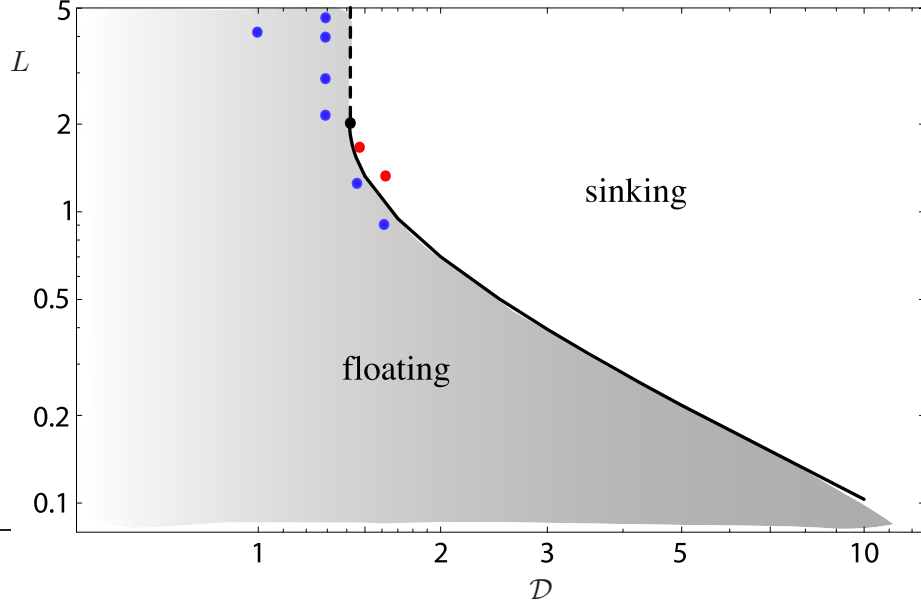
**Figure 3.10:** *Theoretically determined regime diagram showing the regions of $(\mathcal{D}, L)$ space for which floating and sinking are expected to occur. Coloured points represent experiments in which a raft floated (blue) and sank (red).*

## 3.5 Effects of finite bending stiffness

The analysis of the preceding section neglected any resistance to bending that the raft may have. A thin sheet does, however, have a bending stiffness, as do rafts of densely packed particles floating at an interface (Vella *et al.*, 2004*a*). It is natural to ask how the results of the last section carry over to this more general case. In particular, we are interested in determining whether the inclusion of a non-zero bending stiffness alters the conditions for a raft to float in equilibrium.

The variational approach of §3.4.2 may be extended by including a bending energy $\mathcal{B} \int \chi \kappa^2/2 \; \mathrm{d}S$ in the Lagrangian (3.13), where $\mathcal{B}$ is the non-dimensional bending stiffness of the raft and $\kappa = \phi_S = H_{SS} X_S - X_{SS} H_S$ is its curvature. Requiring that the energy be minimized over variations in $H$ and $X$, we find that

$$HX_S + \chi \mathcal{D} - (\lambda H_S)_S + \mathcal{B}\{\chi X_{SS}\phi_S + [\chi X_S \phi_S]_S\}_S = 0, \tag{3.41}$$

$$\left(\tfrac{1}{2}H^2 - 1 + \lambda X_S + \mathcal{B}\{\chi H_{SS}\phi_S + [\chi H_S \phi_S]_S\}\right)_S = 0. \tag{3.42}$$

The variation in $\lambda$ again ensures that the constraint $X_S^2 + H_S^2 = 1$ is satisfied. Eliminating $\lambda$ from these two relations, we find that

$$\lambda_S = \chi \mathcal{D} H_S - 3\mathcal{B}\chi_S \phi_S^2 - \tfrac{5}{2}\mathcal{B}\chi(\phi_S^2)_S, \tag{3.43}$$

so that

$$\lambda = \begin{cases} C_1 + \mathcal{D}H - \frac{5}{2}\mathcal{B}\phi_S^2, & |S| < L \\ C_2, & |S| > L. \end{cases} \tag{3.44}$$

The constant $C_2 = 1$ is determined by the boundary conditions at $S = \infty$. Integrating (3.43) from $S = L - \epsilon$ to $S = L + \epsilon$ and taking the limit $\epsilon \to 0$, we obtain the jump condition

$$[\lambda]_{L_-}^{L_+} = 3\mathcal{B}\phi_S^2(L), \tag{3.45}$$

which gives $C_1 = 1 - \mathcal{D}H_* - \frac{1}{2}\mathcal{B}\phi_S^2(L)$. We may then write

$$\lambda = 1 + \chi\{\mathcal{D}(H - H_*) - \tfrac{1}{2}\mathcal{B}[5\phi_S^2 + \phi_S^2(L)]\}. \tag{3.46}$$

By eliminating $\lambda_S$ from (3.41) and (3.42), we obtain an intrinsic equation for the shape of the raft, which reads

$$\lambda\phi_S + \mathcal{B}(2\phi_S^3 - \phi_{SSS}) = H + \mathcal{D}\cos\phi. \tag{3.47}$$

This is to be solved using the expression for $\lambda$ given in (3.46) with the boundary conditions

$$X(0) = 0, \quad \phi(0) = 0, \quad \phi_{SS}(0) = 0,$$
$$H(L) = H_*, \quad \phi_S(L) = H_*, \quad \phi(L) = -2\arcsin(H_*/2), \tag{3.48}$$

and the geometrical conditions $X_S = \cos\phi$ and $H_S = \sin\phi$.

Our analysis of this system of equations is limited to obtaining its numerical solution for various values of $\mathcal{D}$, $\mathcal{B}$ and $L$. However, this is enough to make some interesting observations about the effect of bending stiffness on the shape of rafts and their ability to float. The system of equations (3.46)–(3.48) were again solved using the MATLAB routine `bvp4c`. The results of these computations were verified by calculation of the quantity

$$Q(\phi) \equiv \tfrac{1}{2}H^2 - 1 + \lambda\cos\phi + \mathcal{B}\left(2\phi_S^2\cos\phi + \phi_{SS}\sin\phi\right), \tag{3.49}$$

which is conserved along the raft and equal to

$$\mathcal{B}\left\{\phi_{SS}(L)\sin\phi(L) - \phi_S^2(L)\cos\phi(L)\right\}.$$

(The conservation of $Q$ follows upon integrating (3.42) once.)

From these numerical solutions we learn two interesting facts about the floating of rafts with non-zero resistance to bending. Firstly, the existence of a non-zero bending stiffness allows dense rafts to remain afloat past the length where a perfectly flexible raft of the
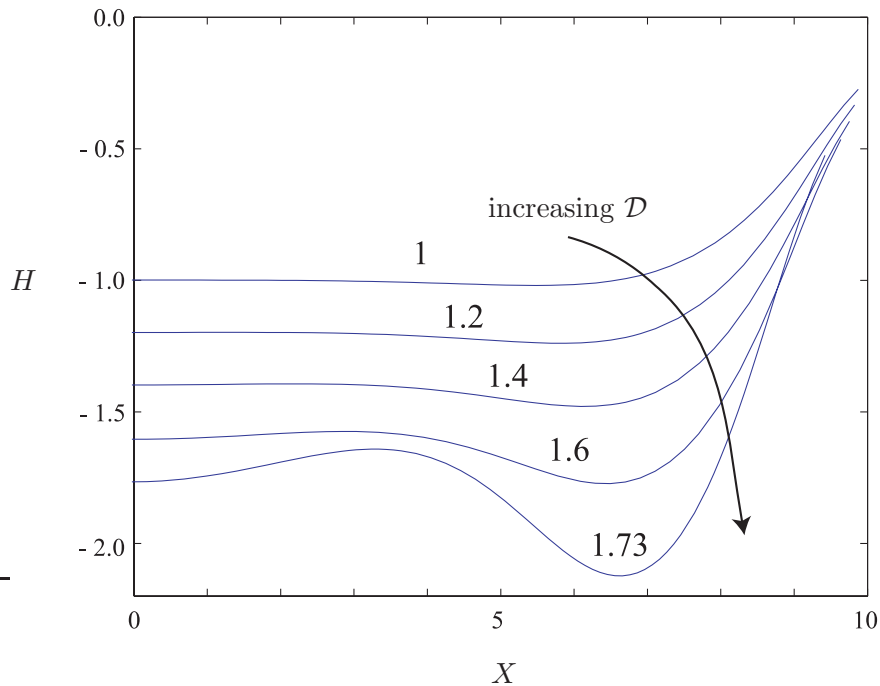
**Figure 3.11:** *The effect of increasing the density on the raft shape. Here $\mathcal{B} = 1$, $L = 10$ and rafts are shown for $\mathcal{D} = 1, 1.2, 1.4, 1.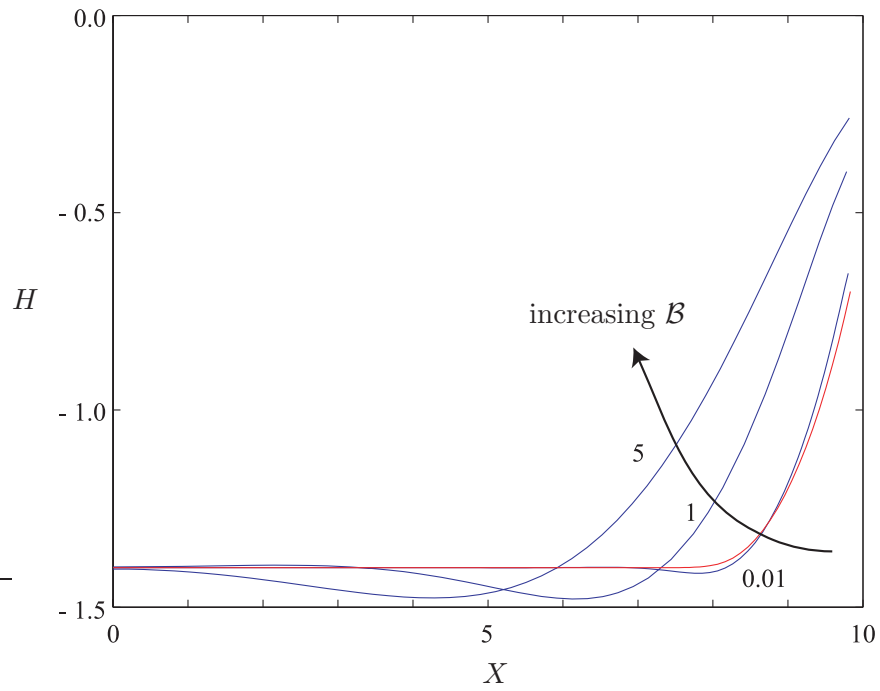6$ and $\mathcal{D} = 1.73$. Only half of the raft is shown, the full raft being obtained by reflection in the $y-$axis. Note that the vertical scale has been enlarged for clarity.*

same density would sink. Two of the rafts shown in figure 3.11 have $\mathcal{D} > \sqrt{2}$ and yet float despite being several times longer than the largest flexible raft, which has $\mathcal{D} = \sqrt{2}$ and $L_{\max} \approx 2$.

Secondly, we notice that wrinkles appear in the raft when it is sufficiently dense or flexible. This is very different from the wrinkling instability observed previously in particle rafts, which is induced by the application of an external compressive force (Vella *et al.*, 2004*a*). Here the wrinkles appear spontaneously, being caused by the tangential component of the raft's weight acting to compress the raft: there is no need for the action of an externally applied force. From figure 3.12 we note that there is a small 'heel' close to the edge of the raft where it must join onto the external meniscus. For $\mathcal{B} \ll 1$ this heel is confined to a small boundary layer near this edge and the remainder of the raft is indistinguishable from the raft shape obtained with $\mathcal{B} = 0$. The horizontal extent of this boundary layer appears to scale with $\mathcal{B}$ (figure 3.12), as we would expect since $\mathcal{B}$ multiplies the highest order derivative in (3.47).

Unfortunately, it seems that it will be very difficult to find a material both soft and dense enough to test these observations experimentally. In terms of dimensional variables,

**Figure 3.12:** *The effect of increasing the bending stiffness on the raft shape. Here $\mathcal{D} = 1.4$, $L = 10$ and rafts are shown for $\mathcal{B} = 0.01, 1$ and $\mathcal{B} = 5$ (solid blue lines). The raft shape in the absence of resistance to bending ($\mathcal{B} = 0$) is also shown for comparison (solid red line). Only half of the raft is shown, the full raft being obtained by reflection in the $y-$axis. Note that the vertical scale has been enlarged for clarity.*

the bending stiffness may be written

$$\mathcal{B} = \frac{E\tau^3}{12(1-\nu^2)(\rho_B - \rho_A)g\ell_c^4},$$  (3.50)

where $E$ is the Young's modulus of the material, $\nu$ is its Poisson ratio and $\tau$ is its thickness. Even for a very soft material such as rubber, $E \sim 10^7$ Pa so that to get $\mathcal{B} = \mathcal{O}(1)$ would require the sheet to be remarkably thin, $\tau/\ell_c \sim 10^{-2}$. Such a thin sheet would in turn have a very small value of $\mathcal{D}$ because $\mathcal{D} \sim \tau/\ell_c$ and so would not produce large enough deformations for wrinkling to be observed.

## 3.6 Discussion

In this chapter, we have quantified the conditions under which multiple objects can remain trapped at a liquid–fluid interface, and shown that when the deformation of the meniscus is suppressed by the presence of other objects, the supporting force that can be generated decreases dramatically. For two small, parallel cylinders or strips, the maximum force that can be supported close to contact is only that provided by the contribution from the exterior meniscus, and so sufficiently dense objects sink upon contact. A two-dimensional raft of touching, floating strips may compensate partially for this loss of meniscus by lowering itself into the fluid. For $\mathcal{D} < \sqrt{2}$, this is sufficient to allow rafts of arbitrary length to remain afloat. For $\mathcal{D} \geq \sqrt{2}$, there is a maximum length (dependent on $\mathcal{D}$) above which equilibrium is not possible.

Although our observation that the elimination of menisci caused by interactions between floating particles can lead to sinking is new, a movie on the website of Daniel Joseph[1] appears to show just this happening in an investigation into the aggregation of two aluminium 'bricks'. Joseph does not, however, dwell on the cause of this and notes it merely as a curiosity.

One intriguing possibility is what role, if any, these effects may have in biological settings. John Bush has pointed out to me that the water-walking bugs *Anurida maritima* often congregate in large groups on the surface of ponds. It is not clear from the available images of these clusters of *Anurida* that the interface is significantly depressed by their presence. However, the ideas presented in this chapter may be relevant to other water-dwelling insects. For example, certain species of mosquito lay their eggs in the form of rafts at the surface of ponds, as shown in figure 3.13. In particular, figure 3.13b shows

---

[1]The movie in question is available for download from:
   `http://www.aem.umn.edu/people/faculty/joseph/particles/floating/`
   (accessed 2nd April, 2007)
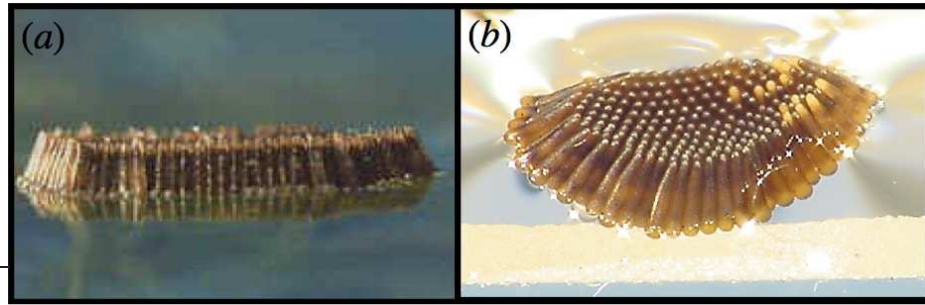
**Figure 3.13:** *Views of mosquito egg rafts floating at an air–water interface. The eggs of (a)* Culex pipiens *and (b)* Coquillettidia xanthogaster. *Typically the rafts are* 6 *mm long and half as wide. Images downloaded from* `http://www.wuvcd.org/mosquito/eggraft.html` *and* `http://www.arbovirus.health.nsw.gov.au`*, respectively.*

very clearly that only the base of the individual eggs are wetted by the liquid. This is because all but the very base of the egg is hydrophobic (Beament & Corbet, 1981) and means that the effective density of the raft is not significantly modified by any excluded volume of liquid. The appropriate density ratio of the egg raft is therefore

$$\mathcal{D} = \frac{\rho_{\text{egg}} h}{\rho \ell_c},$$

where $h$ denotes the height of the individual eggs. Beament & Corbet (1981) found experimentally that $\rho_{\text{egg}} \approx 1.04 \rho$ while Christophers (1945) reports that $h \approx 0.75$ mm. These values give an estimate of $\mathcal{D} \approx 0.3$. Since $\mathcal{D} < \sqrt{2}$, the egg raft should, according our analysis, remain afloat independently of its size. However, it is interesting to note that $\mathcal{D} = \mathcal{O}(1)$; it seems that egg rafts may be 'designed' to allow large eggs whilst not endangering their ability to float.

## Appendix 3.A   Force balance argument

In this appendix, we use a balance of forces argument to derive the governing equations for the shape of a flexible raft of objects. Allowing a tension $T(S)$ to act throughout the raft, the balance of forces tangential to the raft is

$$\frac{\mathrm{d}T}{\mathrm{d}S} = \mathcal{D}\sin\phi = \mathcal{D}\frac{\mathrm{d}H}{\mathrm{d}S}, \tag{3.51}$$

where $\phi(S)$ is the inclination of the raft to the horizontal. Equation (3.51) may be integrated using the boundary condition that $T(L) = 1$ (which arises from the continuity of tension at $S = L$, where the raft meets the free surface), to give $T = 1 + \mathcal{D}\left[H(S) - H_*\right]$, where $H_* = H(L)$. The force balance normal to the raft becomes

$$T\frac{\mathrm{d}\phi}{\mathrm{d}S} + P - \mathcal{D}\cos\phi = 0, \tag{3.52}$$

where $P = -H$ is the hydrostatic pressure in the liquid. Combined with the expression already derived for the tension, (3.52) gives the intrinsic equation for the raft as

$$\frac{\mathrm{d}\phi}{\mathrm{d}S} = \frac{H + \mathcal{D}\cos\phi}{1 + \mathcal{D}(H - H_*)}. \tag{3.53}$$

This is precisely the same form as was derived using a variational approach in §3.4.

# Surface Tension Dominated Impact

### Synopsis

We study the impact of a line mass onto a liquid–gas interface. At early times we find a similarity solution for the interfacial deformation and show how the resulting surface tension force slows the fall of the mass. We compute the motion beyond early times using a boundary integral method, and find conditions on the weight and impact speed of the mass that determine whether it sinks or is trapped by the interface. We find that for given impact speed there is a critical weight above which the mass sinks and investigate the asymptotic behaviour of this critical weight in the limits of small and large impact speeds. Below this critical weight, the mass is trapped by the interface and subsequently floats. We also compare our theoretical results with some simple table-top experiments. Finally, we discuss the implications of our work for the vertical jumps of water-walking arthropods.

## 4.1 Introduction

A carefully placed metal needle will float horizontally on the surface of water. However, if
it is dropped from a height, the needle will break through the surface of the water and sink
into the bulk liquid. Similarly, water-walking arthropods rely on the air–water interface
being strong enough not only to support their weight in equilibrium but also to catch them
when they land after a jump (Bush & Hu, 2006). As we have seen in earlier chapters,
small, dense objects may be able to float at a liquid–gas interface, but they can only do
so if they are placed at the interface sufficiently gently. In this chapter we quantify what
'sufficiently gently' means in this context and study the dynamics of sinking when the
impact is not sufficiently gentle.

The impact of an object onto a liquid surface is an old problem in fluid mechanics and
has been studied extensively (Birkhoff & Zarantonello, 1957; Korobkin & Pukhnachov,
1988). However, previous studies of impact have typically been motivated by large scale
practical (often military) applications such as the tossing of ships by rough seas (Korobkin,
1996), the landing of seaplanes (von Kármán, 1929) and the ricocheting of canon balls
onto enemy ships (Johnson, 1998). In these situations it is primarily the hydrodynamic
pressure impulse that determines the resulting dynamics; the force due to surface tension
may safely be neglected. The relative importance of these inertial hydrodynamic forces to
surface tension is characterized by the Weber number

$$We \equiv \frac{\rho U^2 r_0}{\gamma}, \tag{4.1}$$

in which $U$ is the speed of impact, $r_0$ is the length scale of the object, $\rho$ is the liquid
density, and $\gamma$ is the interfacial tension. Even phenomena at shorter length scales, such
as the running of the basilisk lizard over water (Glasheen & MacMahon, 1996$a$), are
typically classed as 'low speed' (Glasheen & MacMahon, 1996$b$; Gaudet, 1998) despite
having $We \approx 10^3$.

However, for a jumping water strider (Bush & Hu, 2006), as for a falling metal needle,
the inertia of the fluid is less important than its surface tension: $We \lesssim 1$. We shall
examine how surface tension slows a falling object, and begin to understand the dynamic
strength of a liquid–gas interface.

Sufficiently dense objects cannot float at the interface whatever their impact speed.
We shall also study the sinking of such objects. A simple model of sinking from rest
has recently been proposed (Vella *et al.*, 2006$b$) based on the assumption that the shape
of the interface is determined by the quasi-static balance between surface tension and
hydrostatic pressure. The approach adopted here allows us to study the dynamic interfacial

deformation caused by a sinking object and to present a much more complete picture of the sinking process.

The plan of this chapter is as follows. In §4.2 we outline our theoretical formulation of surface tension dominated impact. We then find a similarity solution for the interface shape shortly after impact in §4.3. We use a boundary integral simulation to study the motion at later times, as discussed in §4.4. The remainder of the chapter is then concerned with the conditions under which an object is trapped at the interface or sinks. In §4.5 we determine these conditions theoretically and compare the results with some simple experiments in §4.6. Finally, in §4.7, we consider the implications of our results for water-walking arthropods. Earlier numerical simulations have been aimed at understanding some aspects of their jumps (Li *et al.*, 2005); we focus instead on the impact that occurs when they land. In particular, we show that the jump heights observed in water-walking arthropods are typically close to the theoretically determined maximum possible height for which impact will not cause them to penetrate the surface.

A paper based on the work described in this chapter has been published in *Physics of Fluids* (Vella & Metcalfe, 2007). Paul Metcalfe was involved in discussions about this work and also provided some technical assistance with computations.

## 4.2 Theoretical formulation

We study the impact of a line of mass $m$ per unit length with a liquid of density $\rho$, as shown in figure 4.1. The displacement of the interface at time $t$ after impact is $h(x,t)$. Considering a line mass rather than an object with finite radius simplifies the analysis
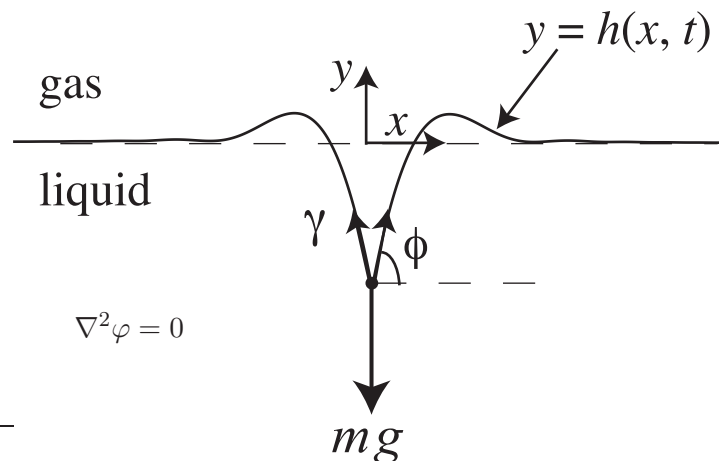


**Figure 4.1:** *Setup for the impact of a line of weight mg per unit length onto a liquid surface.*

in two important respects. Firstly, this situation corresponds to the limit $We = 0$ so that the liquid inertia is entirely neglected: the motion of the mass is controlled by the interfacial tension. Secondly, the contact line is fixed relative to the line mass and we may neglect its motion. For a thin object such as a metal needle, we saw in Chapter 2 that the details of the contact line are unimportant in determining whether the object may float in equilibrium at an interface. It therefore seems reasonable to neglect the contact line in this first study of surface tension dominated impact.

The motion of the line mass is determined by the vertical balance of forces. There are two forces acting on the mass: its weight per unit length, $mg$, and the vertical contribution of the surface tension of the interface, $2\gamma \sin \phi$, where $\phi$ is the angle of inclination of the interface to the horizontal at $x = 0$ (see figure 4.1). The resultant of these two forces gives the vertical acceleration of the mass via Newton's second law

$$m\frac{\mathrm{d}^2 h(0,t)}{\mathrm{d}t^2} = -mg + 2\gamma \sin \phi, \tag{4.2}$$

where $h(0, t)$ denotes the vertical position of the mass at time $t$. Initially, the mass is located at the origin, so that $h(0, 0) = 0$, and has an impact speed $U$, so that

$$\frac{\mathrm{d}h}{\mathrm{d}t}(0,0) = -U. \tag{4.3}$$

The solution of (4.2) and (4.3) is complicated by the dynamic response of the liquid to the motion of the line. This response enters (4.2) via the inclination of the interface to the horizontal, $\phi$. Determining the evolution of $\phi$ requires a model for the fluid motion caused by impact.

Because the line mass does not have its own length scale, the only intrinsic length in the problem is the capillary length $\ell_c \equiv (\gamma/\rho g)^{1/2}$, which is the distance over which equilibrium interfacial deformations decay. Similarly, for initially stationary masses the natural velocity scale is $(\ell_c g)^{1/2}$. Using these two scales, the Reynolds number appropriate for sinking from rest is

$$Re \equiv \frac{\ell_c^{3/2} g^{1/2}}{\nu}, \tag{4.4}$$

where $\nu$ is the kinematic viscosity of the liquid. For an air–water interface, $Re \approx 500$ and so sinking from rest is a high Reynolds number phenomenon. The Reynolds number associated with impact will be at least as large as this. We shall therefore model the fluid as being inviscid and make use of the theory of inviscid flows (Milne-Thomson, 1949; Batchelor, 1967). Since the liquid is initially stationary, the fluid motion induced by the motion of the mass is irrotational and the fluid velocity $\mathbf{u} = \nabla \varphi$ for some velocity potential $\varphi$ (distinct from the interfacial inclination $\phi$). Assuming that the liquid is incompressible,

we therefore have that

$$\nabla^2\varphi = 0 \quad (-\infty < x < \infty, \ -\infty < y \le h(x,t)). \tag{4.5}$$

The geometry is symmetric about $x = 0$, so we consider only $x \ge 0$ henceforth. The velocity potential $\varphi$ is determined by the solution of Laplace's equation (4.5) along with the dynamic and kinematic boundary conditions on the liquid interface $y = h(x,t)$. The dynamic boundary condition may be written

$$\rho\frac{\partial\varphi}{\partial t} + \tfrac{1}{2}\rho|\boldsymbol{\nabla}\varphi|^2 + p + \rho g h = 0, \tag{4.6}$$

where $p = -\gamma h_{xx}(1 + h_x^2)^{-3/2}$ is the pressure jump across the interface due to surface tension. The motion of the line mass causes fluid motion since the fluid at the point $[0, h(0,t)]$ is forced to move with the same velocity as the mass. This is a special instance of the kinematic boundary condition

$$\frac{\mathrm{D}h}{\mathrm{D}t} = \frac{\partial\varphi}{\partial y}, \tag{4.7}$$

which applies along the interface $y = h(x,t)$. Initially, the interface is flat and so $h(x,0) = 0$. Far from the mass, the fluid remains quiescent and so $\varphi(x,y,t) \to 0$ as $x^2 + y^2 \to \infty$. Similarly, $h(x,t) \to 0$ as $x \to \infty$. Finally, symmetry about $x = 0$ requires that $\varphi_x(0,y,t) = 0$.

We introduce non-dimensional variables defined by

$$\begin{aligned}
(\tilde{x}, \tilde{y}, \tilde{h}) &\equiv (x, y, h)/\ell_c, \\
\tilde{t} &\equiv t(g/\ell_c)^{1/2}, \\
\tilde{\varphi} &\equiv \varphi/(\ell_c^{3/2} g^{1/2}),
\end{aligned} \tag{4.8}$$

and shall use these variables (with tildes dropped) henceforth. In non-dimensionalizing the system (4.2)–(4.7) in this manner, two dimensionless parameter groups appear. The first of these is the non-dimensional weight per unit length of the line mass, measured relative to surface tension

$$W \equiv \frac{mg}{\gamma}. \tag{4.9}$$

By setting $h_{tt}(0,t) = 0$ in (4.2) we find that the equilibrium flotation of a line mass is only possible if $W \le 2$. The second dimensionless parameter is the Froude number of impact,

$$F \equiv U/(g\ell_c)^{1/2}, \tag{4.10}$$

which measures the impact speed relative to the typical speed of capillary–gravity waves.

The system of equations (4.2)–(4.7) can only be solved numerically. In §4.3 we discuss a similarity solution of this system, which is valid at early times. At later times it is necessary to solve the full time-dependent problem numerically. A numerical scheme to do this, based on the boundary integral method, is presented in §4.4.

## 4.3 Early time similarity solution

For $t \ll 1$ interfacial deformations are small and the only natural length scale, $\ell_c$, does not enter the problem. We therefore expect that there should be an early time similarity solution. In this section, we study this similarity solution to show how the falling mass deforms the fluid interface and radiates capillary waves at early times. We also determine the leading order slowing of the mass due to surface tension.

At early times, the only force acting on the line mass is its weight — the interface is approximately horizontal and so the vertical force contribution from surface tension may be neglected. The equation of motion (4.2) then simplifies to $h_{tt}(0,t) \approx -1$, and we see that the line mass moves ballistically. To leading order in $t$, we have

$$h(0,t) \sim t^{\alpha}, \tag{4.11}$$

where $\sim$ means 'scales as' and

$$\alpha = \begin{cases} 1, & F \neq 0 \\ 2, & F = 0. \end{cases} \tag{4.12}$$

Although general values of the exponent $\alpha$ are of little interest here, the case $\alpha = 2/3$ has been studied extensively(Keller & Miksis, 1983; Billingham & King, 1995; Sierou & Lister, 2004). For the moment, we retain general values of $\alpha$ in order to facilitate comparison with these studies.

The scaling (4.11) and a consideration of the self-consistent dominant balances for $t \ll 1$ lead us to introduce the scaled variables

$$X \equiv xt^{-2/3}, \quad Y \equiv yt^{-2/3} \tag{4.13}$$

and to look for a similarity solution of the form

$$\Phi(X,Y) \equiv t^{(1-3\alpha)/3}\varphi\big(Xt^{2/3}, Yt^{2/3}, t\big),$$
$$H(X) \equiv t^{-\alpha}h\big(Xt^{2/3}, t\big). \tag{4.14}$$

To leading order in $t$, the system (4.2)–(4.7) becomes the time-independent linear system

$$\nabla^2 \Phi = 0,$$
$$\Phi_Y(X,0) = \alpha H - \tfrac{2}{3} X H_X,$$
$$H_{XX} = \left(\alpha - \tfrac{1}{3}\right)\Phi(X,0) - \tfrac{2}{3}X\Phi_X(X,0),$$
$$\Phi_X(0,Y) = 0,$$

(4.15)

with zero boundary conditions at infinity. We note that upon setting $\alpha = 2/3$, (4.15) reduces to the linearized equations derived first by Keller & Miksis (1983) to describe the recoil of a wedge of inviscid fluid. These equations are ubiquitous in surface tension driven flows, and describe the self-similar evolution of many other systems such as the interaction of a vertical plate with a moving fluid interface (Billingham & King, 1995).

Finally, the approximate equation of motion $h_{tt}(0,t) \approx -1$ determines the prefactor in the scaling (4.11) and requires

$$H(0) = \begin{cases} -F, & F \neq 0 \\ -\tfrac{1}{2}, & F = 0. \end{cases} \tag{4.16}$$

The system of equations (4.15) and (4.16) was solved numerically using a second-order finite difference scheme based on a uniform spatial grid. Note that the solution for any $F \neq 0$ may be obtained by rescaling the solution with $F = 1$ ((4.15) is a linear system and
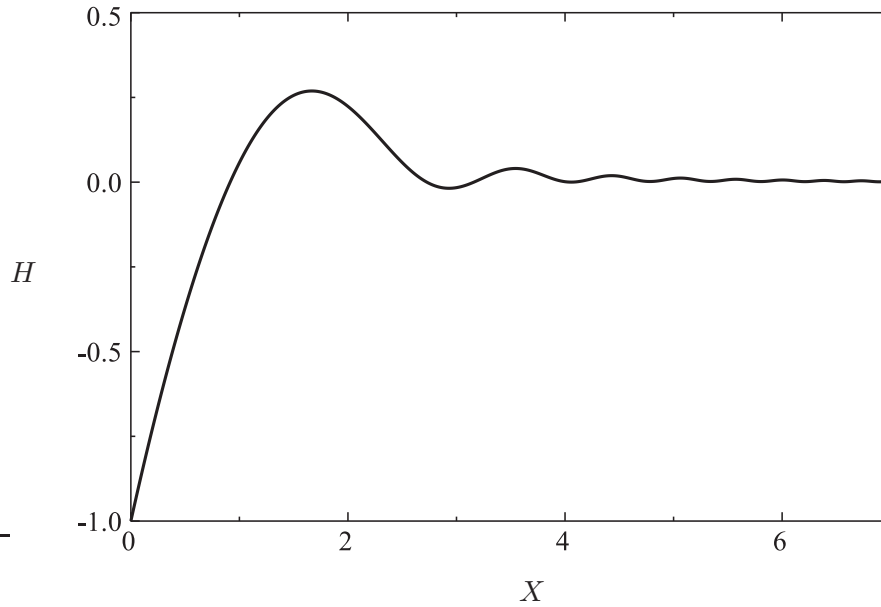


***Figure 4.2:*** *The short time similarity solution for the interfacial profile $H(X)$. Here, $F = 1$ so that the resulting profile can be rescaled to give that for any $F \neq 0$.*

$F$ enters only via the boundary condition (4.16)). Figure 4.2 shows the interfacial profile plotted in similarity variables for the case $F = 1$. (The interfacial profile for the case $F = 0$ is compared to the numerical solution of the time dependent problem in figure 4.5, §4.4.)

### 4.3.1 Far-field behaviour

Figure 4.2 shows that impact generates capillary waves, which decay in amplitude away from $X = 0$. The properties of these waves in the far field can be understood using the WKB approximation, generalizing the analysis of Keller & Miksis (1983) for the case $\alpha = 2/3$. The WKB approximation rests on the assumption that the functions $\Phi$ and $H$ oscillate very rapidly compared to the large scale, $L$, over which they decay. We thus introduce rescaled co-ordinates

$$\xi \equiv \frac{X}{L}, \quad \eta \equiv \frac{Y}{L}, \tag{4.17}$$

and pose series for $\Phi$ and $H$ of the form

$$\Phi = L\big[A^{(0)}(\xi,\eta) + L^{-3}A^{(1)}(\xi,\eta) + \dots\big]\exp\big[iL^3 s(\xi,\eta)\big],$$
$$H = \big[B^{(0)}(\xi) + L^{-3}B^{(1)}(\xi) + \dots\big]\exp\big[iL^3 s(\xi,0)\big]. \tag{4.18}$$

The appearance of $L^3$ terms may be surprising, but is a natural consequence of the dispersion relation for capillary waves, which leads to oscillations with wavenumber $k \sim X^2$ (Sierou & Lister, 2004). We therefore expect the phase of these oscillations to vary as $X^3$ and so, since the length $L$ is arbitrary, an $L^3$ term must appear in the exponential.

Returning to the problem at hand, we substitute the ansatz (4.18) into (4.15) to obtain, at leading order in $L$

$$s_\xi^2 + s_\eta^2 = 0,$$
$$-iA^{(0)}s_\eta - \tfrac{2}{3}i\xi B^{(0)}s_\xi = 0, \tag{4.19}$$
$$-\tfrac{2}{3}i\xi A^{(0)}s_\xi + B^{(0)}s_\xi^2 = 0.$$

The equations in (4.19) give

$$s_\xi = is_\eta, \quad A^{(0)} = -\tfrac{2}{3}i\xi B^{(0)}, \quad s(\xi,0) = \tfrac{4}{27}\xi^3. \tag{4.20}$$

At the next order in $L$, we find that

$$A_\eta^{(0)}s_\eta + A_\xi^{(0)}s_\xi = 0,$$
$$\alpha B^{(0)} - \tfrac{2}{3}\xi B_\xi^{(0)} - A_\eta^{(0)} - iA^{(1)}s_\eta - \tfrac{2}{3}i\xi B^{(1)}s_\xi = 0, \tag{4.21}$$
$$\big(\alpha - \tfrac{1}{3}\big)A^{(0)} - \tfrac{2}{3}\xi\big[A_\xi^{(0)} + is_\xi A^{(1)}\big] - 2iB_\xi^{(0)}s_\xi + B^{(1)}s_\xi^2 - iB^{(0)}s_{\xi\xi} = 0.$$
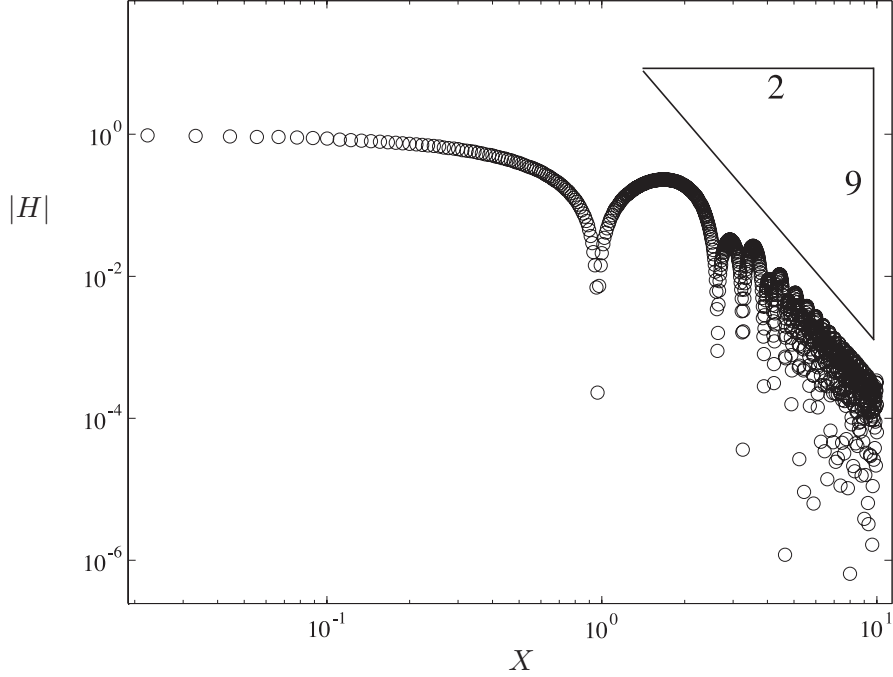
**Figure 4.3:** *The algebraic decay of $H(X)$ observed in numerical solutions of (4.15) and (4.16) is the same as that expected from (4.22). Here $F = 1$ (and so $\alpha = 1$).*

Eliminating $A^{(1)}$ and $B^{(1)}$ from (4.21) and using the results obtained at leading order in (4.20), we find that

$$B^{(0)} \sim \xi^{-\frac{3}{2}(2\alpha+1)}, \tag{4.22}$$

which reduces to the $\xi^{-7/2}$ scaling given previously when $\alpha = 2/3$ (Keller & Miksis, 1983).

The result in (4.22) predicts that the interfacial deformation decays algebraically in the far-field like $X^{-9/2}$ for the impact of a line mass and like $X^{-15/2}$ for a line mass sinking from rest. Both of these scalings are observed in numerical solutions of the system (4.15) and (4.16). Figure 4.3 demonstrates this for the former case ($\alpha = 1$).

The result that $s \approx 4\xi^3/27$ shows that the wavelength of oscillations in the far field satisfies

$$\lambda \approx 9\pi/(2X^2), \tag{4.23}$$

which is again observed in our numerical solutions, as shown in figure 4.4.

### 4.3.2 Modification of ballistic motion by surface tension

We now show how the interfacial deformation studied above slows the ballistic motion of our falling mass. For $t \ll 1$, the inclination of the interface to the horizontal, $\phi \ll 1$.
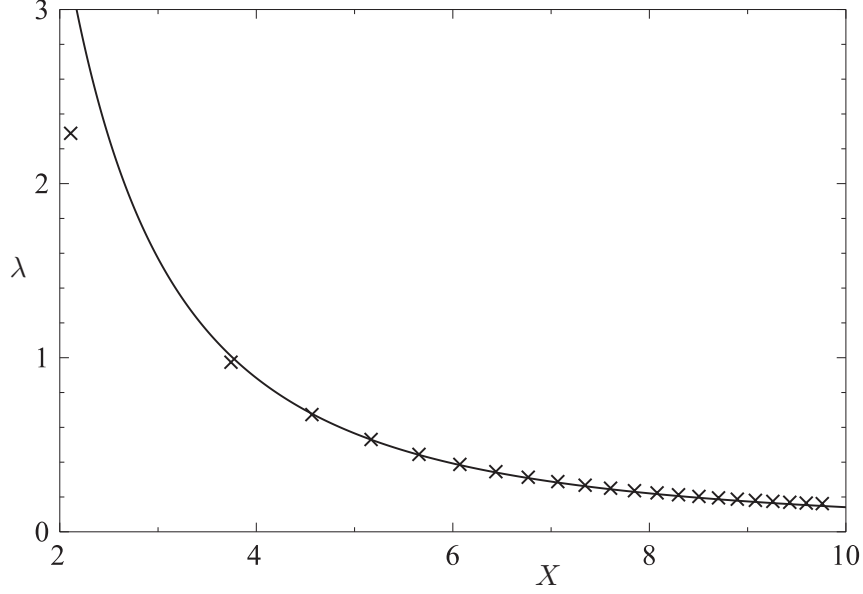
**Figure 4.4:** *The numerically computed wavelength of capillary waves ($\times$) decreases with $X$ in accordance with (4.23) (solid curve). Here $F = 1$.*

Therefore

$$\sin \phi \approx h_x(0, t) \approx t^{\alpha - 2/3} H_X(0).  \tag{4.24}$$

Substituting this expression into the equation of motion (4.2) and posing an expansion for the position of the mass, $h(0, t)$, in powers of $t$, we find that

$$h(0, t) = -Ft - \tfrac{1}{2}t^2 + \frac{18}{W(3\alpha + 1)(3\alpha + 4)} H_X(0) t^{\alpha + 4/3} + \text{ h.o.t.},  \tag{4.25}$$

for $\alpha = 1, 2$. This shows that the leading order correction to the motion of the mass is dependent on the gradient of the interface where it meets the mass, $H_X(0)$, as should be expected.

The value of $H_X(0)$ can be determined from the numerical solution to (4.15) and (4.16) discussed earlier. For the case $F = 0$, we find that $H_X(0) \approx 1.09$ so that

$$h(0, t) \approx -\tfrac{1}{2}t^2 + \frac{0.28}{W} t^{10/3}.  \tag{4.26}$$

Recalling that when $F \neq 0$ the interfacial deformation is proportional to $F$ we find $H_X(0) \approx 1.45F$ so that

$$h(0, t) \approx -Ft - \tfrac{1}{2}t^2 + \frac{0.93F}{W} t^{7/3}.  \tag{4.27}$$

## 4.4 Late times: Boundary integral simulations

In §4.3.2 we showed how interaction with the fluid interface slows the fall of the line mass at early times. However, to determine whether the falling mass is captured by the interface and floats, or breaks through and sinks into the bulk fluid, we must go beyond this early time analysis and compute the trajectory of the mass and the interfacial deformation up to $t = \mathcal{O}(1)$. This requires numerical analysis, and is the subject of this section.

### 4.4.1 The numerical method

Our numerical method is based on a boundary integral method used to study the motion of ships (Greenhow *et al.*, 1982) and other nonlinear free surface flows (see Tsai & Yue, 1996, for a review). Here we give an outline of the numerical method — more details can be found in Appendix 4.A.

We introduce a two-dimensional complex velocity potential

$$\beta(z,t) = \varphi(x,y,t) + \mathrm{i}\psi(x,y,t),\tag{4.28}$$

where $z = x + \mathrm{i}y$ and $\psi$ is the streamfunction of the flow. The velocity $(u, v)$ at any point within the fluid is then given by (Batchelor, 1967)

$$u - \mathrm{i}v = \frac{\mathrm{d}\beta}{\mathrm{d}z}.\tag{4.29}$$

In particular, along the free surface the kinematic boundary condition (4.7) may be written as

$$\frac{\mathrm{D}z}{\mathrm{D}t} = \left(\frac{\mathrm{d}\beta}{\mathrm{d}z}\right)^*,\tag{4.30}$$

where $a^*$ denotes the complex conjugate of $a$. Similarly, the evolution of $\varphi$ at points on the interface is given by the dynamic boundary condition (4.6), which now reads

$$\frac{\mathrm{D}\varphi}{\mathrm{D}t} = \tfrac{1}{2}\left|\frac{\mathrm{d}\beta}{\mathrm{d}z}\right|^2 + \frac{h_{xx}}{(1 + h_x^2)^{3/2}} - h.\tag{4.31}$$

Initially, the interface is flat and the fluid is stationary so that $h(x, 0) = \varphi(x, 0, 0) = 0$. If the complex potential $\beta$ is known at an instant of time, the form of the boundary conditions (4.30) and (4.31) allows us to time-step the value of $\varphi$ at points on the interface and the position of these points. The velocity potential $\varphi(x, h, t)$ is therefore known at any later time, providing that the complex potential, $\beta$, can be determined. We now describe how $\beta$ is calculated.

Since $\varphi$ and $\psi$ are harmonic, $\beta(z)$ is analytic and Cauchy's theorem requires

$$\int_{\mathcal{C}} \frac{\beta(z)}{z - z_k} \, \mathrm{d}z = 0, \tag{4.32}$$

for any point $z_k$ outside a closed contour $\mathcal{C}$. If the real or imaginary parts of $\beta$ are known on enough regions of $\mathcal{C}$, (4.32) may be inverted to give the behaviour of $\beta$ everywhere. Here, $\varphi$ is known all along the interface and $\psi = 0$ along the vertical line $x = 0$ (from symmetry about $x = 0$). The contour $\mathcal{C}$ used here therefore includes the vertical line $x = 0$ and the interface $y = h(x, t)$ and is closed by impermeable boundaries far from the origin, along which $\psi = 0$.

We discretize the contour $\mathcal{C}$ using $N$ points (typically in our simulations $N = 400$). At each of these points, either the value of $\varphi$ is known (if the point is on the free surface) or $\psi = 0$ (if the point is on an impermeable wall). The values of $\psi$ along the surface and of $\varphi$ along the impermeable walls are therefore unknown, giving $N$ unknowns in total. Cubic splines based on arc length are used to interpolate the interface shape and the value of the complex potential $\beta$ between each point.

By taking the $z_k$ in (4.32) to be each of the points on $\mathcal{C}$ in turn, the integral equation (4.32) reduces to a matrix equation for the unknown values of $\varphi$ and $\psi$. This matrix equation may be solved to give the unknown part of $\beta$ at each point on $\mathcal{C}$.

The position of the interfacial points and the value of $\varphi$ at the interfacial points may be evolved by marching (4.30) and (4.31) forward in time using a fourth-order Runge–Kutta scheme. (The spatial derivatives in (4.30) and (4.31) are computed using cubic splines.) This procedure is then iterated.

### 4.4.2  Numerical results

The boundary integral method just discussed tracks the evolution of the interface as well as the motion of the mass. Using this method we are able to follow the motion up to $t = \mathcal{O}(1)$. In particular, for a region of $(F, W)$ parameter space we observe that $\phi = \pi/2$ at some finite time. This corresponds to the interface becoming vertical where it contacts the line mass so that the two menisci joined to the line mass intersect and the mass sinks into the bulk fluid. Alternatively, the velocity of the line mass is observed to change sign so that it begins to rise under the influence of surface tension: the mass has bounced. The conditions under which these two alternatives are realized are discussed in section 4.5. Here, we focus on quantifying some features of the motion up to this point.

At short times, the interface shape is close to that described by the similarity solution discussed in §4.3 (see figure 4.5). Figure 4.6 shows that these capillary waves persist for
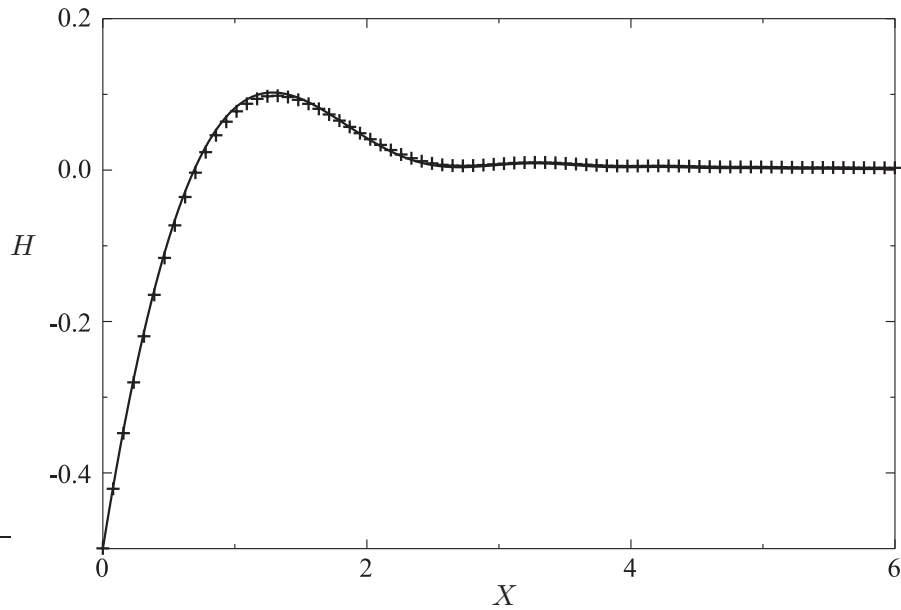
**Figure 4.5:** *Comparison of the interface shape obtained from boundary integral simulations (points) with that predicted by the short time similarity solution discussed in §4.3 (curve). The interface is pictured in similarity co-ordinates $X = x/t^{2/3}$, $H = h/t^2$ at time $t = 0.0253$. Here $W = 5$ and $F = 0$.*

$t = \mathcal{O}(1)$. The results presented in figure 4.6 also demonstrate that the numerical scheme converges as the interfacial grid is refined.

The effect of the interfacial tension on the motion of the line mass is also of interest. The short time similarity solution allowed us to calculate how surface tension slows the motion of the line mass to leading order in time. When $F = 0$, the result in (4.26) predicts that $h(0,t) + t^2/2 \propto t^{10/3}$. Plotting $h(0,t) + t^2/2$ (calculated from the solution to the full time-dependent problem) as a function of $t^{10/3}$ when $F = 0$ shows good agreement with (4.26) for $t \ll 1$ (see figure 4.7). There is a noticeable discrepancy for $t \approx 1$, as is to be expected.
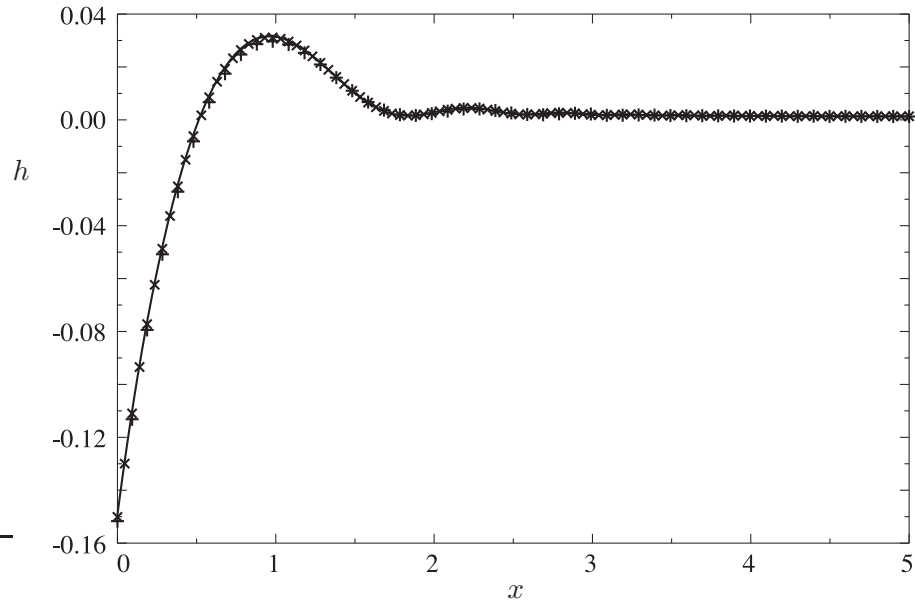
**Figure 4.6:** *Typical interfacial profile obtained from full numerical solutions of the governing equations. The numerical results are presented for various numbers of interfacial grid points $N_f$: $N_f = 50$ (+), $N_f = 100$ (×) and $N_f = 150$ (solid curve). Here $t = 0.5$, $F = 0.1$ and $W = 1.5$.*
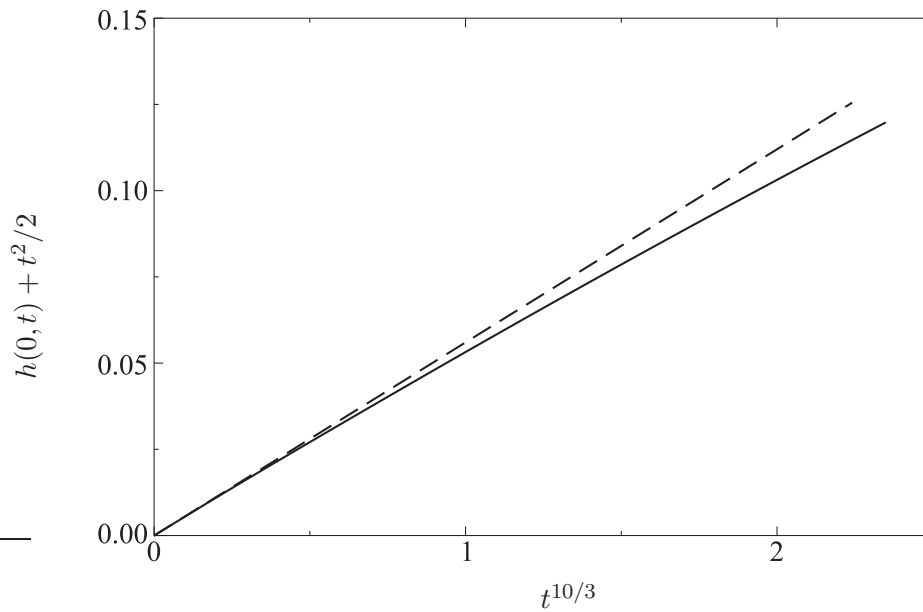


**Figure 4.7:** *The correction to the ballistic motion caused by surface tension for a mass with $W = 5$ and $F = 0$. The results of the boundary integral method (solid curve) agree with the leading order asymptotic prediction (4.26) for $t \ll 1$ (dashed line).*

## 4.5 Impact induces sinking

Common sense suggests that if we wish to float a needle on the surface of water then the needle must be placed on the surface gently. Dropping the needle from a sufficient height onto the liquid's surface will cause it to sink, even if we drop it perfectly horizontally. In this section we quantify this intuitive notion: we determine numerically the values of the parameters $F$ and $W$ for which a line mass will sink or float.

The boundary integral code described earlier was run for a variety of impact speeds, $F$, and line weights, $W$, and whether the mass sank or floated was noted. Before we discuss the results of these simulations, we discuss the criterion for sinking. There are two qualitatively different sinking mechanisms for a cylinder with *finite* radius, depending on the surface properties (in particular, the dynamic contact angle, $\theta_c$) of the cylinder. These mechanisms are illustrated in figure 4.8. When the cylinder surface is hydrophilic $(\theta_c < \pi/2)$ the cylinder sinks when the two contact lines merge at the top of the cylinder. In this case, the interfacial inclination at the contact line $\phi = \theta_c$ at the instant when sinking occurs. When the cylinder is hydrophobic, $\theta_c > \pi/2$, the interface self-intersects before the contact line is able to reach the top of the cylinder, as shown in figure 4.8b. Taking the limit of vanishing cylinder radius with $\theta_c > \pi/2$, we expect that sinking occurs when the interface becomes vertical at the contact line, i.e. $\phi = \pi/2$. Here we shall take this critical interfacial inclination as our criterion for sinking since it applies equally to all dynamic contact angles $\theta_c > \pi/2$.
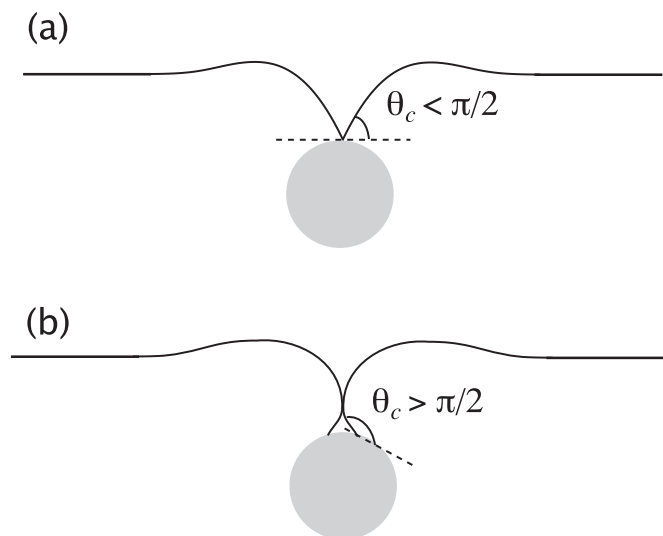


**Figure 4.8:** *The two distinct sinking mechanisms for a cylinder with* finite *radius: (a) for a hydrophilic cylinder surface ($\theta_c < \pi/2$), sinking occurs when the two contact lines meet at the top of the cylinder. (b) For a hydrophobic cylinder surface ($\theta_c > \pi/2$), sinking occurs when the menisci merge above the cylinder.*
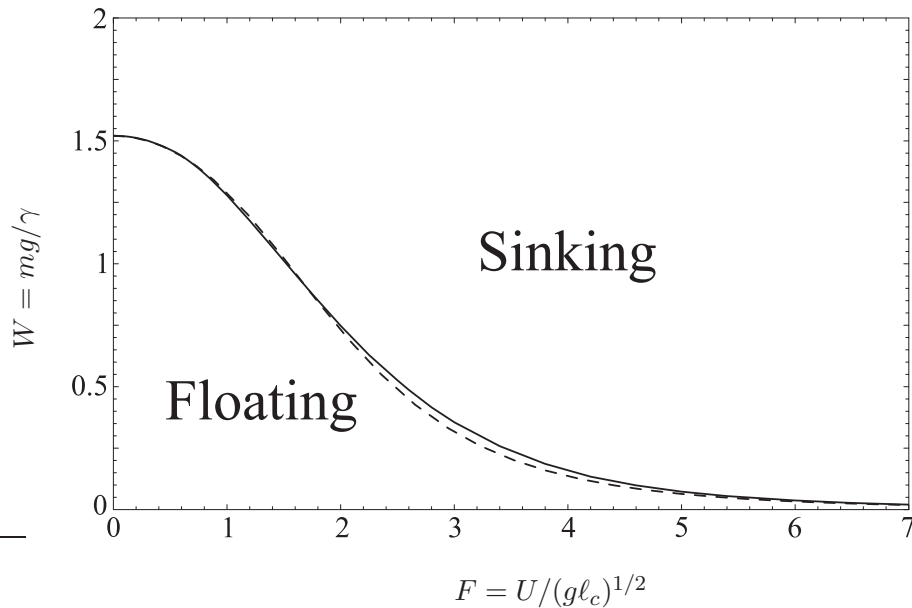
**Figure 4.9:** *Regime diagram showing the regions of $(F, W)$ parameter space for which a line mass is observed to float or sink. The dashed line shows the composite expansion (4.41), which gives $W_c(F)$ to within 15% for intermediate values of $F$.*

Alternatively, the line mass may be trapped by the interface and subsequently float. In our simulations, this occurs when $h_t(0, t)$ becomes positive without $\phi$ having first reached $\pi/2$. This corresponds to a first 'bounce' of the line mass. In reality, dissipation would ensure that a mass that bounces would subsequently float in equilibrium at the interface though our finite computational domain and our neglect of viscosity prevent us from investigating this further.

Figure 4.9 shows the regime diagram that emerges from our computations. We note that for a given impact speed, $F$, there is a critical weight, $W_c(F)$, above which the line mass sinks into the bulk fluid but below which it is trapped at the surface and floats. Equivalently, for a given weight there is a critical impact speed above which sinking will occur, in accordance with intuition. Of particular interest is the function $W_c(F)$. We determined $W_c(F)$ for a range of temporal and spatial resolutions and performed a convergence test on the results to determine the true value of $W_c(F)$ to within 1%. The relative error in $W_c(F)$, $\varepsilon$, decays like $N_f^{-4}$ (where $N_f$ is the number of interfacial points), as shown in figure 4.10. This is consistent with our use of cubic splines.

We now investigate the function $W_c(F)$, the boundary between floating and sinking, by considering the asymptotic limits $F \ll 1$ and $F \gg 1$.
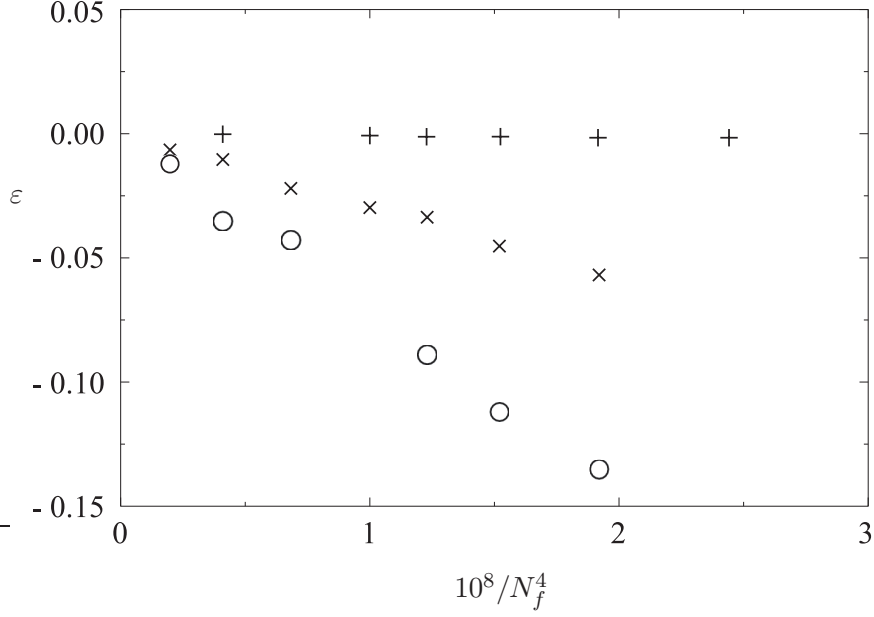
**Figure 4.10:** *Relative error, $\varepsilon$, in the computed value of $W_c(F)$ at different resolutions. The resolution is related to the number of interfacial points used, $N_f = N/4$. Results are shown for $F = 1$ (+), $F = 3.4$ ($\times$) and $F = 14$ ($\bigcirc$).*

### 4.5.1 The limit $F \ll 1$

Using symmetry arguments, we can show that the Taylor series of $W_c(F)$ does not contain a term proportional to $F$. To see this, consider a line mass with $F < 0$ and $|F| \ll 1$, so that the mass initially moves upwards against gravity. Because its initial speed is small, such a mass quickly falls back to its initial height, $y = 0$, under the action of gravity. At this point, its speed is close to its initial speed (viscous dissipation is neglected in our model and little of the kinetic energy of the mass will be radiated as capillary waves in the short time that it takes to fall back to $y = 0$). The mass is then moving downwards and the interfacial disturbance caused by its short upwards motion is small. We therefore expect that the critical weight for sinking, $W_c(F)$, will be approximately $W_c(|F|)$ — the critical weight if the mass had had the same initial speed but directed vertically downwards. The Taylor series of $W_c(F)$ about $F = 0$ cannot, therefore, have a term proportional to $F$.

We can flesh out this argument by estimating the proportion of the particle's initial kinetic energy that is radiated to the surrounding fluid while it is rising against gravity. The time taken for the particle to return to $y = 0$ is $t_* \sim F$. In this time, an area of fluid $t_*^{2/3} \times t_*^{2/3} \sim F^{4/3}$ is accelerated to a speed $F$ removing a kinetic energy $\sim F^{10/3}$ from the particle. The particle therefore returns to the origin with speed $F_*$ where:

$$W(F_*^2 - F^2) \sim F^{10/3}, \tag{4.33}$$
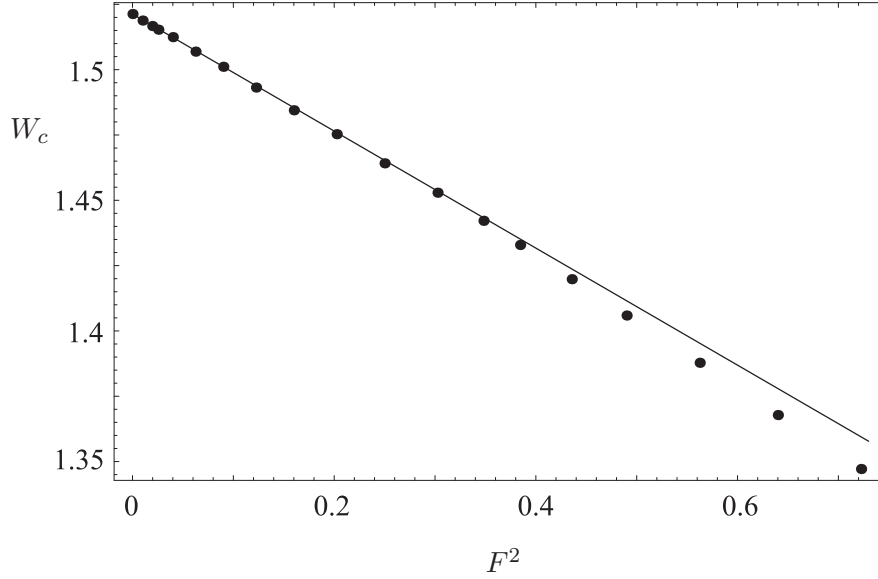
**Figure 4.11:** *Replotting of the boundary between floating and sinking, $W_c(F)$ for $F \ll 1$. The numerically determined values of $W_c$ (points) agree well with the general form suggested in (4.36), which arises from symmetry considerations. The solid line, $W_c = 1.5213 - 0.224F^2$, is plotted as a guide for the eye.*

from which we find

$$F_* - F \sim \frac{1}{W}F^{7/3}. \tag{4.34}$$

Expanding $W_c(F_*)$ about $F$, we may then write

$$
\begin{aligned}
W_c(-F) & \approx W_c(F_*) \approx W_c(F) + W_c'(F)(F_* - F) \\
& \approx W_c(F) + \alpha_0 W_c'(F)F^{7/3},
\end{aligned} \tag{4.35}
$$

for some constant $\alpha_0$. Posing a Taylor series for $W_c(F)$ we find that the term proportional to $F$ must indeed vanish and we may then write

$$W_c(F) \approx W_0 - CF^2, \tag{4.36}$$

for $F \ll 1$. The form of this relationship is observed in the numerically determined values of $W_c(F)$ (see fig. 4.11). Furthermore, the deviation from (4.36) remains very small for $F < 0.6$.

Recall that the maximum weight that can be supported in equilibrium is $W_{\max} = 2$, which arises from setting $h_{tt}(0, t) = 0$ and $\phi = \pi/2$ in (4.2). By comparison, the numerical computations presented here have $W_0 \approx 1.52 < W_{\max}$. This is because a line mass dropped from $y = 0$ has a non-zero velocity when it reaches its equilibrium floating depth. The

mass therefore overshoots its equilibrium floating depth and is more liable to sink.

### 4.5.2 The limit $F \gg 1$

When $F \gg 1$, the line mass has a large impact speed and we expect sinking to occur very quickly, i.e. $t_{\text{sink}} \ll 1$. In this short time, the acceleration due to gravity is negligible and (4.27) may be approximated as

$$h(0,t) + Ft \sim \frac{F}{W}t^{7/3}. \tag{4.37}$$

We also expect that the gradient of the interface at $x = 0$ will be given by the similarity scaling

$$h_x(0,t) \sim \frac{h}{t^{2/3}} \sim Ft^{1/3}. \tag{4.38}$$

We expect sinking to occur when this gradient becomes $\mathcal{O}(1)$, so that $t_{\text{sink}} \sim F^{-3}$. At the critical weight, $W_c(F)$, the mass will be stationary when $t = t_{\text{sink}}$: if it were travelling downwards it would sink, if it were travelling upwards it would already have bounced. Differentiating (4.37) with respect to time and setting $h_t(0, t_{\text{sink}}) = 0$, we find that

$$F \sim \frac{F}{W_c}t_{\text{sink}}^{4/3}, \tag{4.39}$$

which immediately leads to

$$W_c \approx DF^{-4}, \tag{4.40}$$

for some constant $D$. This result compares very well with the numerical results presented in figure 4.12.

Alternatively, the scaling relationship (4.40) may be obtained by considering the conservation of energy. If the line mass is to float, its initial kinetic energy must be successfully converted into surface energy and kinetic energy of the liquid before $t = t_{\text{sink}}$. (A scaling analysis reveals that the surface energy and kinetic energy of the fluid at $t = t_{\text{sink}}$ are of the same order and suggests a form of equipartition.)

### 4.5.3 A composite expansion

The results obtained in the asymptotic limits $F \ll 1$ and $F \gg 1$ can be combined to give an approximate composite expansion that gives an indication of the behaviour of $W_c(F)$ for intermediate values of $F$. The standard additive expansion (Hinch, 1990) does not work because the $F^{-4}$ in (4.40) becomes large for $F \ll 1$ and the $F^2$ in (4.36) dominates
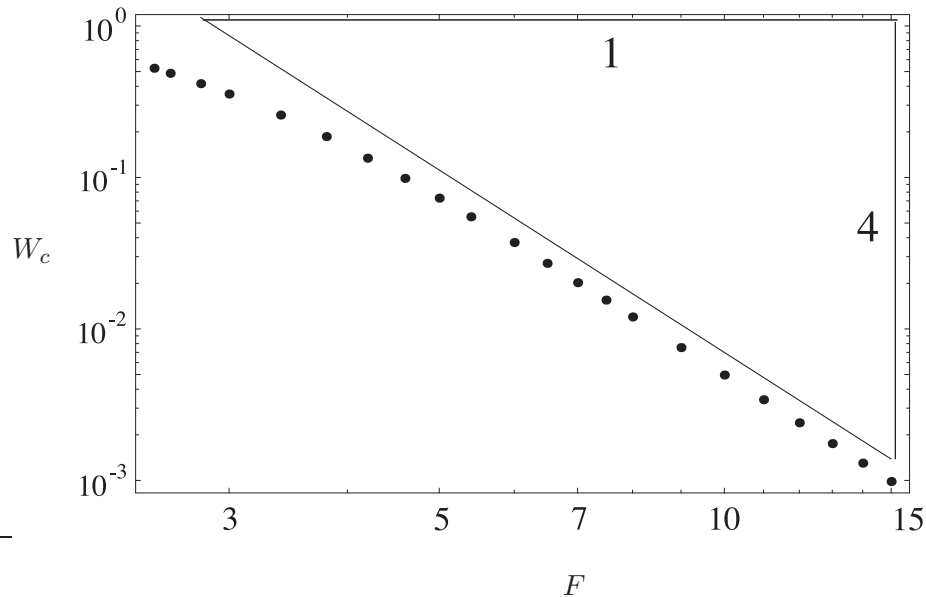
**Figure 4.12:** *Replotting of the boundary between floating and sinking, $W_c(F)$, for $F \gg 1$. The numerically determined values of $W_c$ (points) show the scaling predicted in (4.40).*

for $F \gg 1$. However, we can circumvent this problem by adding the two expressions for $1/W_c(F)$. Inverting the resulting expression gives

$$W_c(F) \approx W_0 \left( 1 + \frac{CF^2}{W_0} + \frac{W_0 F^4}{D} \right)^{-1}. \tag{4.41}$$

From the limits $F \ll 1$ and $F \gg 1$ we estimate that $W_0 \approx 1.52$, $C \approx 0.224$ and $D \approx 49.6$. The resulting composite expansion (4.41) is accurate to within 15% for intermediate $F$ and reproduces the limits $F \ll 1$ and $F \gg 1$ correctly. This result is plotted as the dashed line in figure 4.9.

## 4.6 Experimental results

We performed a series of experiments to test the theoretical picture of a transition between floating and sinking presented in §4.5. Short lengths ($l_s \approx 75$ mm) of steel piano wire were supported horizontally a height $h_{\mathrm{drop}}$ above the interface between air and an isopropanol-water mixture. The wire pieces were then released to determine whether they floated or sank upon impact with the interface. The impact speeds in our experiments were much smaller than the terminal velocity of the wire in air so that air resistance may be neglected.

| Expt. | % isoropanol (vol.) | $r_0$ (mm) | $\rho$ (g cm$^{-3}$) | $\gamma$ (N m$^{-1}$) | $W$ | $R_0$ |
|---|---|---|---|---|---|---|
| 1 | 0 | 0.3 | 0.998 | 0.0728 | 0.30 | 0.11 |
| 2 | 0 | 0.4 | 0.998 | 0.0728 | 0.53 | 0.15 |
| 3 | 10 | 0.3 | 0.977 | 0.0449 | 0.49 | 0.14 |
| 4 | 0 | 0.45 | 0.998 | 0.0728 | 0.67 | 0.17 |
| 5 | 0 | 0.275 | 0.998 | 0.0728 | 0.25 | 0.10 |
| 6 | 0 | 0.35 | 0.998 | 0.0728 | 0.41 | 0.13 |
| 7 | 10 | 0.35 | 0.977 | 0.0449 | 0.66 | 0.16 |
| 8 | 6.25 | 0.275 | 0.985 | 0.0503 | 0.36 | 0.12 |

**Table 4.1:** *Parameter values investigated in the eight sets of experiments presented here. The non-dimensional weight per unit length, $W$, and the dimensionless cylinder radius, $R_0 \equiv r_0/\ell_c$, are dependent on the value of the interfacial tension $\gamma$. The dependence of $\gamma$ on isopropanol concentration is taken from the values given by Vázquez* et al. *(1995).*

The speed of impact is then given by $U = \left(2gh_{\mathrm{drop}}\right)^{1/2}$ and the Froude number is

$$F = \left(\frac{2h_{\mathrm{drop}}}{\ell_c}\right)^{1/2}. \tag{4.42}$$

A cylinder with solid density $\rho_s$ and radius $r_0$ corresponds to a non-dimensional weight per unit length

$$W = \frac{\pi \rho_s r_0^2 g}{\gamma}. \tag{4.43}$$

The steel piano wire used in all our experiments had density $\rho_s = 7850$ kg m$^{-3}$. The weight per unit length of the pieces of wire, $W$, was varied by conducting experiments with six different wire diameters (in the range $0.55 - 0.9$ mm) and by using three isopropanol concentrations $(0, 6.25$ and $10\%$ by volume) to vary $\gamma$. Table 4.1 shows the different combinations of $\gamma$ and $r_0$ used in our experiments and the corresponding values of $W$. The wire diameter was specified by the manufacturer (in terms of wire gauge) and verified using Vernier callipers. The surface tension coefficient $\gamma$ was taken from the literature (Vázquez *et al.*, 1995). The non-dimensional radius, $R_0 \equiv r_0/\ell_c$, is also tabulated to show that in our experiments $R_0 \ll 1$. For each value of $W$, varying the drop height allowed us to vary $F$ and construct an experimental regime diagram for floating and sinking. This regime diagram is shown in figure 4.13 along with the boundary between floating and sinking, $W = W_c(F)$, for a line mass impacting an ideal fluid.

The experimental results plotted in figure 4.13 show that lighter objects can survive impacts at higher speeds. This is in accordance with both the earlier numerical results and intuition. We also note that the boundary between floating and sinking determined for the case of an impacting line mass does not separate the two regions of the experimentally-determined regime diagram particularly well. In particular, we note that the theoretically
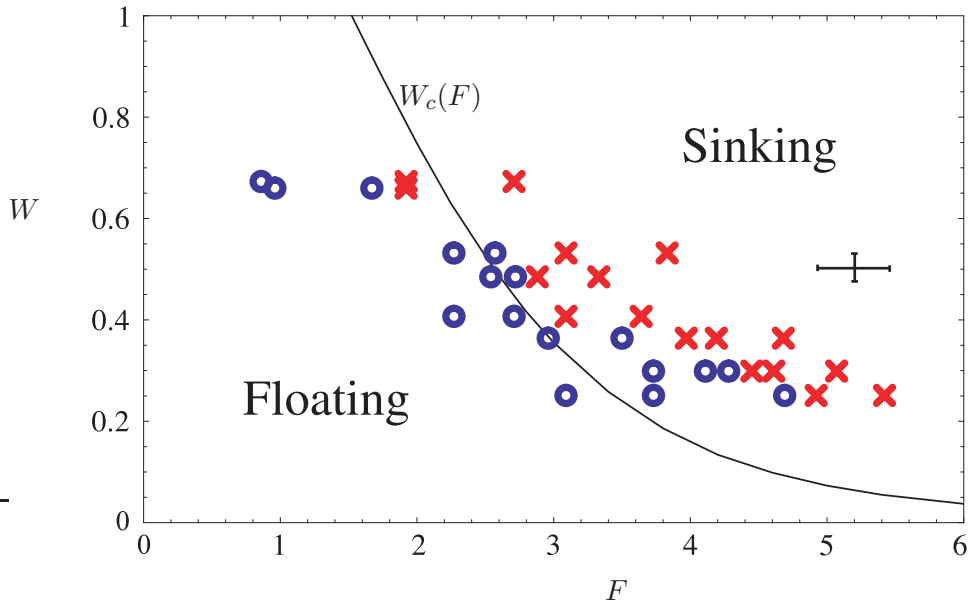
***Figure 4.13:*** *The experimentally determined regime diagram showing values of $W$ and $F$ for which impacting objects were observed to float (blue ◯) or to sink (red ×) upon impact. Here $W = \pi \rho_s R_0^2 / \rho$ and $F = (2h_{\mathrm{drop}}/\ell_c)^{1/2}$. The solid line shows the theoretically computed curve $W = W_c(F)$, which separates floating from sinking for a line mass impacting an ideal liquid. A typical error bar is included for illustration.*

determined value of the critical weight $W_c(F)$ is consistently below that observed experimentally. However, the general trend is qualitatively similar as is the magnitude of the dimensionless parameters at which the transition between sinking and floating occurs.

The observed discrepancy between theory and experiment might reasonably be attributed to the finite radius and length of the wire used in the experiments, both of which were neglected in our theoretical calculations. We now consider the relative importance of these two finite sizes.

The finite length, $l_s$, of the wire means that there is an additional vertical surface tension force arising from the ends, which acts to reduce the effective weight per unit length to some $W'$. The additional surface tension force is at most $\gamma$ times the additional contact line length introduced (Hu *et al.*, 2003), which is $4r_0$. The effective weight per unit length may therefore be estimated as

$$W' \approx \frac{\pi \rho_s r_0^2 g - 4\gamma r_0/l_s}{\gamma} = W - \frac{4r_0}{l_s}. \tag{4.44}$$

In all of our experiments $r_0/l_s < 0.006$ so that $W - W' < 0.024$. This is a small ($< 10\%$) correction for the experimental parameters investigated here and we conclude that it is

most likely our neglect of the finite radius of the wire that dominates the discrepancy between theory and experiment.

There are several physical mechanisms by which the finite radius of a cylinder might cause it to float at higher impact speed than our theory predicts. Here, we limit our discussion to two of these. Firstly, by considering a line mass we have neglected the motion of the contact line, which will sweep around the cylinder during sinking. The dissipation associated with this motion may well be significant and will act as an energy sink slowing the fall of the cylinder. Secondly, our analysis holds only in the limit $We = 0$. In this limit, the force contribution from the dynamic pressure in the liquid is neglected in comparison to the force from surface tension. In our experiments, however,

$$We = F^2 R_0, \tag{4.45}$$

so that for the parameter regime investigated here $0.1 \lesssim We \lesssim 3$. While the Weber number is significantly smaller than in previous impact experiments, the effects of dynamic pressure in the liquid have not been eliminated entirely. This dynamic pressure will supply an additional vertical force that will act to further slow the fall of the cylinder. In particular, we note that as $F$ increases, $We$ increases like $F^2$ so that the effects of the finite cylinder radius are especially pronounced at higher impact speed. This is consistent with the experimental results presented in figure 4.13: for $F \lesssim 3$ theory and experiment are in quantitative agreement (to within the experimental error bars) but for $F \gtrsim 3$ the discrepancy between theory and experiment grows and cannot be explained by experimental errors. A quantitative investigation of these effects is beyond the scope of the present work. However, we note that both contact line motion and the finite Weber number act to slow the impact of the cylinder. They therefore explain, at least partially, the observation that the theory presented here systematically underestimates the experimentally measured value of $W_c(F)$.

## 4.7 Biological discussion

Several species of water-walking arthropod are observed to jump from the water's surface with the objective of avoiding a predator (Suter, 2003; Bush & Hu, 2006) or ascending menisci (Bush & Hu, 2006). Clearly the height of such a jump must be chosen carefully: large jumps may be good for avoiding predators but could potentially cause the arthropod to break through the surface either during the driving strike or upon landing. Here we consider briefly how the jumps of these arthropods fit into the picture we have developed of impact-induced sinking. Where do arthropod jumps lie in the regime diagram presented in figure 4.9?

In nature the fastest impacts occur during the driving stroke that launches an arthropod from the interface (Bush & Hu, 2006). Typically the speed during this stroke is around 1.3 m s$^{-1}$ (Bush & Hu, 2006), which corresponds to a Froude number $F \approx 8$ and Weber number $We \approx 1$ (see table 4.2 for typical values of the leg radius). Based on this Weber number, we expect that the finite leg radius may play an important role in the dynamics of the driving stroke. Li *et al.* (2005) proposed a model for this stroke in which the arthropod is treated as a spring-loaded object at the interface. However, biologically relevant values of the parameters used in this model are not known. These two complications mean that the model of surface tension dominated impact developed in this paper cannot easily be applied to the driving stroke. Instead, we consider landing for which the interface is initially approximately flat and the arthropod's legs are approximately horizontal. Furthermore, the speed of impact is less than the speed during the driving stroke and the corresponding Weber number is less than unity: the arthropod's legs are the analogue of the idealized line masses studied here.

From the arthropod's weight, $mg$, and wetted leg perimeter, $p$, we may calculate an effective value of the dimensionless weight per unit length

$$W = 2\frac{mg}{\gamma p}, \tag{4.46}$$

the factor of 2 coming from the fact that the total leg length is $\approx p/2$. In the biological literature the weight per unit perimeter is often referred to as the *Baudoin number* (Bush & Hu, 2006); in our notation $Ba \approx W/2$. Note that because the legs support the arthropod's body weight, the value of $W$ is substantially larger than the weight of the leg itself.

Two species for which jumping has been documented are the water strider (*Gerridae*) and the fishing spider (*Dolomedes triton*). Typical values for the relevant physical attributes of these arthropods and their jump heights are given in table 4.2 along with the corresponding values of $W$, $F$ and $We$.

We note that both of these arthropods are able to land safely after jumps that are slightly higher than our theory predicts on the basis of their weight. However, the individuals that performed these jumps did not drown. As with the experimental results presented in §4.6, we do not expect the finite length of the arthropod's legs to explain this discrepancy. Instead, we believe that the finite radius of the leg, and hence the finite Weber number, might help arthropods to remain afloat. Note from table 4.2 that the Weber number upon landing is $We \approx 0.45$ for both of the species considered here, suggesting that dynamic pressure forces may indeed be significant.

It also seems possible that the extremely hydrophobic nature of arthropod legs will play an important role. Recent work by Duez *et al.* (2007) on the impact of spheres with

|  | Water Strider (Hu, 2006) | Fishing Spider (Suter & Gruenwald, 2000) |
|---|---|---|
| Leg perimeter (cm) | 2.2 | 16.3 |
| Leg radius ($\mu$m) | 40 | 75 |
| Weight (g) | 0.0045 | 0.233 |
| Jump height (cm) | 4 | $2 - 2.5$ |
| $F$ | 5.4 | $3.8 - 4.2$ |
| $W_c(F)$ | 0.055 | $0.13 - 0.19$ |
| $W$ | 0.06 | 0.19 |
| $We$ | 0.43 | $0.40 - 0.49$ |

**Table 4.2:** *Typical values from the literature for the jumping of two species of water-walking arthropod.*

$We \gg 1$ has shown that the threshold velocity at which an impacting object entrains air decreases substantially as the hydrophobicity of the object increases. The legs of water-walking arthropods are typically covered in a very fine mat of hairs, which render the legs extremely hydrophobic (Bush *et al.*, 2007). If, as seems likely, impacts with $We \ll 1$ are also sensitive to the hydrophobicity of the impacting object, water-walking arthropods may entrain a significant amount of air upon landing. The added buoyancy of any entrained air, as well as the thin air layer trapped by the hairs (Bush *et al.*, 2007), may prevent the legs from piercing the surface after faster impacts than our theory predicts.

Despite the above caveats, it is interesting that both of these species seem to lie so close to the boundary between floating and sinking. This suggests that it may be the threat of sinking during a jump that limits the jump heights of water-walking arthropods. Alternatively, one could argue that the jump height is set by the need to successfully avoid predators. The arthropods therefore seem to have evolved to have the maximum value of $W$ (or minimum leg length, given their weight) for which such jumps are safe.

## 4.8 Conclusions

In this chapter, we have studied the impact of a two-dimensional line mass onto a liquid–gas interface. At early times, we found a similarity solution describing the deformation of the interface caused by impact and studied how the surface tension force arising from this deformation slows the fall of the line mass. Using a boundary integral method, we studied this motion at later times, up to the point at which either the line mass sinks into the bulk liquid or the mass bounces. We have shown that for impact at a given speed, there is a critical weight per unit length above which the line mass will sink; below this weight, the line mass is captured by the interface and floats. We then compared the

results of our numerical calculations with a series of simple experiments and considered how the transition between floating and sinking may limit the height to which water-walking arthropods may safely jump. While the application of our theory to these situations is promising, we believe that better quantitative agreement would be obtained by accounting for the finite radius of the impactor.

## Appendix 4.A    Numerical method

This appendix describes the numerical method used to solve the system of equations (4.5)–(4.7) along with (4.2). These equations describe the sinking of a line mass at high Reynolds number. The results discussed in sections 4.4 and 4.5 were obtained using this numerical method.

In the system of equations (4.5)–(4.7), the velocity potential $\varphi(x, y, t)$ and interface shape $h(x, t)$ are coupled. To simplify the solution of this system we de-couple $\varphi$ and $h$ by solving Laplace's equation (4.5) for a given interface shape and then evolving the properties of the interface using the dynamic and kinematic boundary conditions (4.6) and (4.7). This process is illustrated schematically in figure 4.14 and is expanded upon in the following sections.

### 4.A.1    Solving Laplace's equation: The boundary integral method

The solution to Laplace's equation was found using a boundary integral method. This method is based on the observation that since the velocity potential $\varphi$ and stream function $\psi$ satisfy the Cauchy–Riemann equations, the complex potential $\beta = \varphi + i\psi$ must be analytic everywhere. For every point $z_k$ outside a closed contour $\mathcal{C}$, the Cauchy Integral Theorem immediately gives that

$$\int_{\mathcal{C}} \frac{\beta(z)}{z - z_k} \, \mathrm{d}z = 0. \tag{4.47}$$

This result is valid in the limit as the point $z_k$ tends to the contour $\mathcal{C}$ as long as $z_k$ remains *outside* $\mathcal{C}$.
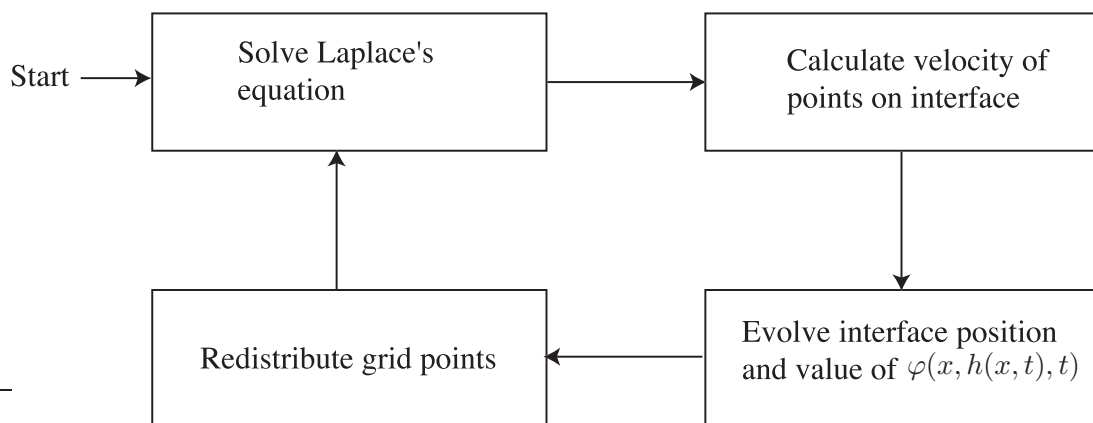


*Figure 4.14:* Schematic diagram showing the main steps in the numerical scheme described in this Appendix.
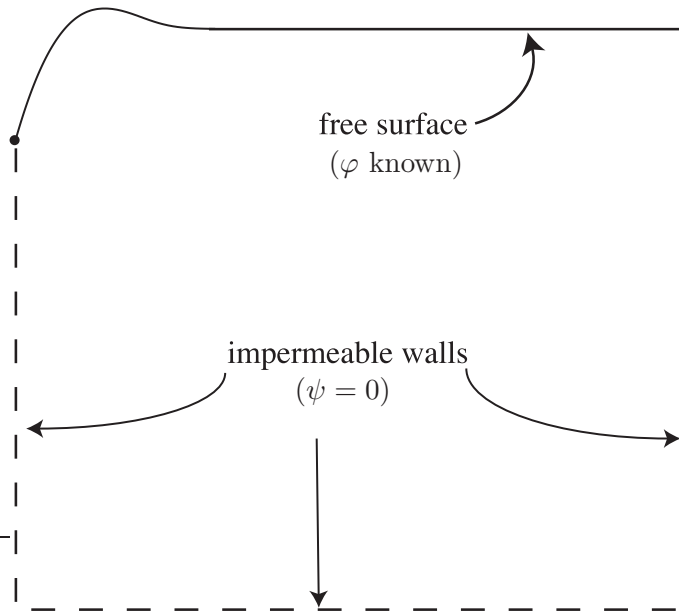
**Figure 4.15:** *Schematic of the contour $\mathcal{C}$ used in the numerical results presented here. $\mathcal{C}$ consists of a free surface (solid line) and impermeable walls (dashed lines).*

For the problem of sinking, we take $\mathcal{C}$ to be the contour consisting of half of the free surface and an impermeable wall beneath the line mass; the latter enforces symmetry about $x = 0$. The contour is closed by impermeable walls, as shown in figure 4.15. Closing $\mathcal{C}$ in this way imposes an artificial reflective symmetry on the system. This is done sufficiently far from the line mass that this artificial boundary condition does not significantly affect the motion. (Recall from the WKB analysis of §4.3.1 that the interfacial deformation decays like $x^{-9/2}$ in the far field for early times.)

To use (4.47) to determine $\beta$ everywhere on the boundary of $\mathcal{C}$, some information about $\varphi$ and $\psi$ along $\mathcal{C}$ is required. In our case, the value of $\varphi$ is known along the interface, having been evolved using the dynamic boundary condition in (4.6). Along the impermeable walls, $\psi = 0$. Finally, the kinematic condition that the velocity of the line mass must match the local fluid velocity requires that

$$\varphi_y(0, h, t) = \frac{\mathrm{d}h(0, t)}{\mathrm{d}t}. \tag{4.48}$$

Solving Laplace's equation therefore reduces to computing the values of $\psi$ on the interface and $\varphi$ along the no-flux boundary by solving (4.47). To do this, we represent the boundary $\mathcal{C}$ by a set of points $\{z_j\}_{j=1}^{N}$ and interpolate between the points with cubic splines. For simplicity, we map the interval $[z_j, z_{j+1}]$ onto $[0, 1]$ so that the integral

equation (4.47) may be written

$$\sum_{j=1}^{N} \int_{0}^{1} \frac{\beta_j(t)}{z_j(t) - z_k} z_j'(t) \, \mathrm{d}t = 0. \tag{4.49}$$

Here, $f_j(t)$ on $[0,1]$ interpolates the function $f(z)$ on the interval $[z_j, z_{j+1}]$ based on its values and the values of its derivatives at the end points $z_j$ and $z_{j+1}$. In particular, for interpolation via a cubic spline, we have

$$f_j(t) = f(z_j)(1 - 3t^2 + 2t^3) + f(z_{j+1})t^2(3 - 2t) + \left[\frac{\mathrm{d}f}{\mathrm{d}t}\right]_{z_j} t(1-t)^2 + \left[\frac{\mathrm{d}f}{\mathrm{d}t}\right]_{z_{j+1}} t^2(t-1). \tag{4.50}$$

This representation of the interface shape and the unknown function $\beta(z)$ allows the integrals in (4.49) to be performed numerically in terms of the (unknown) values of $\beta$ and $\beta' \equiv \mathrm{d}\beta/\mathrm{d}t$ at the points along $\mathcal{C}$. In particular, (4.49) can be written in matrix form as

$$\boldsymbol{F}_1 \cdot \boldsymbol{\beta} + \boldsymbol{F}_2 \cdot \boldsymbol{\beta}' = \boldsymbol{0}, \tag{4.51}$$

where the matrices $\boldsymbol{F}_1$ and $\boldsymbol{F}_2$ are dense since the integral around the contour $\mathcal{C}$ incorporates global information. Here, the vectors $\boldsymbol{\beta}$ and $\boldsymbol{\beta}'$ represent the values of $\beta$ and $\beta'$ at each point on $\mathcal{C}$. The matrices $\boldsymbol{F}_1$ and $\boldsymbol{F}_2$ are calculated using Gaussian quadrature with ten quadrature points in all but two of the intervals: the contribution to the integral that arises from the intervals $[z_{k-1}, z_k]$ and $[z_k, z_{k+1}]$ requires special treatment because of the singularity that occurs at $z = z_k$.

To handle the singularity in the integrand of (4.47) that occurs when $z = z_k$ we write

$$\int_{z_{k-1}}^{z_{k+1}} \frac{\beta}{z - z_k} \, \mathrm{d}z = \int_{z_{k-1}}^{z_{k+1}} \frac{\beta - \beta(z_k)}{z - z_k} \, \mathrm{d}z + \beta(z_k) \int_{z_{k-1}}^{z_{k+1}} \frac{\mathrm{d}z}{z - z_k}. \tag{4.52}$$

The first integral on the right hand side of (4.52) can be computed using Gaussian quadrature since the singularity in the integrand has been 'subtracted out'. The second integral can easily be calculated analytically. However, this introduces a logarithmic term, whose branch must be chosen carefully. The value of the integral in (4.52) must be independent of the path taken from $z_{k-1}$ to $z_{k+1}$ as long as $z_k \notin \mathcal{C}$, as shown in figure 4.16a. To see which branch is appropriate here, we examine the linear function

$$Z(z) \equiv \frac{z - z_k}{z_{k-1} - z_k}. \tag{4.53}$$

The function $Z$ sends the branch point $z_k$ to the origin and $z_{k-1}$ to 1. In this notation, the second integral in (4.52) is just $\log Z(z_{k+1})$, the imaginary part of which is simply the (negative) angle subtended by 1, 0 and $Z(z_{k+1})$. The correct choice of branch is therefore
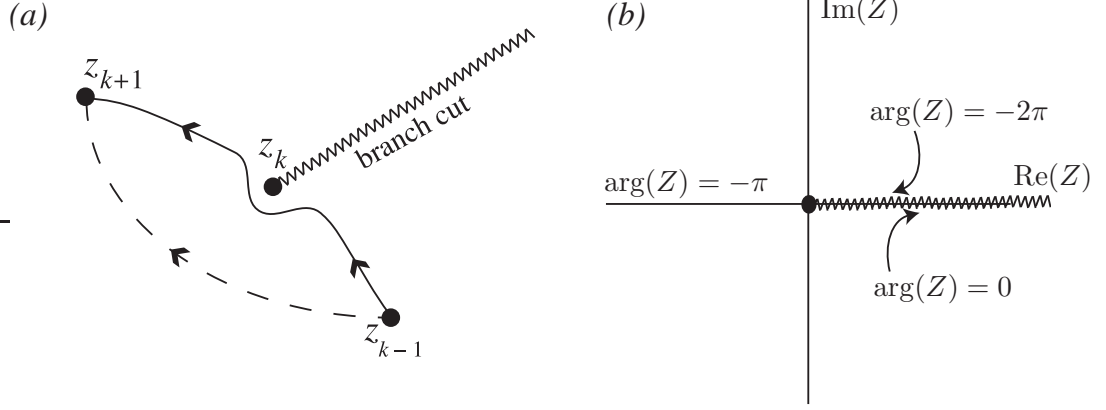
*Figure 4.16:* The branch cut associated with the logarithmic term in (4.52). (a) Since $z_k \notin \mathcal{C}$, the integral from $z_{k-1}$ to $z_{k+1}$ must be the same for the solid and dashed integration paths. This suggests that the correct branch of the logarithm is that illustrated in (b) with the branch cut taken along the positive real axis.

that illustrated in figure 4.16b.

With the matrices $\boldsymbol{F}_1$ and $\boldsymbol{F}_2$ calculated, it only remains to discuss how $\boldsymbol{\beta}$ and $\boldsymbol{\beta'}$ are related. Since derivatives are computed via cubic splines in our approach, $\boldsymbol{\beta'}$ and $\boldsymbol{\beta}$ are in fact related via another matrix equation. It is important that the correct boundary conditions be used for the cubic splines in this method — the order of convergence of the method is reduced if the incorrect boundary conditions are used. Normally, natural boundary conditions (that is $\beta''(z) = 0$ at the end points of the splines) would be used. However, there is no flow through the two corners of the impermeable wall, and so $\beta'(z) = 0$ is the correct boundary condition at these points. Similarly, at the line mass the kinematic boundary condition (4.48) requires that

$$\frac{\mathrm{d}\beta}{\mathrm{d}z} = -\mathrm{i}h_t(0,t). \tag{4.54}$$

Finally the symmetry at the other intersection of the free surface with the impermeable wall gives $\phi_x = 0$ and $\psi_{xx} = 0$ there.

With these boundary conditions correctly implemented we may write

$$\boldsymbol{C} \cdot \boldsymbol{\beta'} = \boldsymbol{D} \cdot \boldsymbol{\beta} + \boldsymbol{C} \cdot \boldsymbol{f}. \tag{4.55}$$

Here the matrices $\boldsymbol{C}$ and $\boldsymbol{D}$ are found by requiring the cubic splines to have continuous first and second derivatives and using the boundary conditions on $\beta'(z)$ at the end points of the splines just discussed. The matrices $\boldsymbol{C}$ and $\boldsymbol{D}$ are sparse since the splines are only 'slightly' nonlocal (Press *et al.*, 1992). The vector $\boldsymbol{f}$ represents a forcing term, which arises from the kinematic condition (4.54) at the line mass. Eliminating $\boldsymbol{\beta'}$ from (4.51)

by using (4.55), we obtain a single matrix equation for $\boldsymbol{\beta}$. The resulting matrix equation (Greenhow *et al.*, 1982) for the unknown parts of $\boldsymbol{\beta}$ may then be solved using MATLAB. In our implementation of this numerical scheme, the matrices were generated in a FOTRAN program but the resulting matrix equation was solved in MATLAB. I wrote these codes but Paul Metcalfe wrote a routine to import the FORTRAN output into MATLAB.

### 4.A.2 Test of numerical solutions to Laplace's equation

The convergence properties of the boundary integral scheme were tested using the simplified problem

$$\nabla^2 \varphi = 0 \quad (0 \leq x \leq 1, -1 \leq y \leq 0), \tag{4.56}$$

with boundary conditions

$$\varphi = \cos(\pi j x) \cosh(\pi j) \quad (y = 0),$$
$$\frac{\partial \varphi}{\partial x} = 0 \quad (x = 0, 1), \tag{4.57}$$
$$\text{and} \quad \frac{\partial \varphi}{\partial y} = 0 \quad (y = -1),$$

for some integer $j$. The system (4.56)-(4.57) has the exact solution

$$\varphi + \mathrm{i}\psi = \cos\big[\pi j(z + \mathrm{i})\big], \tag{4.58}$$
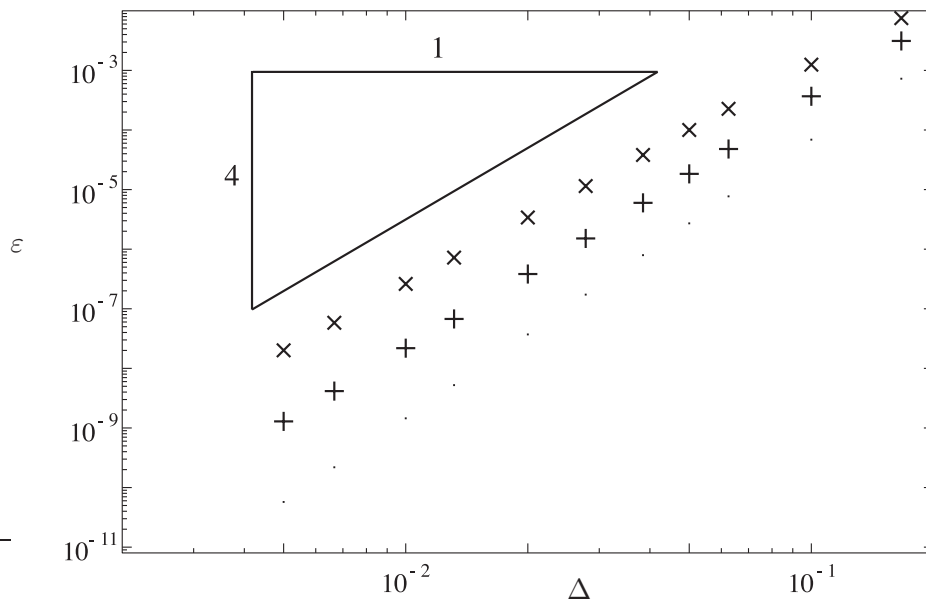


**Figure 4.17:** *Variation of three measures of numerical error, $\varepsilon$, as a function of the grid spacing, $\Delta$, for the case $j = 1$. The maximum error (denoted by $\times$), error at the point $(\frac{1}{2}, 0)$ (denoted by $+$) and the mean error (denoted by $\cdot$).*

which can be used to calculate the error in the numerical scheme for various values of the grid spacing $\Delta$. Typical results are shown in figure 4.17 for the case $j = 1$. These show that the numerical results converge on the analytical solution (4.58) as $\Delta \to 0$ and that this convergence is fourth-order.

### 4.A.3   Time-stepping and regridding

An explicit fourth-order Runge–Kutta method was used to evolve the properties of points on the interface (namely the position of a point and the value of $\varphi$ there). This process is made easier by using the Lagrangian forms of the dynamic and kinematic boundary conditions (4.6) and (4.7). In particular, we have

$$\frac{\mathrm{D}\varphi}{\mathrm{D}t} = \tfrac{1}{2}|\boldsymbol{\nabla}\varphi|^2 - p - h$$
$$\text{and} \quad \frac{\mathrm{D}z}{\mathrm{D}t} = \left(\frac{\mathrm{d}\beta}{\mathrm{d}z}\right)^*,$$
(4.59)

since the components of the velocity $(u, v)$ and $\beta$ are related by

$$u - \mathrm{i}v = \frac{\mathrm{d}\beta}{\mathrm{d}z}.$$
(4.60)

The time-step that can be used in the Runge–Kutta scheme is constrained by the CFL-type condition

$$\Delta t \leq C(\Delta s)^{3/2}$$
(4.61)

where $C$ is a constant and $\Delta s$ denotes the typical spacing in arc length between points (Leppinen & Lister, 2003). Typically, we used $C = 5 \times 10^{-5/2}$ in the simulations reported here.

To avoid the clustering of interfacial grid points, these grid points are regularly redistributed using cubic splines (parametrized by arc length). This ensures that the points remain equi-spaced in arc length. We did not observe the numerical instability that has been reported by others in similar systems (Longuet-Higgins & Cokelet, 1976; Oğuz & Prosperetti, 1990; Gaudet, 1998) and so had no need of the various forms of artificial smoothing that have been suggested previously. In these previous studies the flow was driven by surface tension whereas here it is driven by the motion of the line mass. However, when we used linear interpolation, rather than cubic spline interpolation, we did observe an interfacial instability. It therefore seems that the instability can be suppressed by using a sufficiently high order interpolation scheme.

### 4.A.4  Size of computational domain

When $F \gg 1$, sinking occurs at much earlier times than when $F \ll 1$. Because the disturbance caused by the sinking line mass grows like $t^{2/3}$ independent of $F$, care must be taken to ensure that the interfacial deformation caused by sinking is properly resolved. We therefore need to have a higher spatial resolution available for simulations with $F \gg 1$. It would be impractical to increase the number of grid points used for $F \gg 1$ because the computation is only manageable with $\mathcal{O}(400)$ grid points. Instead, we varied the size of the computational domain, $L_d$.

To determine how $L_d$ should scale with $F$ we consider the scaling arguments given in §4.5. Briefly, we expect sinking to occur in a time $t_{\text{sink}} \sim F^{-3}$. By this time the interface will be disturbed up to a distance $\sim t_{\text{sink}}^{2/3} \sim F^{-2}$ away. To resolve this interfacial disturbance, we therefore choose $L_d \sim F^{-2}$. In particular, the simulations described in §4.5 were carried out with

$$L_d = \min(10, 30F^{-2}). \tag{4.62}$$

These values were found to ensure that the interfacial deformation was resolved but also that the interface shape was not unduly affected by the proximity of the reflecting boundary at $x = L_d$.

# The Waterlogging of Floating Objects

All the water in the world,
However hard it tries,
Can never sink the smallest ship,
Unless it gets inside.

*(Anonymous)*

**Synopsis**

We consider the dynamical processes by which a dense and porous object floating in a body of liquid becomes waterlogged and sinks. We first generalize the classic model of capillary rise in a porous medium to present an analytically tractable model of the process, which is valid for objects that are very shallow compared to their horizontal extent. We also find an analytical expression for the time taken for the object to sink under this approximation. We use a series of boundary integral simulations to show that decreasing the horizontal extent of the object decreases the time taken to sink. We find that the results of these numerical simulations are in good quantitative agreement with a series of laboratory experiments. Finally, we discuss the implications of our work for pumice fragments, which are often found floating in open water after a volcanic eruption, occasionally even supporting human remains.

## 5.1 Introduction

In the discussions of sinking earlier in this thesis, it has been implicitly assumed that the bulk density of an interfacial object remains constant. There are, however, situations where this is not the case. For example, during volcanic eruptions pumice fragments (or clasts) are often ejected and end up in the ocean. Because they are initially dry and have a large void fraction (typically the porosity $\phi = 80\%$) the pumice initially floats. It does not remain dry for long, however, and gradually soaks up water by a combination of capillary action and the hydrostatic pressure in the surrounding water; the mean density of the pumice clast increases until it becomes greater than that of the surrounding water at which point the clast sinks. (In this chapter we shall neglect the vertical force on a floating body from surface tension because the objects of interest are typically much larger than the capillary length, $\ell_c$.)

The sinking process can be extremely drawn out for fragments of pumice, which are often found floating as part of a large 'pumice raft' in oceans many months or even years after a volcanic eruption (Whitham & Sparks, 1986). Figure 5.1 shows pumice rafts formed after a recent volcanic eruption near Tonga. During their time afloat, pumice rafts follow ocean currents, which suggests that tracking their progress might yield information on the speed and direction of these currents (Bryan *et al.*, 2004; Vaughan *et al.*, 2007). The sediments formed once the pumice fragments sink also have interesting features that have been noted by sedimentologists (Manville *et al.*, 1998). In these and other applications, it is important to understand the time taken for the pumice to become sufficiently waterlogged that it sinks. Here we address this question by formulating and solving a fluid mechanical model of the waterlogging process and consider the geophysical implications of our results.



***Figure 5.1:*** *Photographs of pumice rafts resulting from eruptions during September 2006 of a volcano near Home Reef, Tonga. These images were taken off the coast of the Fijian Islands in late September/October 2006 and show the extent of the rafts. Images downloaded from:* `http://www.volcano.si.edu/world/volcano.cfm?vnum=0403-08=&volpage=var`*.*
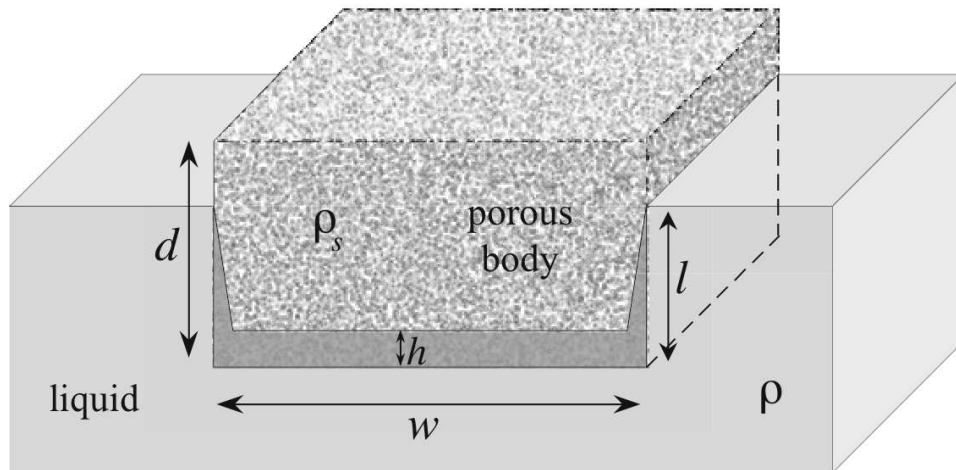
**Figure 5.2:** *Schematic illustration of a porous block floating in a liquid. Due to the combined action of surface tension and hydrostatic pressure, the liquid is imbibed by the porous medium and so the level of the liquid relative to the block, l, rises.*

The plan of this chapter is as follows. We begin in §5.2 by discussing the theoretical formulation in terms of the flow into a floating, porous body. Using a one-dimensional formulation, we are able to derive an analytical expression for the level at which the body floats in the liquid as a function of time. In particular, we obtain an analytical expression for the time taken to sink as a function of the various material properties of the body. §5.3 is concerned with the two-dimensional situation. This cannot be solved analytically and so we introduce a boundary integral formulation of the problem, which we then solve numerically. We discuss the results of these numerical simulations and compare them to a series of laboratory experiments in §5.4. Finally, in §5.5, we discuss some of the implications of our work for the waterlogging of pumice.

A paper based on the work described in this chapter has been published in the *Journal of Fluid Mechanics* (Vella & Huppert, 2007). This work is in collaboration with Herbert Huppert.

## 5.2 Theoretical formulation

Consider a hydrophilic porous body with solid density $\rho_s$ and constant, homogeneous porosity $\phi$. If this is placed in air (of negligible density and viscosity) on the surface of a liquid with density $\rho > \rho_s(1 - \phi)$ then the body will initially float, as shown in figure 5.2. However, the combined actions of the interfacial tension, $\gamma$, and the hydrostatic pressure in the liquid outside the body will force the liquid to impregnate the porous body. If $\rho_s > \rho$

**Figure 5.3:** *Photograph showing the saturation of a pumice fragment with red food dye. At the edge of the wetted portion of the pumice, there is a region of partial saturation, illustrated by the colour variation in this region.*

and the pores are all connected then this process will ultimately cause the object to sink. We are interested in the dynamical processes by which the object becomes waterlogged, and the time at which it will sink.

### 5.2.1 Governing equations

In general, regions of the porous medium may only be partially saturated so that we should compute the evolution of the saturation field (Bear, 1988). In capillary absorption the width of the partially saturated region is typically a constant fraction of the overall depth of the wetted region (Philip, 1969). By observing the capillary absorption of coloured food dye into several pieces of pumice (see figure 5.3), we estimate that this partial saturation region (signified by variations in coloration) is typically $\lesssim 5\%$ of the overall wetted region. Since the region of variable saturation is relatively limited in these rocks, we shall use a sharp interface model in which the free surface separates regions of the object that are fully dry and fully wet. The flow of liquid into the porous body is then Darcy flow (Bear, 1988) in a gravitational field. According to Darcy's law, the liquid velocity within the porous medium, $\boldsymbol{u}$, is linearly related to the pressure gradient by

$$\boldsymbol{u} = \frac{k}{\phi\mu}\left(-\boldsymbol{\nabla}p + \rho\boldsymbol{g}\right), \tag{5.1}$$

where $\mu$ is the dynamic viscosity of the liquid and $k$ is the permeability (assumed uniform) of the porous body. The incompressibility of the liquid requires that $\boldsymbol{\nabla} \cdot \boldsymbol{u} = 0$ so that the pressure in the liquid satisfies

$$\nabla^2 p = 0. \tag{5.2}$$
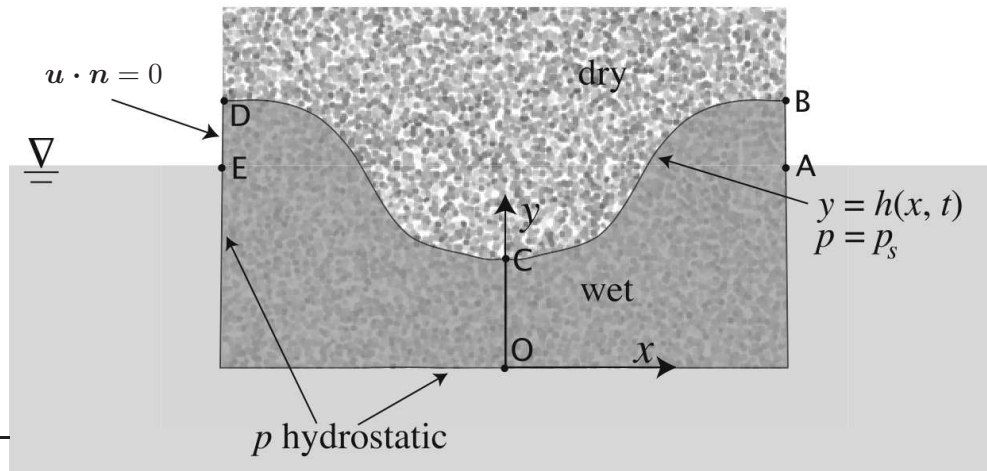
**Figure 5.4:** *Cross–section of the floating body showing the different pressure boundary conditions on the wetted region of the porous body.*

From (5.1) it is clear that the pressure $p$ completely specifies the flow within the porous medium. The problem therefore reduces to solving Laplace's equation (5.2) with suitable boundary conditions. We assume that the pressure distribution in the liquid outside the floating body is purely hydrostatic because sinking typically occurs very slowly. The pressure along the boundary of the body in contact with the exterior liquid (AOE in figure 5.4) is therefore specified by the position of the object in the liquid.

The boundary condition along the air–liquid interface is more complicated. Where the air–liquid interface lies within the porous medium (BCD in figure 5.4), we assume that there is a constant pressure jump across the interface $\Delta p = \gamma \kappa$ where $\kappa$ is the pore-scale curvature. Taking atmospheric pressure as the zero pressure datum, the boundary condition on this interface is therefore $p = p_s$, a constant. Where the air–liquid interface coincides with the edges of the porous medium itself (AB and DE in figure 5.4), the pore-scale meniscus curvature is ill-defined. Here the capillary pressure acts against the hydrostatic head that would tend to drive the fluid to flow out of the block and so we assume that there is no fluid flux through these boundaries, i.e. $\boldsymbol{u} \cdot \boldsymbol{n} = 0$ where $\boldsymbol{n}$ is the normal to the edge of the body. These interfaces are called capillary exposed faces in the literature (Bear, 1988, §7.1.9). The boundary conditions for this problem are summarized in figure 5.4.

The level of the floating body is determined by the assumption that the vertical force balance on the body is satisfied instantaneously. Archimedes' principle applied to the floating body requires that the weight of exterior liquid displaced by the body must be equal to the weight of the body, including the weight of any imbibed liquid. However, it is difficult to express this condition mathematically for general body shapes.

Throughout this chapter, our main focus is on determining the time taken for a given porous body to become waterlogged to the point where it is no longer able to float and therefore sinks. We expect this process to occur on the time scale, $t^*$, over which the liquid flows a distance into the porous medium comparable to its characteristic depth, $d$. From (5.1) the typical fluid speed is $u^* = k\rho g/\phi\mu$ suggesting that we should define

$$t^* \equiv d\phi\mu/(k\rho g). \tag{5.3}$$

We shall use this characteristic time to non-dimensionalize time, $t$, letting $T = t/t^*$. Similarly, we use the characteristic depth $d$ to non-dimensionalize lengths, letting $X = x/d$, $Y = y/d$ and so on. Finally, we introduce a dimensionless pressure $P = p/\rho g d$ (again measured relative to the atmospheric pressure). Letting

$$\Pi \equiv -p_s/\rho g d, \tag{5.4}$$

the constant pressure along the air–liquid interface due to capillarity is $P = -\Pi$ (the minus sign signifying that, for the hydrophilic materials of interest here, capillarity acts to suck liquid into the porous medium). We note that in the experiments presented in §5.4, $\Pi = \mathcal{O}(1)$: the capillary suction pressure and the external hydrostatic pressure are typically of comparable magnitude.

With this formulation of the problem we now turn to a one-dimensional model. This is a modification of the classic analysis of capillary rise in a porous medium given by Washburn (1921). As in Washburn's analysis, we are able to solve the problem analytically in this limit.

### 5.2.2 A one-dimensional model

We begin by considering a one-dimensional model in which liquid can only flow in through the base of the object (the line $Y = 0$ in figure 5.4). This corresponds to the limit in which the object is very shallow in comparison to its horizontal extent. In the one-dimensional case, the air–liquid interface remains planar so that its height above the base is $H(X,T) \equiv H(T)$. Similarly, the pressure within the porous body must only be a function of the height, $Y$, from the base of the body and time $T$. The pressure will also satisfy Laplace's equation (5.2) with boundary conditions $P(0) = L$ and $P(H) = -\Pi$ corresponding to hydrostatic pressure in the exterior liquid at $Y = 0$ and the capillarity induced pressure at the air–liquid interface, respectively. We therefore find

$$\frac{\mathrm{d}P}{\mathrm{d}Y} = -\frac{\Pi + L}{H}. \tag{5.5}$$

Substituting this pressure gradient into Darcy's law (5.1) and equating the liquid velocity to the rate at which the interface moves through the body, we find that

$$\frac{\mathrm{d}H}{\mathrm{d}T} = \frac{\Pi + L}{H} - 1. \tag{5.6}$$

This ordinary differential equation for the motion of the air–liquid interface through the porous medium is dependent on both the height of the interface from the base, $H$, and the submerged depth of the body, $L$. These two quantities are, however, related through the condition of vertical force balance, which here simplifies to

$$L = \phi H + D(1 - \phi), \tag{5.7}$$

in which

$$D \equiv \rho_s/\rho > 1 \tag{5.8}$$

is the density ratio of solid to liquid. Eliminating $L$ from (5.6) using (5.7) and integrating the result subject to $H(0) = 0$, we find that

$$(1 - \phi)T = -H - \Pi_e \log\left(1 - H/\Pi_e\right) \tag{5.9}$$

where

$$\Pi_e \equiv D + \Pi(1 - \phi)^{-1} \tag{5.10}$$

is the effective non-dimensional pressure driving the waterlogging of the body. It is interesting to note that the density of the object enters (5.9) only through the modified driving pressure in (5.10). This is a result of the vertical force balance condition, which requires that the pressure at the base increase linearly with the solid density in order to allow the object to float.

It is not possible to invert (5.9) to give the immersed depth of the object, $H$, in terms of elementary functions of $T$. However, we may write

$$H = \Pi_e \left\{ 1 + W\left[ -\exp\left( -1 - \frac{1 - \phi}{\Pi_e}T \right) \right] \right\}, \tag{5.11}$$

where $W(x)$ is the Lambert W-function, defined as the solution of $x = W(x)\exp[W(x)]$ (see Corless $et\ al.$, 1996, for example). In fact, the form of (5.9) is extremely convenient for determining the time, $T_s$, taken for the body to become waterlogged and sink: sinking occurs when the exterior free surface coincides with the top edge of the body, i.e. when $L = 1$. From (5.7) we therefore have that $H(T_s) = D + (1 - D)/\phi$, which may be substituted

directly into (5.9) to give

$$T_s = \frac{\Pi_e - \Pi - 1}{\phi(1 - \phi)} - \frac{\Pi_e}{1 - \phi}\left(1 + \log\left[\frac{\Pi_e - \Pi - 1}{\Pi_e\phi}\right]\right). \tag{5.12}$$

Here we have used $\Pi$ to simplify the result. For our purposes, it is enough to note that $T_s$ is a monotonically decreasing function of $\Pi$ and therefore that the maximum time, $T_{\max}$, to sink for given values of the density $D$ and porosity $\phi$ is

$$T_{\max} = \frac{D - 1}{\phi(1 - \phi)} - \frac{D}{1 - \phi}\left(1 + \log\left[\frac{D - 1}{D\phi}\right]\right). \tag{5.13}$$

## 5.3 Numerical simulations

In the one-dimensional model presented above, we have assumed that liquid can only flow in through the base of the floating object and flows only vertically. In general, the flow through the sides of the body could also be considerable and will presumably cause the object to reach the sinking density more quickly. We now consider how much of an effect this is.

For simplicity, we consider a two-dimensional body with rectangular cross-section, as shown in figure 5.2. The body has width $w$ and depth $d$ as in figure 5.2. In non-dimensional terms the porous medium occupies the region $|X| \leq \mathcal{A}/2, 0 \leq Y \leq 1$, where $\mathcal{A} \equiv w/d$ is the aspect ratio of the body. The air–liquid interface is given by $Y = H(X, T)$ and moves through the body according to the kinematic boundary condition

$$\frac{\mathrm{D}H}{\mathrm{D}T} = \boldsymbol{U} \cdot \boldsymbol{e}_y|_{Y=H}, \tag{5.14}$$

where $\boldsymbol{e}_y$ is the unit normal in the vertical direction and $\boldsymbol{U}$ is given by the dimensionless version of Darcy's law (5.1). The evolution of the air–liquid interface therefore depends on the pressure in the liquid and thus on the level, $L$, at which the body floats in the liquid. As the liquid infiltrates the floating body, $L$ increases according to the vertical force balance condition, which requires that

$$L = D(1 - \phi) + \frac{\phi}{\mathcal{A}}\int_{-\mathcal{A}/2}^{\mathcal{A}/2} H \, \mathrm{d}X. \tag{5.15}$$

As soon as $L > 1$, the body sinks because it is then more dense than the surrounding liquid. What interests us here is the time taken for the body to reach the critical value $L = 1$.

In this two-dimensional problem, the air–liquid interface does not remain planar and the associated free-boundary problem cannot be solved analytically. The sinking time cannot,

therefore, be determined analytically and we resort to a numerical method to calculate the dynamics of liquid motion in the body and thereby calculate $T_s$. We now discuss this numerical method in more detail.

### 5.3.1 Numerical method

We used a boundary integral method to solve Laplace's equation (5.2) for the pressure $P$ in the porous medium. Our method is based on a boundary integral method used to study two-dimensional potential flow problems (see Tsai & Yue, 1996, for a review of these methods) and is very similar to the method used in Chapter 4. The connection to two-dimensional potential flows arises upon introducing a velocity potential $\Phi \equiv -Y - P$ so that $\boldsymbol{U} = \boldsymbol{\nabla}\Phi$. It is then natural to introduce the corresponding streamfunction $\Psi(X, Y; T)$. Both $\Phi$ and $\Psi$ are harmonic functions and so the complex potential $\beta(Z; T) \equiv \Phi(X, Y; T) + \mathrm{i}\Psi(X, Y; T)$ is analytic within the wetted porous medium (where $Z = X + \mathrm{i}Y$). By Cauchy's theorem, therefore,

$$\int_{\mathcal{C}} \frac{\beta}{Z - Z_k} \, \mathrm{d}Z = 0, \tag{5.16}$$

where $\mathcal{C}$ is the closed contour bounding the wetted porous medium (ABCDEOA in figure 5.4) and $Z_k$ is a point outside the contour $\mathcal{C}$.

At an instant of time, the pressure on most of the air–liquid interface and on the portion of perimeter that is in contact with the exterior fluid is given by the configuration of the body. The velocity potential $\Phi$ is therefore known at these positions on the contour $\mathcal{C}$. On the small portions of the air–liquid interface that coincide with the boundary of the porous body (the capillary exposed faces), $\Phi$ is unknown since the pressure there is unknown. However, because there is no flux through these faces, they are streamlines and we may set $\Psi = 0$ along these portions of $\mathcal{C}$. Therefore either the real or imaginary part of $\beta$ is known for every portion of $\mathcal{C}$. After discretizing the contour $\mathcal{C}$, (5.16) we use linear interpolation (rather than the cubic spline interpolation used in Chapter 4) to calculate the matrix equation corresponding to (5.16). This is a matrix equation for the unknown parts of $\beta$, which may be solved numerically (as discussed by Greenhow $et\ al.$, 1982). The complex potential $\beta$ is therefore known all around $\mathcal{C}$ at a given instant of time.

From complex potential theory, the velocity $(U, V)$ of the fluid within the porous medium satisfies $U - \mathrm{i}V = \mathrm{d}\beta/\mathrm{d}Z$ (Batchelor, 1967). The kinematic boundary condition (5.14) for the motion of points on the air–liquid interface may therefore be written as

$$\frac{\mathrm{D}Z}{\mathrm{D}T} = \left(\frac{\mathrm{d}\beta}{\mathrm{d}Z}\right)^*, \tag{5.17}$$

where * denotes the complex conjugate. The derivative in (5.17) is calculated numerically using a second-order central-difference scheme. The position of points on the air–liquid interface is then stepped forward in time using the fourth-order Runge–Kutta method. The points are regularly redistributed according to the smoothing scheme proposed by Longuet-Higgins & Cokelet (1976) to suppress an unphysical interfacial instability. The new value of $L$, the level at which the body floats in the liquid, is calculated using (5.15). This method is repeated marching forward in time, until $L = 1$ at some time $T = T_s$.

Our simulations typically used 100 interfacial nodes and a simple variable time-step routine. The time-step is chosen to ensure that the fastest moving interfacial point moves less than 1% of the grid spacing in a single step. The convergence of our scheme was tested by varying the number of nodes used and the time step; the results presented here are accurate to $\lesssim 1\%$. We first validated our numerical scheme by comparing the results for capillary rise in a (immobile) porous medium with the analytical result

$$H(T) = \Pi \left\{ 1 + W \left[ -\exp \left( -1 - \frac{T}{\Pi} \right) \right] \right\}, \tag{5.18}$$

which has been given by, among others, Lago & Araujo (2001) using the analysis of Washburn (1921). This comparison is made in figure 5.5 and shows that the agreement is very good. We also compared our results for sinking with the analytical result from our one-dimensional model (5.11) in the limit of shallow floating objects.
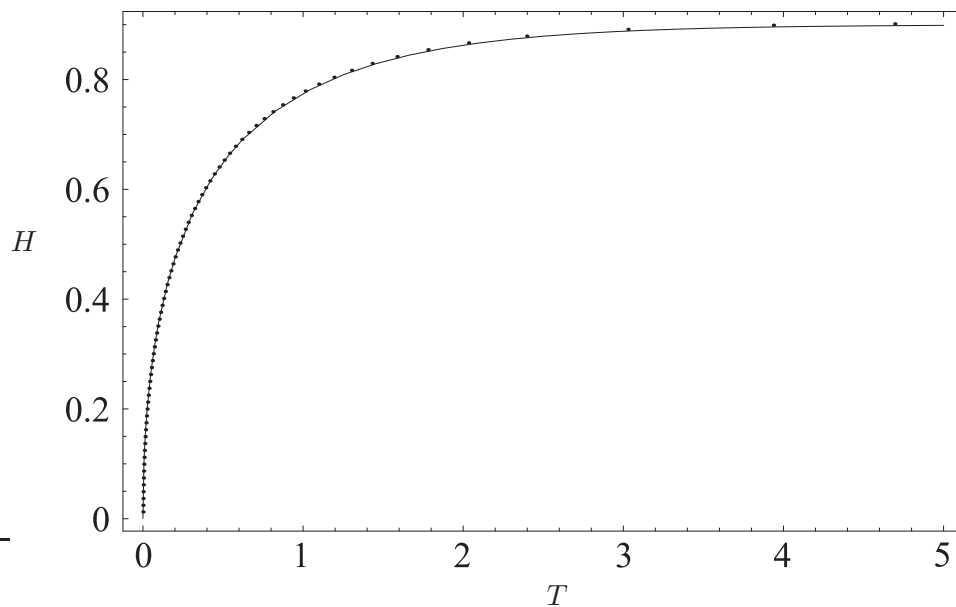


***Figure 5.5:*** *Comparison between simulation results (points) and the analytical result (5.18) (solid curve) for $H(T)$ in capillary driven flow into an immobile porous medium. Here $\Pi = 0.9$ and $\phi = 0.3$.*
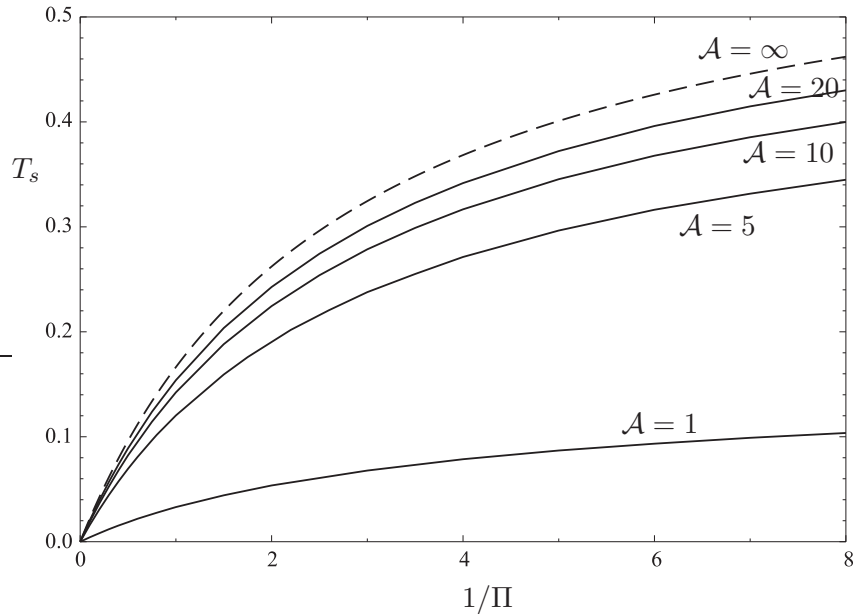
**Figure 5.6:** *Numerical results for the non-dimensional time to sink, $T_s$, as a function of the strength of surface tension, $\Pi$, for various values of the aspect ratio $\mathcal{A}$ of the object. The dashed line shows the analytical prediction of the one-dimensional model, corresponding to the limit $\mathcal{A} = \infty$. Here $D = 2.3$ and $\phi = 0.8$ as is typical of pumice (Whitham & Sparks, 1986).*

### 5.3.2 Results

The non-dimensional time to sink depends on the four non-dimensional parameters already discussed: the density ratio $D$; porosity $\phi$; aspect ratio $\mathcal{A}$; and the strength of surface tension $\Pi$. In the case of pumice clasts the first two of these parameters are reasonably constant with $D \approx 2.3$ and $\phi \approx 0.8$ (Whitham & Sparks, 1986). In the numerical results presented here, therefore, we have held these two parameters constant and varied only the aspect ratio $\mathcal{A}$ and the strength of surface tension $\Pi$.

The time taken to sink, $T_s$, as calculated by our boundary integral simulations is plotted in figure 5.6 as a function of $1/\Pi$ for different values of the aspect ratio $\mathcal{A}$. It is convenient to use $1/\Pi = -\rho g d/p_s$ as the independent variable in this graph since, with all other variables held constant, increasing $1/\Pi$ corresponds to increasing the size of the body. For $1/\Pi \ll 1$ figure 5.6 shows that $T_s \sim 1/\Pi$, which in dimensional terms indicates that $t_s \sim d^2$.

Our simulations track the position of the air–liquid interface within the porous block as well as the level at which the block floats in the exterior liquid. The evolution towards sinking is illustrated by the time series in figure 5.7.
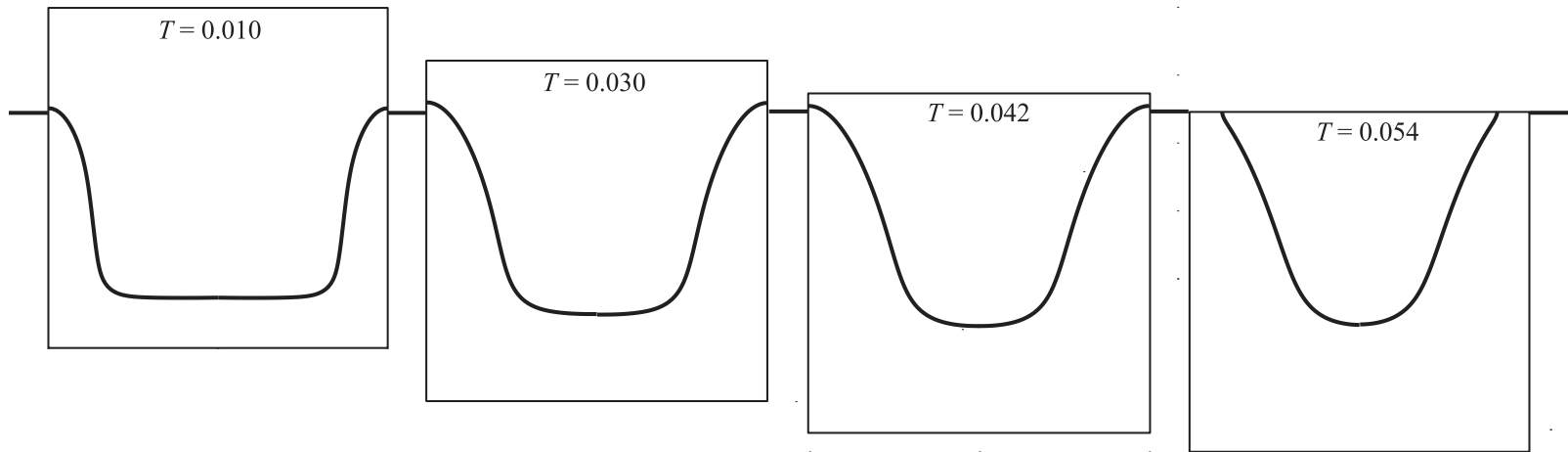
**Figure 5.7:** *Time series depicting the sinking of a square ($\mathcal{A} = 1$) porous block in simulations. The exterior level of the liquid is indicated by the horizontal lines and the curves show the position of the air–liquid interface within the block at four different times. The last of these corresponds to the instant at which the block sinks. Here $\Pi = 0.5$ and other parameters are typical of pumice, namely: $D = 2.3$ and $\phi = 0.8$ (Whitham & Sparks, 1986).*

The numerical results show that, as expected, the finite aspect ratio of a floating porous body decreases the value of $T_s$ (as compared to the one-dimensional limit considered in §5.2.2). This is because there is an additional boundary through which liquid can flow into the body. The one-dimensional model shows that for given material properties there is a maximum non-dimensional time to sink, $T_{\max}$, given by (5.13). For $1/\Pi \gg 1$, therefore, we must have $T_s \to \beta$, where $\beta < T_{\max}$ is a constant. In dimensional terms this shows that the time to sink $t_s \sim d$ for $\Pi \ll 1$. Summarizing the results for $\Pi \gg 1$ and $\Pi \ll 1$ we have:

$$t_s \sim \begin{cases} d^2 & d \ll |p_s|/\rho g, \\ d & d \gg |p_s|/\rho g. \end{cases} \tag{5.19}$$

## 5.4 Experimental results

We conducted a series of simple experiments to directly test the results of our numerical simulations. In these experiments the porous medium used was hydrophilic cellulose sponge (Sydney Heath and Son). Sponge was chosen rather than pumice because it appeared to be homogeneous and isotropic, was easy to cut into different sized pieces and could be dried quickly between runs. As with pumice, the sponge has only a limited region of partial saturation ($< 5\%$).

The porosity of the sponge was measured to be $\phi \approx 0.77$. Its permeability was measured in a dynamic capillary rise experiment: the sponge was vertically clamped and the capillary rise of dyed water through the sponge was recorded using a CCD camera. The measured height of capillary rise as a function of time agrees well with the theoretical prediction of Washburn (1921) with a value of $k/\phi = 3.4 \pm 0.2 \times 10^{-10}$ m$^2$. The maximum rise height of liquid was measured to be 2.7 cm, which corresponds to $p_s \approx -264$ Pa.

To make the sponges effectively two-dimensional, OHP transparencies were glued onto thin slices of the sponge, as shown schematically in figure 5.8. This prevents water from flowing into the sponge except through the thin open edges. To investigate how different solid densities affect the time taken to sink, we taped various metal weights to the base of the sponge without impeding the fluid flow into the sponge. The object was then placed in a bath of water and the time taken for it to sink measured. The presence of a weight at the base of the object also stabilized the object to toppling, ensuring that it remained upright throughout the experiment.

The results of these experiments, together with the predictions of our boundary integral simulations, are presented in figure 5.9. These show that there is good agreement between experiment and the theoretical predictions. We note that in the case of the smaller object
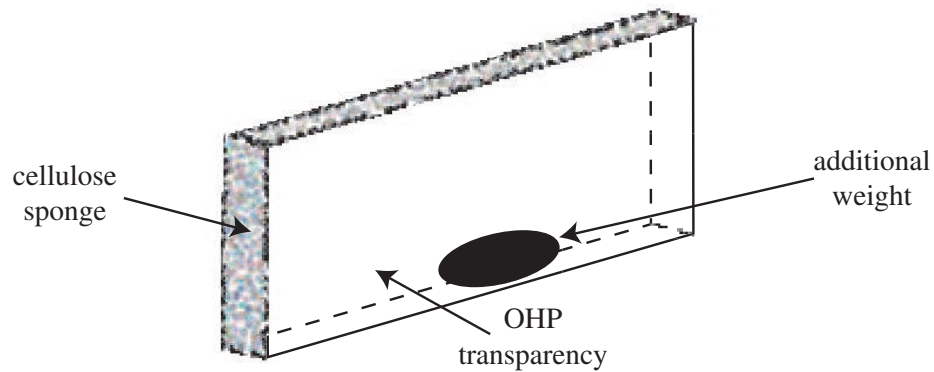
**Figure 5.8:** *Schematic illustration of the sponge sheets used in our experiments. Typically the sponge was around* 1 cm *thick with a cross section of* 10 cm × 5 cm.

(a), the theory systematically over predicts the time taken for the object to sink. This may be attributed to the early time transients in the experiment where the object is not initially in hydrostatic equilibrium. As can be seen from a graph of its level in the water (figure 5.10) the object initially oscillates about hydrostatic equilibrium. During these oscillations the object soaks up water faster than the model suggests: it initially falls below its equilibrium depth where the hydrostatic pressure is relatively high, forcing liquid in faster. This increases the weight of the object and it does not rise as far during its upward motion as it would with its initial weight. For the larger object (b), waterlogging takes longer and so these early transients are less significant; the experimental results in this case agree with theoretical predictions to within the experimental errors.

In other experiments we recorded the level of the sponge in the water as a function of time. The results of a typical run of this experiment are shown in figure 5.10 and again show good agreement with the predictions of the relevant boundary integral simulation.
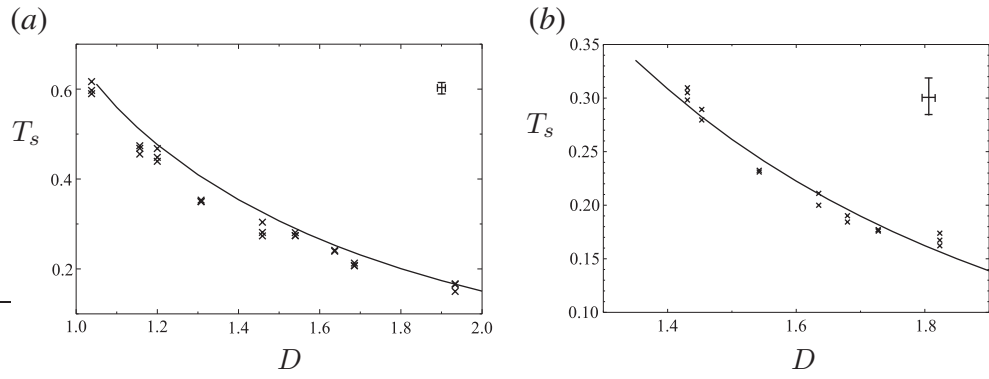
**Figure 5.9:** *The experimentally measured time taken for sponges of various effective solid densities to sink (points) compared to the predictions of our boundary integral simulations (curve). The two plots correspond to different size sponges: in (a) $\Pi \approx 0.42$ and $\mathcal{A} \approx 2.1$ while in (b) $\Pi \approx 0.26$ and $\mathcal{A} \approx 1.3$. In both cases $\phi \approx 0.77$. Typical error bars are shown in the top right hand corner of each plot.*
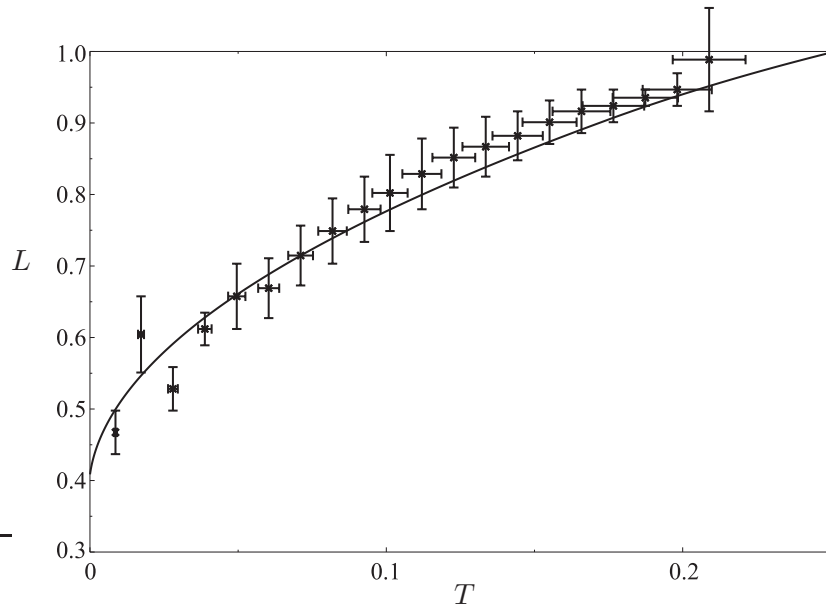


**Figure 5.10:** *The time evolution of the non-dimensional submerged body depth. Experimental results (points) compare well with the theoretical prediction (solid line). Here $\phi = 0.77$, $D = 1.64$, $\Pi = 0.42$ and $\mathcal{A} = 2.1$.*

## 5.5 Discussion

Our experimental and theoretical analyses have shown how the time taken for a porous object to sink depends on its size and material properties. The dependence of sinking time on the size of the object is particularly relevant in sedimentology. According to Manville *et al.* (1998), pumiceous sediments that formed at the bottom of a body of water are unusual in being 'inverted': that is they consist of smaller pumice fragments at the base of the sediment with increasing fragment size towards the top of the sediment. Manville *et al.* (1998) suggest that this could be explained by the smaller pumice fragments becoming waterlogged more quickly than larger fragments and so reaching the bed earlier. They explained this using an analogy between the motion of liquid in a porous medium and diffusion and therefore predicted that, in our notation, $t_s \sim d^2$. The results of our numerical simulations, summarized by the scalings in (5.19), show that this is correct for fragments that are small in comparison to the equilibrium capillary rise height in the material. For larger fragments, however, the liquid motion is driven primarily by the hydrostatic pressure head in the surrounding liquid so that $t_s \sim d$. This difference in exponents will not alter the postulated size 'inversion' of pumiceous deposits. However, it will be important in estimating the time taken to sink, which is the quantity of interest in other contexts, as we now discuss.

There are many recorded instances in which long-lived pumice 'rafts' have formed on open water shortly after volcanic eruptions. Perhaps the most famous of these instances was the Krakatoa eruption of 1883. More than six months after the eruption, individual pumice fragments as well as larger 'pumice rafts' were washed up on the east coast of Africa (Symonds, 1888)[1]. The vast distances covered by pumice in this and other instances has led to the suggestion that floating pumice and other material could act as a means of biological dispersal carrying plants and even small animals between distant continents (McBirney & Williams, 1969; Heyligers, 2001). Indeed, field studies by Jokiel (1989) have shown that marine organisms (including coral colonies) are commonly brought into the Kwajalein Atoll (Marshall Islands) onboard floating pumice.

For biological dispersal via pumice to be feasible, pumice fragments must typically remain afloat for long periods of time. While this longevity has been observed numerous times in the field, there are no quantitative estimates of how long we might expect, on fluid mechanical grounds, pumice to remain afloat. In general, this will depend on the strength of surface tension in driving the flow. However, from figure 5.6 we see that $T_s \leq \mathcal{O}(1)$ for

---

[1] Several eyewitness accounts of these pumice rafts, as well as descriptions of the cargo that they carried with them, are collected in the popular book about Krakatoa by Winchester (2003).

| Expt. | Symbol | $\tilde{d}$ (cm) |
|:-----:|:------:|:----------------:|
| $M1$  | $+$    | 4.82             |
| $M2$  | $\times$ | 3.67           |
| $M3$  | $\bigcirc$ | 2.93         |
| $M4$  | $\square$ | 2.25          |

**Table 5.1:** *Effective sizes, $\tilde{d}$, of the four pumice clasts investigated by Whitham & Sparks (1986) analyzed here. The experiment number is that used in Whitham & Sparks (1986) while the symbol is that used to represent each clast in figure 5.11.*

all values of the surface tension strength $\Pi$. Given the non-dimensionalization of time in (5.3), we therefore expect that

$$t_s \le O\left(\frac{d\phi\mu}{k\rho g}\right). \tag{5.20}$$

Klug & Cashman (1996) found that pumice typically has $k \gtrsim 10^{-14}$ m$^2$. which then suggests that $t_s \le \mathcal{O}(1)$ day for $d = 1$ cm. However, the experiments of Manville *et al.* (1998) and Whitham & Sparks (1986) both show that pumice fragments of this size actually float for $\mathcal{O}(10^3)$ hrs $\approx \mathcal{O}(40)$ days before sinking. This discrepancy is interesting because our own experiments with pieces of sponge found good agreement between experiment and theory.

To resolve this discrepancy, we test some other predictions of our model using the data provided by Whitham & Sparks (1986). They performed a series of experiments on different sized cuboids cut from a single piece of pumice from the Minoan eruption of Santorini. We shall therefore assume that the material properties of each sample are the same. Whitham & Sparks (1986) only report the volume of each cuboid, not its aspect ratio. We therefore estimate the effective depth of a given cuboid, $\tilde{d}$, as the cube root of its volume. Whitham & Sparks (1986) dropped seven such cuboids into a beaker of water and measured their density at points during the next one and a half years. Because of various discrepancies between the results tabulated and those plotted by Whitham & Sparks (1986) for the three smallest clasts, we consider only the four largest clasts here. The size of each of these clasts is given in table 5.1.

Figure 5.11 shows how the bulk clast density, $L$, increases in time. Here, time has been rescaled by the effective clast size $\tilde{d}$, which is motivated by the scaling $t^* \sim d$. In plotting the data of Whitham & Sparks (1986) we have neglected their estimate for the amount of water lost from the pumice by removing it from the beaker.

Expanding the analytical one-dimensional result (5.11) for $T \ll 1$ we find that

$$L \approx D(1-\phi) + \phi\left[2(1-\phi)\Pi_e\right]^{1/2} T^{1/2}. \tag{5.21}$$
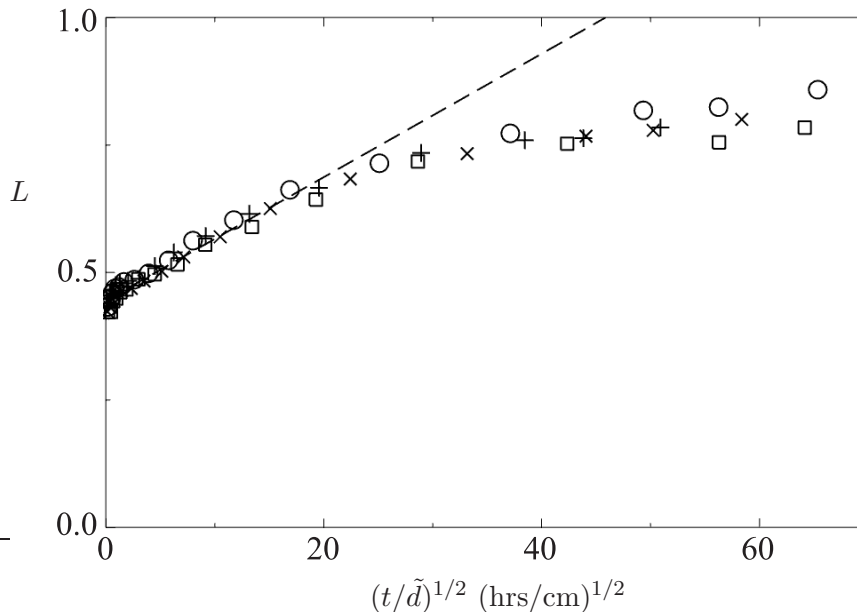
**Figure 5.11:** *The waterlogging of pumice measured by Whitham & Sparks (1986). The dimensionless bulk density of each clast (in our notation, L) is plotted as a function of rescaled time, $(t/\tilde{d})^{1/2}$ where $\tilde{d}$ is the effective size of the clast. The symbol for each pumice clast is as in table 5.1. Raw data taken from Whitham & Sparks (1986). The dashed line shows the best fit line for short times (5.22).*

This suggests that we should plot $L$ as a function of $(t/\tilde{d})^{1/2}$, as has been done in figure 5.11.

Figure 5.11 shows a reasonable collapse of the data for different sized samples cut from a single piece of pumice. This plot also shows the diffusive growth of $L$ at early times predicted by (5.21). The collapse of the experimental data over a range of values of $\tilde{d}$ suggests that $p_s/\rho g \tilde{d} \ll 1$: otherwise $\Pi_e = D - p_s/\left[\rho g \tilde{d}(1-\phi)\right]$ would vary considerably as $\tilde{d}$ varies and the data would not collapse. We therefore conclude that in this instance waterlogging is driven primarily by hydrostatic pressure, rather than surface tension.

The dashed line in figure 5.11 shows the line

$$L = 0.445 + 0.0123 \left(\frac{t}{\tilde{d}}\right)^{1/2}. \tag{5.22}$$

The gradient of this line is the mean of the gradients of the best fit lines for each individual clast, which have standard deviation $7.5 \times 10^{-4}$ (cm/hrs)$^{1/2}$ about this mean.

From the gradient in (5.22) and the one-dimensional result (5.21) we obtain an order of magnitude estimate for the permeability $k \sim 10^{-16}$ m$^2$. We cannot estimate $k$ more precisely since the dimensionless constants that appear in (5.21) are correct only for one-dimensional pumice! However, we note that this estimate is a factor of 100 smaller than

the value of $k$ given by Klug & Cashman (1996). This smaller $k$ increases our estimate of the sinking time (bringing it into line with the data of Whitham & Sparks, 1986) and suggests that some pumice samples have much lower permeability than was previously thought.

# Gravity Currents in a Porous Medium at an Inclined Plane

> And I will show you something different...
>
> *(T. S. Eliot, The Waste Land)*

## Synopsis

We consider the release from a point source of relatively heavy fluid into a saturated porous medium above an impermeable slope. We consider the case where the volume of the resulting gravity current increases with time like $t^\alpha$ and show that for $\alpha < 3$, at short times the current spreads axisymmetrically, with radius $r \sim t^{(\alpha+1)/4}$, while at long times it spreads predominantly downslope. In particular, for long times the downslope position of the current is proportional to $t$, while the current extends a distance proportional to $t^{\alpha/3}$ across the slope. For $\alpha > 3$, this situation is reversed with spreading occurring predominantly downslope for short times. The governing equations admit similarity solutions whose scaling behaviour we determine, with the full similarity form being evaluated by numerical computations of the governing partial differential equation. We find that the results of these analyses are in good quantitative agreement with a series of laboratory experiments. Finally, we discuss the implications of our work for the sequestration of carbon dioxide in aquifers with a sloping, impermeable cap.

## 6.1 Introduction

Horizontal differences in density between two fluids lead to the propagation of so-called gravity currents. These currents are of interest in a number of industrial as well as natural applications and so obtaining an understanding of the way in which they propagate is a subject that has motivated a considerable amount of current research (see Huppert, 2006, for a review).

Previously, our understanding of axisymmetric viscous gravity currents on an impermeable boundary (Huppert, 1982) has been generalized to take account of the effects of a slope (Lister, 1992) as well as the propagation of a current in a porous medium (Huppert & Woods, 1995; Lyle *et al.*, 2005). In this chapter, we consider the propagation of a gravity current from a point source in a porous medium at an impermeable sloping boundary. Of particular interest is the evolution of the current away from the axisymmetric similarity solution found by Lyle *et al.* (2005). This is a situation that has significant implications in the field of carbon dioxide sequestration, which we will discuss below.

We begin by deriving the evolution equations for the shape of a current whose volume varies in time like $qt^\alpha$. A scaling analysis of these governing equations reveals the extent of the current as a function of time up to a multiplicative constant. The full form of the similarity solutions that give rise to these scalings can only be determined by numerical means, however, and to do so we modify the numerical code of Lister (1992). For some particular values of $\alpha$, it is possible to make analytical progress; these cases are considered separately in §6.3 and provide a useful check of the numerical scheme. We then compare the results of the numerical calculations to a series of experiments in §6.4 and find good quantitative agreement between the two. Finally, in §6.5, we discuss the implications of our results in geological settings, with particular emphasis on the implications of our work for the geological sequestration of carbon dioxide.

A paper based on the work described in this chapter has been published in the *Journal of Fluid Mechanics* (Vella & Huppert, 2006). This work is in collaboration with Herbert Huppert.

## 6.2 Formulation

### 6.2.1 Governing equations

We consider a gravity current consisting of fluid material of density $\rho + \Delta\rho$ in an infinitely deep porous medium saturated with fluid of density $\rho$, which is bounded by an impermeable barrier at an angle $\theta$ to the horizontal (see figure 6.1 for a sketch of the setup). That
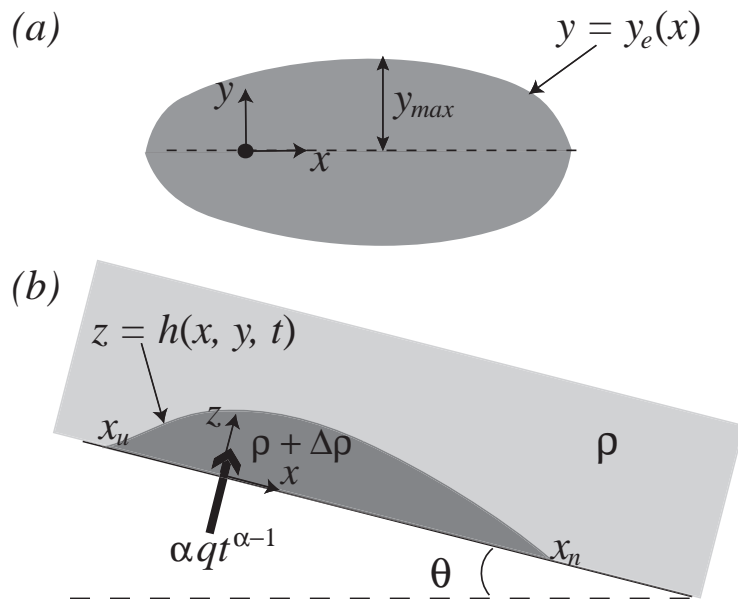
**Figure 6.1:** *Sketches of a gravity current, of density $\rho + \Delta\rho$, propagating in a porous medium saturated with liquid of density $\rho$ above an inclined plane. (a) Plan view of the current and (b) horizontal section through the current.*

the saturated porous medium is deep in comparison with the vertical extent of the current allows us to neglect the motion of the surrounding fluid, simplifying the problem considerably. We use the natural Cartesian co-ordinate system centred on the mass source and aligned with the slope of the impermeable boundary. The depth, $h(x, y, t)$, of the gravity current is then determined by continuity combined with Darcy's law (see Bear, 1988, for example) and the assumption that the pressure, $P$, in the current is hydrostatic, i.e.

$$P - P_0 = \Delta\rho g h \cos\theta - (\rho + \Delta\rho)gz\cos\theta + \rho g x \sin\theta \quad (z < h), \tag{6.1}$$

with $P_0$ constant and $g$ being the acceleration due to gravity. This assumption is valid provided that the aspect ratio of the current (depth/length) remains small (Huppert & Woods, 1995). Here, Darcy's law takes the form

$$\boldsymbol{u} = -\frac{k}{\mu}\left[\boldsymbol{\nabla}P - (\rho + \Delta\rho)g(\sin\theta, 0, -\cos\theta)\right], \tag{6.2}$$

where $k$ is the permeability of the porous medium (assumed uniform) and $\mu$ is the viscosity of the liquid. The Darcy velocity within the porous medium is therefore given by

$$\boldsymbol{u} = -\frac{k\Delta\rho g}{\mu}\left(-\sin\theta + \cos\theta\frac{\partial h}{\partial x}, \cos\theta\frac{\partial h}{\partial y}, 0\right). \tag{6.3}$$

Using this along with the conservation of mass, we obtain

$$\frac{\partial h}{\partial t} = \frac{k\rho g'}{\mu\phi} \left( \frac{\cos\theta}{2} \nabla^2 h^2 - \sin\theta \frac{\partial h}{\partial x} \right), \tag{6.4}$$

where $\phi$ is the porosity of the porous medium and

$$g' \equiv g\Delta\rho/\rho \tag{6.5}$$

is the reduced acceleration due to gravity. Equation (6.4) is a nonlinear advection–diffusion equation for the current thickness $h(x,y,t)$, with the two terms on the right hand side representing the gravity-driven spreading of the current and its advection downslope, respectively.

It is common to close the system by requiring that the volume of the current depend on time like $qt^\alpha$ for some constant $\alpha \geq 0$ (Huppert, 1982; Lister, 1992; Huppert & Woods, 1995). This constraint leads to solutions of self-similar form (as we shall see again in this case) but also covers the natural cases of a fixed volume release ($\alpha = 0$) and a constant flux release ($\alpha = 1$). To impose this volume constraint, (6.4) must be solved along with

$$\phi \int_{x_u}^{x_n} \int_{-y_e(x)}^{y_e(x)} h \, \mathrm{d}y \, \mathrm{d}x = qt^\alpha, \tag{6.6}$$

with $|y| = y_e(x)$ giving the edge of the current for $x_u(t) < x < x_n(t)$. Note that (6.6) contains an extra multiplicative factor of $\phi$, which was erroneously omitted in the study of an axisymmetric current in a porous medium by Lyle *et al.* (2005).

Equations (6.4) and (6.6) may be non-dimensionalized by setting $T = t/t^*$, $H = h/h^*$, $X = x/x^*$ and $Y = y/y^*$, where

$$t^* \equiv \left( \frac{q}{\phi V^3 \tan\theta} \right)^{\frac{1}{3-\alpha}}, \quad x^* = y^* \equiv Vt^*, \quad h^* \equiv x^* \tan\theta, \tag{6.7}$$

and

$$V \equiv \frac{k\rho g' \sin\theta}{\mu\phi} \tag{6.8}$$

is the natural velocity scale in the problem. In non-dimensional terms, therefore, the current satisfies

$$\frac{\partial H}{\partial T} = \boldsymbol{\nabla} \cdot (H\boldsymbol{\nabla}H) - \frac{\partial H}{\partial X}, \tag{6.9}$$

along with the volume conservation constraint

$$\int_{X_u}^{X_n} \int_{-Y_e(X)}^{Y_e(X)} H \, \mathrm{d}Y \, \mathrm{d}X = T^\alpha. \tag{6.10}$$

## 6.2.2 Scalings

To aid our physical understanding of spreading of the gravity current, we begin by considering the scaling behaviour of the spreading in the limits of short and long times. Two different spreading regimes are observed depending on which of the two downslope velocity terms in (6.3) dominate. When $h_x \gg \tan\theta$ ($H_X \gg 1$), the typical horizontal velocity scale is $X_n/T \sim H/X_n$ so that $H \sim X_n^2/T$. Further, $X_n \sim Y_{\max}$ and volume conservation (6.10) requires that $HX_nY_{\max} \sim T^\alpha$. From this we therefore find the axisymmetric scalings obtained by Lyle *et al.* (2005), namely

$$H \sim T^{\frac{\alpha-1}{2}}, \quad X_n \sim Y_{\max} \sim T^{\frac{\alpha+1}{4}}. \tag{6.11}$$

When $h_x \ll \tan\theta$ ($H_X \ll 1$), (6.3) gives a typical downslope velocity of the current as $X_n/T \sim 1$ while in the across-slope direction we have $Y_{\max}/T \sim H/Y_{\max}$. Combined with volume conservation $HX_nY_{\max} \sim T^\alpha$ these scalings lead to

$$H \sim T^{\frac{2\alpha-3}{3}}, \quad X_n \sim T, \quad Y_{\max} \sim T^{\frac{\alpha}{3}}, \tag{6.12}$$

so that the current spreads predominantly downslope. It is worth noting here that the long time scaling $X_n \sim T$ is unsurprising because (6.9) may be simplified by moving into a frame moving at unit speed downslope (Huppert & Woods, 1995). We also note that the scaling $Y_{\max} \sim T^{\alpha/3}$ is identical to that found by Lister (1992) for a viscous current on a slope. In fact, this scaling is generic in these problems, being recovered whenever the fluid flux is proportional to some power of the current height, $H$, as shown in Appendix 6.A of this chapter.

Note that to observe axisymmetric spreading we require $h_x \gg \tan\theta$. For this condition to be consistent with the thin layer assumption used to derive (6.4) we therefore require $\tan\theta \ll 1$. Asymmetric spreading, on the other hand, ensures that $h_x \ll 1$ and we do not need to assume that $\theta \ll 1$ in this case.

From the scalings in (6.11) and (6.12) we see that

$$H_X \sim \frac{H}{X_n} \sim \begin{cases} T^{(\alpha-3)/4}, & H_X \gg 1 \\ T^{2(\alpha-3)/3}, & H_X \ll 1. \end{cases} \tag{6.13}$$

When $\alpha < 3$, therefore, we find axisymmetric spreading at short times ($T \ll 1$) and asymmetric spreading at long times ($T \gg 1$). When $\alpha > 3$, the importance of the two downslope terms (the diffusive and translational terms) reverses and we recover the axisymmetric spreading scalings given in (6.11) as being relevant for $T \gg 1$. Conversely,

| Regime | | Downslope extent $x_n$ | Cross-slope extent $y_{\max}$ | Thickness $h$ |
|---|---|---|---|---|
| $\alpha < 3$ | $t \ll t^*$ | $\sim \left(\frac{Vq}{\phi\tan\theta}\right)^{1/4} t^{(\alpha+1)/4}$ | $\sim \left(\frac{Vq}{\phi\tan\theta}\right)^{1/4} t^{(\alpha+1)/4}$ | $\sim \left(\frac{q\tan\theta}{\phi V}\right)^{1/2} t^{(\alpha-1)/2}$ |
| $\alpha < 3$ | $t \gg t^*$ | $\sim Vt$ | $\sim \left(\frac{q}{\phi\tan\theta}\right)^{1/3} t^{\alpha/3}$ | $\sim \left(\frac{q^2\tan\theta}{\phi^2 V^3}\right)^{1/3} t^{(2\alpha-3)/3}$ |
| $\alpha > 3$ | $t \ll t^*$ | $\sim Vt$ | $\sim \left(\frac{q}{\phi\tan\theta}\right)^{1/3} t^{\alpha/3}$ | $\sim \left(\frac{q^2\tan\theta}{\phi^2 V^3}\right)^{1/3} t^{(2\alpha-3)/3}$ |
| $\alpha > 3$ | $t \gg t^*$ | $\sim \left(\frac{Vq}{\phi\tan\theta}\right)^{1/4} t^{(\alpha+1)/4}$ | $\sim \left(\frac{Vq}{\phi\tan\theta}\right)^{1/4} t^{(\alpha+1)/4}$ | $\sim \left(\frac{q\tan\theta}{\phi V}\right)^{1/2} t^{(\alpha-1)/2}$ |

**Table 6.1:** *Summary of the asymptotic scalings for the dimensions of a gravity current in a porous medium at an inclined plane. Here dimensional notation is used for clarity, and $t^*$ and $V$ are as defined in (6.7) and (6.8), respectively.*

for $T \ll 1$ we recover the non-axisymmetric scalings of (6.12). A summary of the different scaling regimes expected is given in dimensional terms in table 6.1.

That we observe axisymmetric spreading if $\alpha > 3$ and $T \gg 1$ is surprising, but is a consequence of the fact that the downslope flux in a porous medium gravity current is only weakly dependent on the local height and so can be swamped by the spreading terms in (6.9). In the viscous case, this is not possible because the downslope flux is able to remove the incoming flux much more efficiently and penalizes the accumulation of material at a particular point more. A scaling analysis addressing the difference between these two cases is given in Appendix 6.A.

The importance of the case $\alpha = 3$ as a transition between qualitatively different flow regimes is reminiscent of earlier work on gravity currents. For an axisymmetric gravity current, Huppert (1982) found that viscous forces dominate inertia at long times for $\alpha < 3$ (being insignificant at short times) with the situation reversed for $\alpha > 3$. Acton *et al.* (2001) found that a viscous gravity current propagating over a permeable medium spreads only a finite distance if $\alpha < 3$ but spreads indefinitely for $\alpha > 3$. Despite these similarities, the reappearance of a transition at $\alpha = 3$ here is purely coincidental.

### 6.2.3 Numerics

The axisymmetric spreading of a gravity current in a porous medium above a horizontal plane was considered by Lyle *et al.* (2005). In particular, they determined the coefficients in the scalings (6.11) by finding a solution dependent on one similarity variable in this case. To determine the prefactors in the non-axisymmetric scaling relations (6.12), it is necessary to resort to numerical solutions of (6.9) and (6.10). The numerical code I used to do this was adapted from that used by Lister (1992) for a viscous gravity current on an inclined plane, with minor alterations to make it applicable to a gravity current in a porous
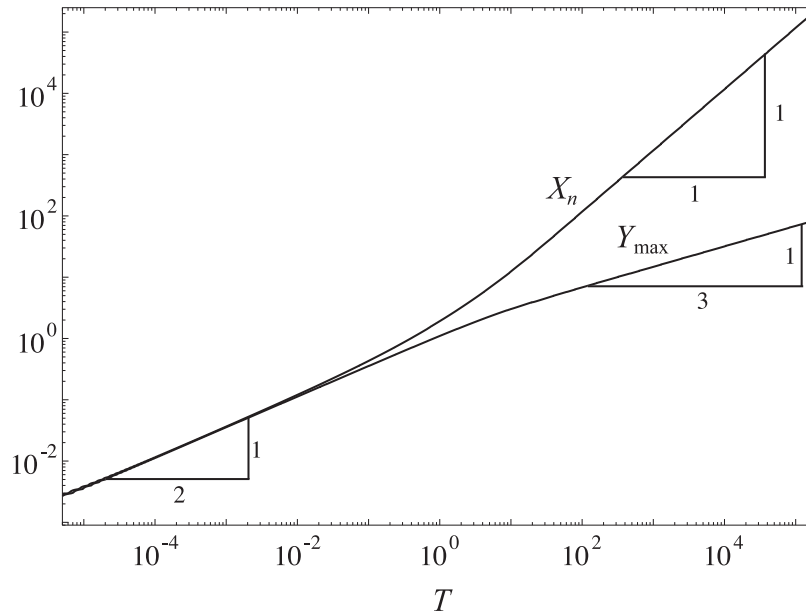
**Figure 6.2:** *Numerically computed evolution of the extent of a constant flux current ($\alpha = 1$) showing the transition from axisymmetric spreading when $T \ll 1$ to asymmetric spreading when $T \gg 1$. The numerical results reproduce the scalings (6.11) and (6.12).*

medium. This code is an implementation of a finite-difference scheme on a rectangular grid with time-stepping performed using an alternating-direction-implicit method. Equation (6.9) was written in flux-conservative form allowing the diffusive and advective terms to be represented by the Il'in scheme (Clauser & Kiesner, 1987). More details of the numerical scheme may be found in Lister (1992).

Typical numerical results are shown in figure 6.2 for the case of a constant flux current ($\alpha = 1$). This shows that we observe the scalings (6.11) when $T \ll 1$ and (6.12) when $T \gg 1$, as expected.

## 6.3 Special values of $\alpha$

In this section, we consider separately particular values of $\alpha$ that are of special interest. In some of these cases, it is possible to make progress analytically providing useful checks on the numerical scheme discussed in §6.2.3, but they also shed light on situations of practical interest.

### 6.3.1 Constant volume

As already noted, the differential equation in (6.9) may be simplified by moving into a frame translating at unit speed downslope. However, for general values of $\alpha$, this corresponds to a point source that is moving uphill in the new frame, complicating the analysis.

For a current of constant volume, $\alpha = 0$, there is no distinguished source point and we let $X' \equiv X - T$. The resulting transformation of (6.9) has an axisymmetric similarity solution (Lyle *et al.*, 2005), which may be written

$$H(X, Y, T) = \frac{1}{8T^{1/2}} \left( \frac{4}{\sqrt{\pi}} - \frac{R'^2}{T^{1/2}} \right), \tag{6.14}$$

where $R' \equiv (X'^2 + Y^2)^{1/2}$.

## 6.3.2 Constant flux: A steady state

For very long times $T \ggg 1$, we expect that a constant flux current (corresponding to $\alpha = 1$) will approach a steady state, whose shape we now determine. We expect this steady shape to be observed far from the nose of the current, since the nose is always unsteady, requiring that $X \ll T$. Sufficiently far downstream from the source ($X \gg 1$), the steady shape is given by

$$\frac{\partial^2 H^2}{\partial Y^2} = 2\frac{\partial H}{\partial X}, \tag{6.15}$$

which has a similarity solution of the form $H(X, Y) = X^{-1/3}f(Y/X^{1/3})$ where the function $f$ satisfies

$$\frac{\mathrm{d}^2 f^2}{\mathrm{d}\eta^2} + \frac{2}{3}\left( f + \eta\frac{\mathrm{d}f}{\mathrm{d}\eta} \right) = 0, \quad \int_{-\eta_e}^{\eta_e} f \, \mathrm{d}\eta = 1, \quad f(\pm\eta_e) = 0. \tag{6.16}$$

This has solution

$$f(\eta) = \frac{1}{6}(\eta_e^2 - \eta^2), \tag{6.17}$$

where $\eta_e = (9/2)^{1/3} \approx 1.651$ denotes the position of the current edge in similarity variables. This limiting solution is also given by Woods (1999) without any further discussion.

This result shows that far away from the source and nose regions, we should expect the boundary of unsteady currents to approach $Y = (9X/2)^{1/3}$. Superimposing this curve onto the numerically calculated current provides a useful check of the numerical scheme described in §6.2.3. This comparison (see figure 6.3) shows that, away from both the nose and source regions, we do indeed see the steady state boundary shape, though this region is confined to $T^{-1} \ll X/T \ll 1$ in the rescaled co-ordinates used in figure 6.3.

It is interesting to note that the similarity solution (6.17) is precisely that given by Huppert & Woods (1995) for the shape of a two-dimensional current of constant volume spreading in a porous medium above a horizontal boundary. This correspondence arises because in the steady state case considered here, fluid moves downslope at a constant velocity — independently of its cross-slope position and the local current height — so
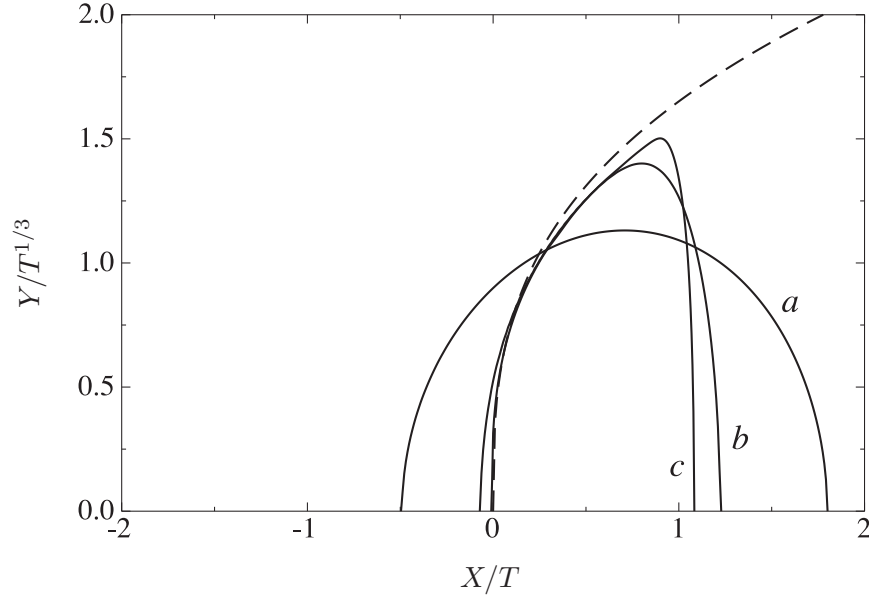
**Figure 6.3:** *Numerical evolution of the boundary of a constant flux current ($\alpha = 1$) in rescaled co-ordinates at (a) $T = 1.23$, (b) $T = 9.52$ and (c) $T = 270.9$. The last of these is indistinguishable from the steady state shape that is found at long times in these rescaled variables. The similarity solution for the steady shape in the interior is given by $Y = (9X/2)^{1/3}$ (dashed line) and is valid away from the source and the front regions, which in these rescaled variables requires that $T^{-1} \ll X/T \ll 1$.*

that $X$ is a proxy for time. A material slice in the $y$–$z$ plane thus remains planar as it is advected downslope and so spreads laterally in exactly the same way that a fixed volume release does in two dimensions.
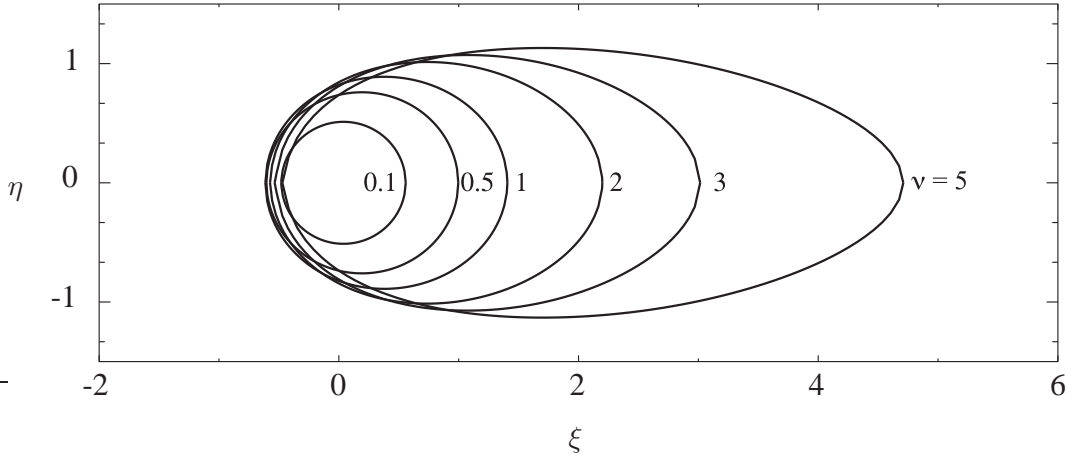
### 6.3.3 $\alpha = 3$

When $\alpha = 3$, the non-dimensionalization leading to (6.9) breaks down because there is no longer a characteristic time scale $t^*$ of the motion. Instead, an additional natural velocity scale, $(q/\phi)^{1/3}$, enters the problem. We thus define a new set of dimensionless variables $\tilde{T} = t/\tilde{t}^*$, $\tilde{H} = h/\tilde{h}^*$, $\tilde{X} = x/\tilde{x}^*$ and $\tilde{Y} = y/\tilde{y}^*$ where $\tilde{t}^*$ is an arbitrary time scale and

$$\tilde{x}^* = \tilde{y}^* \equiv \left( \frac{q}{\phi \tan \theta} \right)^{1/3} \tilde{t}^*, \quad \tilde{h}^* \equiv \tilde{x}^* \tan \theta. \tag{6.18}$$

In these non-dimensional variables, the system becomes

$$\frac{\partial \tilde{H}}{\partial \tilde{T}} = \nu \left( \boldsymbol{\nabla} \cdot (\tilde{H} \boldsymbol{\nabla} \tilde{H}) - \frac{\partial \tilde{H}}{\partial \tilde{X}} \right), \tag{6.19}$$

**Figure 6.4:** *Numerical results showing the boundaries of currents with $\alpha = 3$ obtained by solving (6.22) and (6.23) for six values of the parameter $\nu$. Labels refer to the value of $\nu$ for each current.*

along with volume conservation in the form

$$\int_{\tilde{X}_u}^{\tilde{X}_n} \int_{-\tilde{Y}_e(\tilde{X})}^{\tilde{Y}_e(\tilde{X})} \tilde{H} \; \mathrm{d}\tilde{Y} \; \mathrm{d}\tilde{X} = \tilde{T}^3, \tag{6.20}$$

where

$$\nu \equiv V(\phi \tan \theta / q)^{1/3} \tag{6.21}$$

is essentially the ratio of the two velocity scales in the problem. By substituting $\tilde{H} = \tilde{T}\mathcal{H}(\xi, \eta)$ with $\tilde{X} = \tilde{T}\xi$ and $\tilde{Y} = \tilde{T}\eta$, time can be eliminated from this problem entirely so that $\mathcal{H}$ is the solution of the two-dimensional problem

$$3\mathcal{H} = \left[\mathcal{H}\{\xi + \nu(\mathcal{H}_\xi - 1)\}\right]_\xi + \left[\mathcal{H}(\eta + \nu\mathcal{H}_\eta)\right]_\eta, \tag{6.22}$$

(with subscripts denoting differentiation) and

$$\int_{\xi_u}^{\xi_n} \int_{-\eta_e}^{\eta_e} \mathcal{H} \; \mathrm{d}\eta \; \mathrm{d}\xi = 1. \tag{6.23}$$

The system (6.22) and (6.23) was solved by time-stepping the problem in (6.19) and (6.20) using a minor modification of the code described in §6.2.3. This was found to be a convenient method of solution and also demonstrates that time-dependent solutions converge on the time-independent solution. The results of this calculation are shown in figure 6.4 for a number of different values of $\nu$.
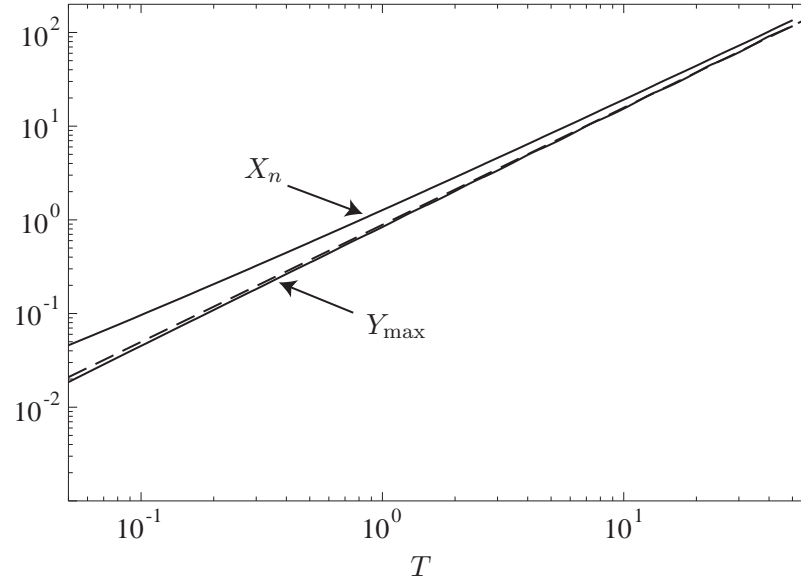
**Figure 6.5:** *Numerical results for the positions of the current edge $X_n$ and $Y_{\max}$ as a function of time $T$ for $\alpha = 4$ (solid lines). For $T \gg 1$ these obey the axisymmetric spreading relationship, $X_n, Y_{\max} \approx 0.8855T^{5/4}$ (dashed line), that we expect from the axisymmetric analysis of Lyle* et al. *(2005).*

### 6.3.4 $\alpha > 3$

In §6.2.2, we observed that for $\alpha > 3$ a scaling analysis suggests that we should observe axisymmetric spreading for $T \gg 1$. For such values of $\alpha$, therefore, we expect to recover the axisymmetric solutions given by Lyle *et al.* (2005) in our numerical simulations. In particular, for $\alpha = 4$ we would expect to find that

$$X_n, Y_{\max} \approx 0.8855T^{5/4},$$

where the prefactor here has been determined by repeating the analysis of Lyle *et al.* (2005). As shown in figure 6.5, this result is indeed obtained from our numerical results.

## 6.4 Experimental results

I conducted experiments in which a saline solution (dyed red) was injected at constant flux ($\alpha = 1$) into the base of a porous medium saturated with fresh water. The details of the experimental setup are as described by Lyle *et al.* (2005). In summary, the experiments were performed in a square-based Perspex tank of internal side length 61 cm and height 41 cm. The porous medium consisted of a self-supported matrix of glass ballotini (diameter 3 mm), which filled the tank to a height of 25 cm. In contrast to the experiments of Lyle

| Expt. | Symbol | $g'$ ($\mathrm{cm\,s^{-2}}$) | $q$ ($\mathrm{cm^3\,s^{-1}}$) | $\theta$ (°) | $t^*$ (s) | $x^*$ (m) | $h^*$ (m) |
|-------|--------|------|------|------|-------|-------|-------|
| 1 | △ | 91 | 2.14 | 9.5 | 40.5 | 0.112 | 0.019 |
| 2 | □ | 99 | 1.31 | 10 | 25.2 | 0.080 | 0.014 |
| 3 | ◇ | 99 | 3.04 | 18 | 11.9 | 0.067 | 0.022 |
| 4 | ● | 99 | 4 | 18 | 13.7 | 0.077 | 0.025 |
| 5 | ■ | 99 | 5.78 | 18 | 16.5 | 0.093 | 0.030 |
| 6 | ★ | 91 | 3.86 | 5 | 196.2 | 0.286 | 0.025 |

**Table 6.2:** *Parameter values investigated in the six experiments presented here as well as the symbol used to represent their results in figure 6.7.*
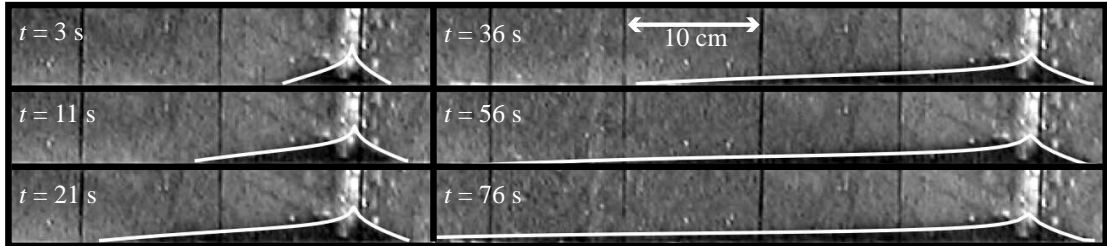


**Figure 6.6:** *Comparison between the current profiles (dark) observed in Experiment 3 and those predicted by numerical computation (superimposed white lines).*

*et al.* (2005), the Perspex tank was tilted (so that the gravity current was propagating on a slope) and the saline solution was injected at the edge of the tank, away from the corner because the inherent symmetry is different here to that of the axisymmetric case. Video footage of the motion was captured using a CCD camera and measurements of the front distance down slope $x_n$ as well as the maximum lateral extent of the current $y_{\max}$ were made using the image analysis software ImageJ[1]. The details of the six different combinations of $g'$, $q$ and $\theta$ investigated are given in table 6.2, along with the relevant values of the typical scales $t^*$, $x^*$ and $h^*$. The latter estimates are based on the measurements of $\phi = 0.37$ and $k = 6.8 \times 10^{-9}$ m$^2$ given by Lyle *et al.* (2005). The experimental results of Lyle *et al.* (2005) are in very good agreement with theory once the additional factor of $\phi$ in (6.6) is included. We therefore believe these values of $\phi$ and $k$ to be correct.

Figure 6.7 shows that the experimental results are in good agreement with the theoretical results produced by solving (6.9). The comparison between experimentally observed current profiles and those predicted from theoretical solutions of (6.9) shown in figure 6.6 is also favourable — particularly away from the source region. Two possible mechanisms may account for the slight discrepancy between experiments and theory observed: the drag exerted by the solid substrate on the current and the fact that the pore Reynolds number in our experiments is typically $\mathcal{O}(5)$. Such a value of the pore Reynolds number suggests that we may be approaching the regime where Darcy's law begins to break down,

---

[1]ImageJ is distributed by the National Institutes of Health and may be downloaded from: `http://rsb.info.nih.gov/ij/`
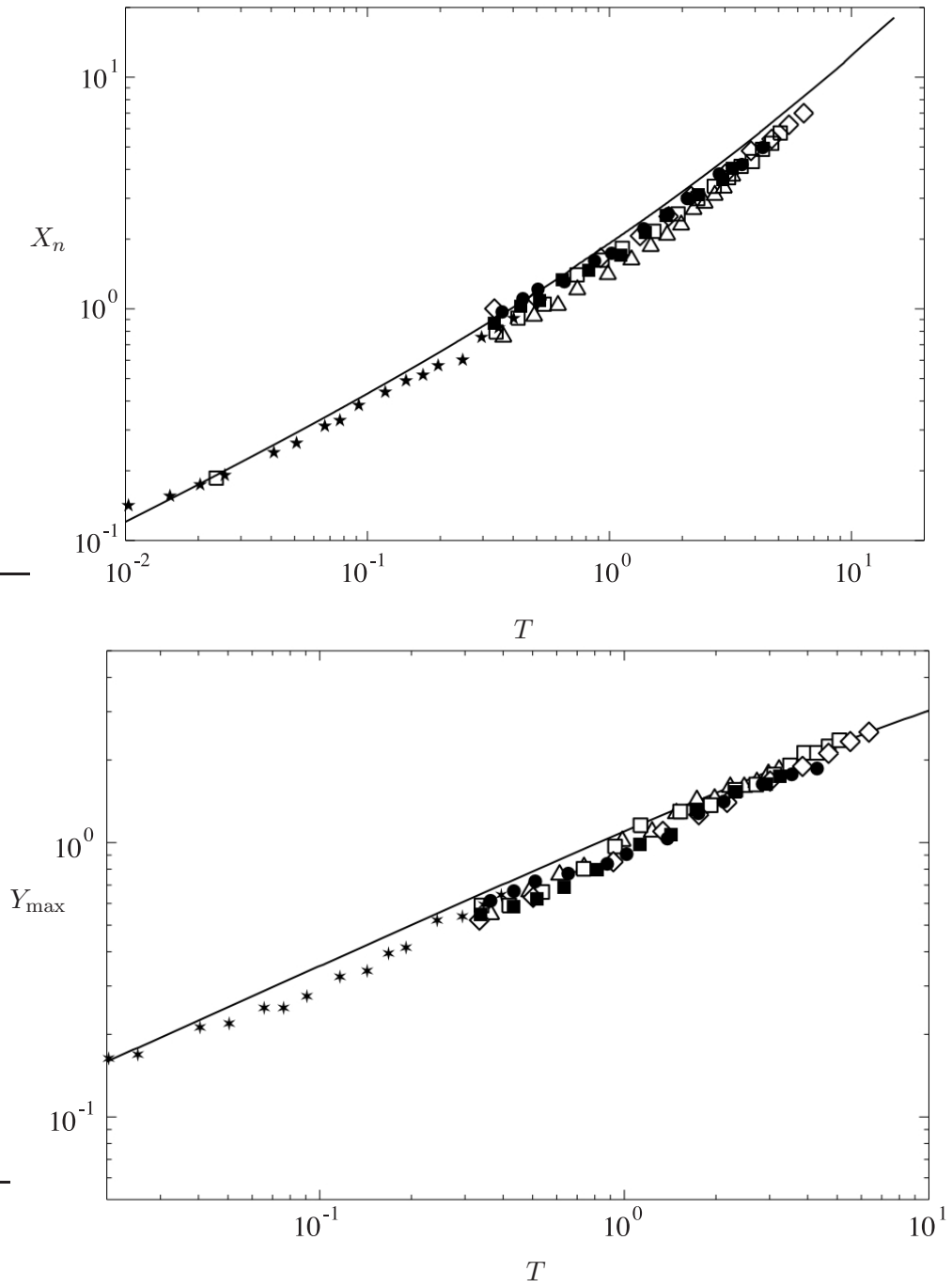
**Figure 6.7:** *Numerical (solid line) and experimental (points) results for the position of the nose of the current, $X_n$, and the maximum horizontal extent of the current, $Y_{\max}$, as functions of time for a constant flux gravity current ($\alpha = 1$). The symbols used to represent each experimental run are given in table 6.2.*

which is around Re = 10 (Bear, 1988).

## 6.5 Discussion

In this chapter, we have shown that shortly after the initiation of a gravity current with $\alpha < 3$ the current spreads axisymmetrically in the manner described by Lyle *et al.* (2005). However, at times much longer than the characteristic time $t^*$ given in (6.7), the current loses its axisymmetry and propagates predominantly downslope. Our theoretical analyses have been confirmed by a series of laboratory experiments in the case $\alpha = 1$.

At long times, a current with $\alpha = 1$ propagates at constant velocity along the slope. In the asymmetric phase, the current propagates much faster downslope than would be the case if it remained axisymmetric. The time scale $t^*$ over which the asymmetry develops is, therefore, of particular interest to those trying to predict the course of such a current in any practical application.

One such application is the geological sequestration of carbon dioxide in which super-critical carbon dioxide is pumped into aquifers. It is hoped that storing carbon dioxide in this way may ameliorate the effects of climate change. There are several sites where geological carbon sequestration is already being implemented on an industrial scale, one of the best studied being the Sleipner field in Norway (Bickle *et al.*, 2007; Chadwick
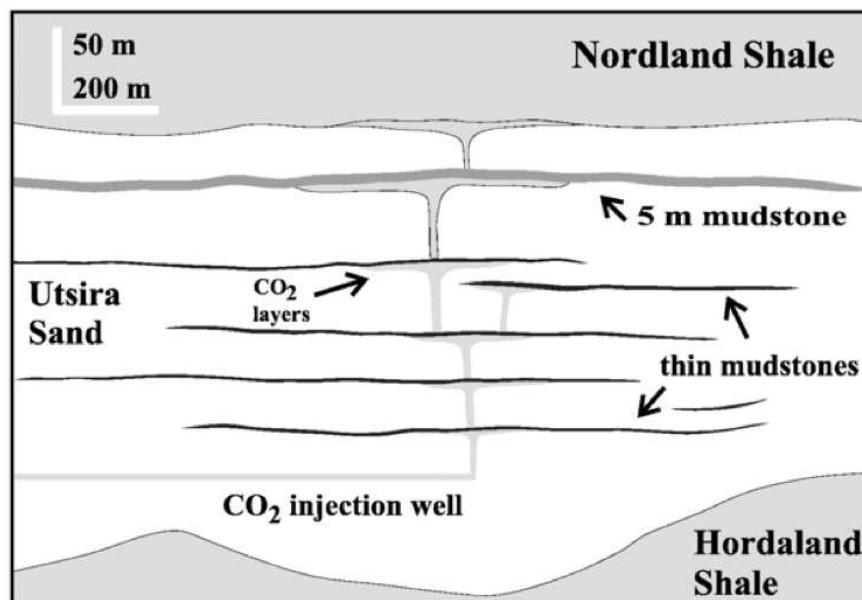


***Figure 6.8:*** *Schematic illustration of carbon dioxide sequestration at the Sleipner field, Norway. Carbon dioxide is injected at a single position in the aquifer but subsequently splits into several currents spreading beneath thin mudstone layers. Figure taken from Bickle* et al. *(2007).*
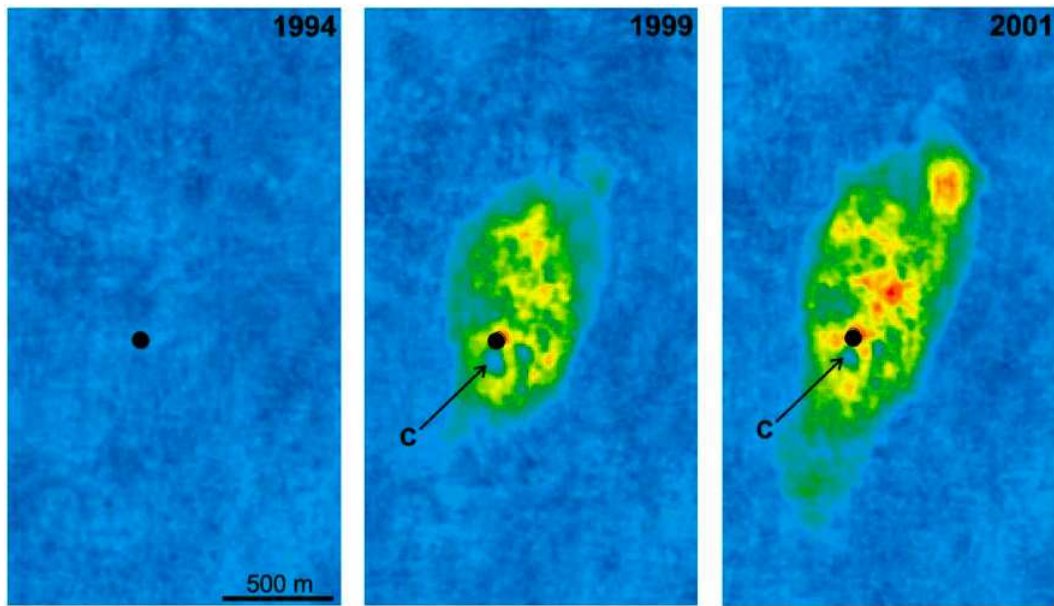
**Figure 6.9:** *Seismic maps showing the lateral extent of spread of a carbon dioxide current in the Sleipner field in the years 1999 and 2001 as compared to the natural state measured in 1994. The black dot shows the position at which carbon dioxide was injected, which is distinct from the 'chimney' at* C *through which most of the carbon dioxide rises. Colours show the absolute reflection amplitude: blue corresponds to low reflectivity (no carbon dioxide); red corresponds to high reflectivity (significant carbon dioxide). Figure taken from Chadwick* et al. *(2005).*

*et al.*, 2005). Since 1996, around $10^9$ kg of liquid $CO_2$ has been pumped annually into the Utsira sand. The Utsira sand is a saline sandstone aquifer approximately 200 m deep and also contains a series of thin, relatively impermeable mudstone layers, as shown schematically in figure 6.8. Since the density of the liquid carbon dioxide lies in the range $500 \pm 150$ kg m$^{-3}$ (Chadwick *et al.*, 2005), it is buoyant with respect to the interstitial salt water and so rises up through the aquifer until it encounters a relatively impermeable mudstone layer. The presence of these mudstone layers causes the single input flux to separate into around ten independent currents propagating within different horizons of the permeable layer. Each of these currents has a volume flux lying in the region $0.002 \lesssim q \lesssim 0.03$ m$^3$ s$^{-1}$ and spreads beneath the corresponding mudstone until it is able to penetrate and form a $CO_2$ plume.

Using seismic techniques, Chadwick *et al.* (2005) and Bickle *et al.* (2007) were able to deduce the lateral extent of the carbon dioxide current in the years 1999, 2001 and 2002. Typical results of these measurements (see figure 6.9) illustrate that the carbon dioxide does not spread axisymmetrically but rather develops a reasonably pronounced asymmetry. The cause of this asymmetry is unknown but it is possible that it is caused by small variations in the slope of the overlying mudstones. Based on the highly simplified analysis presented in this chapter, we expect that such an asymmetry would develop over the time

scale $t^*$. It is difficult to estimate the value of $t^*$ in carbon sequestration because of the uncertainties in the properties of the sandstone and the ambient temperature. However, Bickle *et al.* (2007) give typical measured values for the porosity and permeability of $0.7 \leq k \leq 5 \times 10^{-12}$ m$^2$ and $\phi = 0.31 \pm 0.04$ as well as the $CO_2$ viscosity, $\mu = 3.5 \pm 0.5 \times 10^{-5}$ Pa s. Combining these values with the measured current fluxes, $0.002 \lesssim q \lesssim 0.03$ m$^3$ s$^{-1}$, we can estimate upper and lower bounds on the value of $t^*$. When $\theta = 1°$, we find that $0.03 \leq t^* \leq 14.2$ years. This suggests that the effects of asymmetric spreading is likely to be observable on the time scale of the Sleipner field's operation if $\theta = 1°$.

In obtaining the above estimate of $t^*$, we assumed that $\theta = 1°$. This is based on estimates that $\theta \lesssim 2°$, although it is not possible to measure the relevant slopes accurately (Mike Bickle, personal communication). The uncertainty in the slope and variations in slope inherent in any geological setting mean that the dependence of $t^*$ on $\theta$ is of interest. We find that for $\theta \ll 1$ (measured in radians), $t^* \sim \theta^{-4/(3-\alpha)}$ so that with constant pumping rate ($\alpha = 1$) $t^* \sim \theta^{-2}$: the precise value of the time scale over which the current becomes asymmetric depends sensitively on $\theta$.

It is also interesting to note that the area of the current in contact with the sloping boundary is larger in the case of an asymmetric current than for an axisymmetric current of the same volume. This suggests that an asymmetric current is more likely to find any faults in the cap rock that forms the sloping boundary, and so an asymmetric current is apparently more likely to escape from beneath the cap rock. Determining the degree of
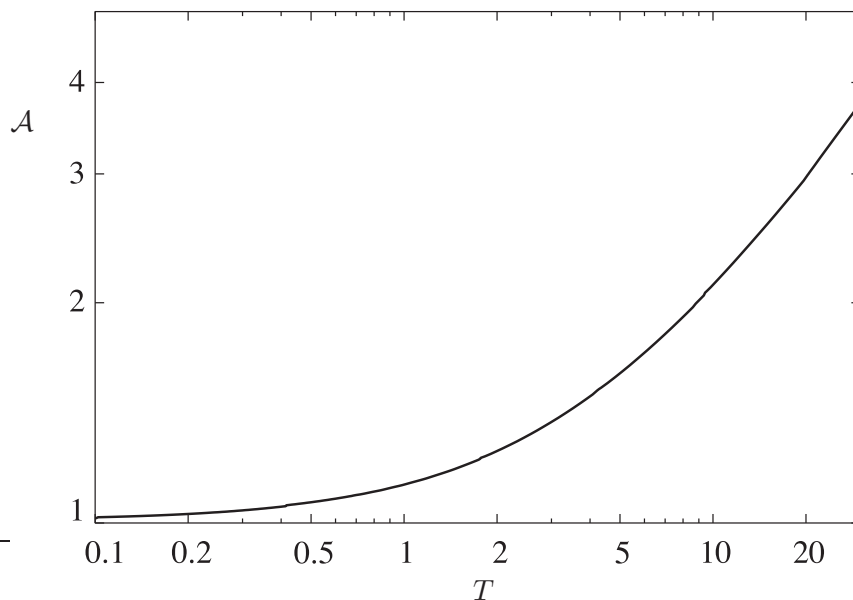


***Figure 6.10:*** *Predictions of the aspect ratio of the current as a function of time based on numerical simulations for a constant flux current ($\alpha = 1$).*

asymmetry of the current is therefore of primary importance. Mike Bickle (Department of Earth Sciences) has measured the aspect ratio, $\mathcal{A}$, of the spreading currents in Sleipner using seismic images similar to those shown in figure 6.9. His data do not show any systematic variation in this aspect ratio over time, but do show that 2000 days after the initiation of pumping $1.5 \lesssim \mathcal{A} \lesssim 2.5$. Figure 6.10 shows the dependence of aspect ratio on time determined from our numerical simulations in the case $\alpha = 1$. This shows that to obtain $1.5 \lesssim \mathcal{A} \lesssim 2.5$ would require $4 \lesssim T \lesssim 13.5$ assuming that the asymmetry is caused only by the presence of a sloping cap rock. This allows us to estimate that $0.4 \lesssim t^* \lesssim 1.4$ years, which is consistent with the estimate of $t^*$ based on the measured parameter values. It therefore seems likely that the different spreading regimes discussed in this chapter are already being observed in the field.

Since injection occurs into confined layers of sediment, estimates for the vertical scale of the current, $h^*$, are also important. Interestingly, $h^*$ is independent of $\theta$ for $\theta \ll 1$ and $\alpha = 1$ so that, with the parameter values given above, we find $1.2 \leq h^* \leq 25$ m. Typically, the layer thickness in the Sleipner field is around 50 m (Bickle *et al.*, 2007). We therefore expect that, near the source, the depth of the sediment layer may be similar to that of the current (and so exchange, confined flows may become significant). However, we expect that the scaling $H \sim T^{-1/3}$ valid away from the source ensures that the present study will remain valid downstream.

## Appendix 6.A  A generalization of (6.9)

In this appendix, we consider some of the scaling properties of the solutions to the equation

$$\frac{\partial H}{\partial T} = \boldsymbol{\nabla} \cdot (H^n \boldsymbol{\nabla} H) - \frac{\partial H^n}{\partial X}, \tag{6.24}$$

which is to be solved along with the volume conservation constraint

$$\int \int H \; \mathrm{d}Y \; \mathrm{d}X = T^\alpha. \tag{6.25}$$

This is the generalized advection-diffusion system describing spreading on inclined planes and is obtained using thin layer models with a depth dependent flux $Q \sim H^n$. In the case $n = 1$, (6.24) and (6.25) reduce to the system (6.9) and (6.10) studied in this chapter, which describes a gravity current in a porous medium above an impermeable slope. When $n = 3$ the system (6.24) and (6.25) describes a viscous gravity current on a slope (Lister, 1992).

We shall consider in more detail two properties of this generalized advection-diffusion equation that were noted in the main text of the chapter. We shall first show that in the asymmetric spreading phase, the cross-slope extent of the current $Y_{\max} \sim T^{\alpha/3}$, independently of $n$. Secondly, we determine conditions on the constants $\alpha$ and $n$ such that the current spreads asymmetrically at *short* times and axisymmetrically at *long* times.

### 6.A.1  Asymmetric cross-slope extent

Here we show that the cross-slope extent of asymmetric solutions to (6.24) and (6.25) scales as $T^{\alpha/3}$. For a current to spread asymmetrically, $(H^n H_X)_X \ll (H^n)_X$, so that the balances between dominant terms in (6.24) can be expressed in scaling terms as

$$\frac{H}{T} \sim \frac{H^{n+1}}{Y_{\max}^2} \sim \frac{H^n}{X_n}, \tag{6.26}$$

which gives

$$H \sim Y_{\max}^2 X_n^{-1}. \tag{6.27}$$

In scaling terms, the conservation of volume (6.25) may be written $H X_n Y_{\max} \sim T^\alpha$, which, after using (6.27) to eliminate $H$, yields

$$Y_{\max} \sim T^{\alpha/3}, \tag{6.28}$$

independently of $n$. From this analysis, we see that the independence of the scaling (6.28) from $n$ is due to a fortuitous cancellation between the $X_n^{-1}$ factor in (6.27) and the factor of $X_n$ that arises in the conservation of volume.

## 6.A.2 Axisymmetric spreading at long times

Here we consider the conditions on the exponents $\alpha$ and $n$ for which the solutions to (6.24) and (6.25) exhibit axisymmetric spreading at *long times*. To observe axisymmetric spreading, rather than asymmetric downslope spreading, we require $(H^n H_X)_X \gg (H^n)_X$, i.e. $H/X_n \gg 1$, and that $X_n \sim Y_{\max}$. The dominant balance in (6.24) is then between the left hand side and the first term on the right hand side, which shows that

$$X_n^2 \sim H^n T. \tag{6.29}$$

From the conservation of volume, (6.25), we then have

$$T^\alpha \sim X_n Y_{\max} H \sim X_n^2 H \sim H^{n+1} T, \tag{6.30}$$

so that

$$H \sim T^{(\alpha-1)/(n+1)}. \tag{6.31}$$

We require that $H/X_n \gg 1$ to observe axisymmetric spreading, which is equivalent to a condition on time, $T$:

$$T^{(\alpha-1)/(n+1)} \gg T^{n(\alpha-1)/2(n+1)} T^{1/2}. \tag{6.32}$$

From this expression it is a simple matter to show that we observe axisymmetric spreading for $T \gg 1$ if

$$\alpha(2 - n) > 3. \tag{6.33}$$

Conversely, if $\alpha(2 - n) < 3$ we observe axisymmetric spreading when $T \ll 1$.

Substituting $n = 1$ (corresponding to a gravity current in a porous medium) into (6.33), we observe that, as found earlier, long time axisymmetric spreading occurs when $\alpha > 3$. Finally, we note that for $n = 3$ (corresponding to a viscous gravity current) axisymmetric spreading at long times could only be observed if $\alpha < -3$.

# Epilogue

> ...we have found the true Cause of the Natation of those Bodies, which otherwise, as being graver than the Water, would descend to the bottom...
>
> *(Galileo Galilei, Discourse on Floating Bodies, 1612)*

## 7.1 Conclusions

In this thesis we have studied a series of problems aimed at uncovering the fluid mechanical aspects of floating and sinking.

Through the analysis and experiments of Chapters 2 and 3 we have studied when small objects can float at a liquid–fluid interface. We have derived conditions on the density and size of an object for surface tension to support it in equilibrium at the interface. For objects that are small compared to the capillary length $\ell_c$, flotation at relatively large densities is possible because of the force of surface tension acting on the object. This force is related to the length of the contact line, which depends on the surface properties of an object in some geometries but not in others. The surface properties of an object, therefore, can only influence its ability to float in certain geometries. In particular, our analysis shows that the extremely hydrophobic leg coatings observed in water striders and other water-walking arthropods do not significantly increase the load bearing ability of the leg. Instead, we suggested that such a coating reduces the energy required for water striders to remove their leg from the water's surface and hence expedites walking and jumping on the surface. The energy saved by having a super-hydrophobic leg coating is comparable to the

energy expended in jumping and thus represents a significant portion of a water strider's energy budget. It therefore seems likely that this energy saving may have driven water-walking arthropods to evolve super-hydrophobic leg coatings. We have also shown that floating can be a very perilous business for dense objects: even the proximity of another object can be enough to cause both objects to sink. We have quantified the conditions under which this happens and have validated our theoretical results with an experimental investigation of touching strips of stainless steel shim. We then considered the continuum limit of a raft of dense strips touching one another and developed a governing equation for the shape of such a raft. This extended to large deflections the work of Mansfield *et al.* (1997) and allowed us to consider the conditions under which a raft can float. We found that below a threshold raft density, $\mathcal{D} = \sqrt{2}$, a floating raft may have arbitrarily large spatial extent. Rafts with $\mathcal{D} \geq \sqrt{2}$ have a maximum size (dependent on $\mathcal{D}$) above which they cannot float and so sink.

In Chapter 4 we studied the impact of an object onto a liquid interface in situations where the interfacial tension dominates inertial hydrodynamic forces. In particular, we studied the impact of a line mass so that the Weber number, $We = 0$. Within our potential flow formulation we studied the interfacial deformation caused by impact as well as the slowing of the line mass caused by the interfacial deformation. We found a similarity solution, valid at early times, which describes the interfacial deformation and allows us to calculate the slowing of the line mass to leading order in time. We used a boundary integral simulation to study the motion after early times. Using this simulation, we determined (given a line's weight, $W$, and impact speed, $F$) whether it sinks or is captured by the interface. We found that below a critical weight, $W_c(F)$, the line mass is trapped by the interface and floats; above $W_c(F)$ the line mass sinks. The numerically computed value of $W_c(F)$ is consistent with experiments, provided that $We \lesssim 1$. We found that at large impact speeds (such that $We \sim 1$) the theory systematically under-predicts the value of $W_c(F)$: objects are observed to float when theory predicts that they should sink. We attribute this discrepancy to the inertial forces within the liquid, which act to slow the object down and were neglected in our theoretical model. These forces become comparable to the force from surface tension when $We \sim 1$, consistent with where the discrepancy between theory and experiment becomes significant.

The dynamic waterlogging of a porous, floating body was the subject of Chapter 5. We began by developing a one-dimensional model of the waterlogging process, which neglected the flow of liquid into the body through its sides. We solved this model, obtaining analytically an expression for the time taken for a floating body to become sufficiently waterlogged to sink. To investigate the effect of flow into the body through its sides we used a boundary integral simulation of the two-dimensional problem and determined numerically the time at which sinking occurs. As expected, these simulations showed that

waterlogging progresses more rapidly once flow through the sides of a body is accounted for. We then discussed how these results relate to the observation of long-lived pumice rafts after major volcanic eruptions. In particular, we noted that our theory is only in quantitative agreement with laboratory experiments by Whitham & Sparks (1986) if the permeability of pumice used in those experiments was significantly smaller than is normal for pumice.

Finally, in Chapter 6, we studied a problem motivated by the geological sequestration of carbon dioxide in saline aquifers. Seismic surveys show that after injection the carbon dioxide spreads asymmetrically. Our aim was to determine whether this asymmetry might be caused by the presence of a sloping cap rock. We developed a thin layer model of a gravity current in a porous medium bounded by an impermeable sloping boundary and determined the scaling relationships describing the propagation of such a current. In particular, we showed that a constant flux current spreads axisymmetrically for short times but propagates predominantly downslope (with a constant velocity) at later times. We also compared the numerical solutions of our model with a series of experiments. Most importantly, we estimated the time scale, $t^*$, over which downslope spreading develops to be of the order of a few months to years in carbon sequestration. This suggests that the observed asymmetry in spreading may indeed be due to the presence of sloping cap rock.

## 7.2 Future work

Our study of the fluid mechanics of floating and sinking has highlighted a number of areas that warrant further investigation. The most pressing of these is the role of the finite size of an object during impact with an interface. Our theoretical analysis of the impact of a line mass seems to be a reasonable description of the low speed impact of long, thin cylinders. However, there is a significant discrepancy at higher impact speeds, which we believe is where the finite radius of an object becomes significant. To confirm that this discrepancy is due primarily to finite size effects (rather than contact line motion, for example) would require a more detailed numerical model. This might be possible using a modified version of the code developed by Li *et al.* (2005). Such a study would also allow us to assess the importance of the liquid viscosity during impact.

Several recent experiments also pose interesting questions about the dynamics of surface tension dominated impact. In particular, the floating/sinking regime diagram presented in figure 4.9 may need modification to explain the impact of super-hydrophobic spheres. Experiments by Lee & Kim (2007) show that at low impact speeds such spheres are trapped at the surface, just as we have found for line masses. However, at higher impact

speeds they 'bounce' clear of the surface. Finally, at still higher impact speeds, super-hydrophobic spheres penetrate the surface and sink. Bouncing is observed only with sufficiently hydrophobic surfaces, i.e. for contact angles $\theta > \theta_c$ for some $\theta_c$. Furthermore, $\theta_c$ appears to depend on the liquid viscosity, though this has not yet been quantified experimentally. Understanding this behaviour is important both for our understanding of wetting phenomena as well as being of use in practical applications. Such an understanding may also provide an alternative explanation for the super-hydrophobicity of the legs of water-walking arthropods.

Many of the applications that motivated our work rely on an object remaining at a liquid–fluid interface. Sinking is undesirable in such applications. In other situations it is floating that is undesirable and we might instead ask: how can we make moving through the interface as easy as possible? For example, what shape should the edge of a thin disk be to minimize the density at which sinking occurs? Using the ideas developed in Chapter 2 we would expect that the disk that sinks at the lowest density should have the minimum contact line length per unit area — i.e. it should be a circular disk. However, in Chapter 3 we saw that interactions between solid edges can induce sinking. We might therefore expect that some sort of star-shaped disk would be easiest to sink: the edges can 'feel' one another without too much extra contact line length being introduced. We also expect that the presence of sharp corners in an object may reduce the maximum density for which the object is able to float. An analysis of this problem could perhaps build on the work of King *et al.* (1999) who determined the asymptotic properties of interface shapes in the vicinity of a sharp corner. Both the interactions between edges and the presence of sharp corners suggest that this problem may be similar to the optimal faucet problem studied
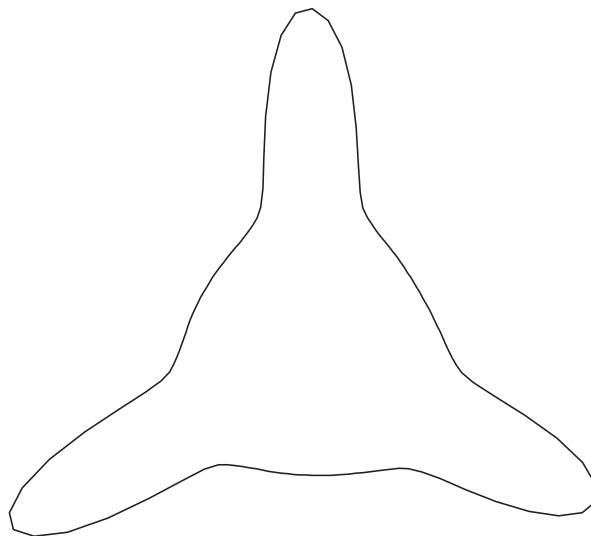


*Figure 7.1:* *The cross-section of a tap that leads to the smallest possible drop size (taken from Chen & Brenner, 2004).*

by Chen & Brenner (2004). They found that a tap with the cross-section shown in figure 7.1 minimizes the volume of droplets produced. It is likely that the two-dimensional disk that is easiest to sink will have a shape qualitatively similar to that shown in figure 7.1.

There is also much theoretical work required to understand the fluid mechanical aspects of other problems that bear a resemblance to those studied in this thesis. Take, for example, the attachment of particles to bubble surfaces during froth flotation (see the review by Nguyen *et al.*, 2006). In many ways this is the reverse of the surface tension dominated impact problem studied in this thesis: a particle approaches an interface from the liquid phase and may get trapped at the air–liquid interface or bounce off and remain in the liquid. Which of these scenarios is realized depends on how fast the liquid between the particle and the interface drains. We might therefore expect the interaction to be controlled by a lubricating layer between the particle and the interface. However, the effect of such a layer does not appear to be included in the current models of collisions between particles and bubbles (Dai *et al.*, 2000).

# Bibliography

ABRAMOWITZ, M. & STEGUN, I. A. 1964 *Handbook of Mathematical Functions with Formulas, Graphs, and Mathematical Tables*. New York: Dover.

ACTON, J. M., HUPPERT, H. E. & WORSTER, M. G. 2001 Two-dimensional viscous gravity currents flowing over a deep porous medium. *J. Fluid Mech.* **440**, 359–380.

BATCHELOR, G. K. 1967 *An Introduction to Fluid Dynamics*. Cambridge University Press.

BEAMENT, J. & CORBET, S. A. 1981 Surface properties of *Culex pipiens pipiens* eggs and the behaviour of the female during egg-raft assembly. *Physiol. Entomol.* **6**, 135–148.

BEAR, J. 1988 *Dynamics of Fluids in Porous Media*. Dover.

BICKLE, M., CHADWICK, A., HUPPERT, H. E., HALLWORTH, M. A. & LYLE, S. 2007 Modelling carbon-dioxide accumulation at Sleipner: Implications for underground carbon storage. *Earth Planet. Sci. Lett.* **255**, 164–176.

BILLINGHAM, J. & KING, A. C. 1995 The interaction of a moving fluid/fluid interface with a flat plate. *J. Fluid Mech.* **296**, 325–351.

BINKS, B. P. & HOROZOV, T. S. 2006 Colloidal particles at liquid interfaces: An introduction. In *Colloidal Particles at Liquid Interfaces* (ed. B. P. Binks & T. S. Horozov), pp. 1–74. Cambridge University Press.

BIRKHOFF, G. & ZARANTONELLO, E. H. 1957 *Jets, Wakes and Cavities*. New York: Academic.

BOWDEN, N., TREFORT, A., CARBECK, J. & WHITESIDES, G. M. 1997 Self-assembly of mesoscale objects into ordered two-dimensional arrays. *Science* **276**, 233–235.

BRAGG, L. & NYE, J. F. 1947 A dynamical model of a crystal structure. *Proc. R. Soc. London A* **190**, 474–481.

BRYAN, S., COOK, A., EVANS, J., COLLS, P., WELLS, M., LAWRENCE, M., JELL, J., GREIG, A. & LESLIE, R. 2004 Pumice rafting and faunal dispersion during 20012002 in the southwest pacific: record of a dacitic submarine explosive eruption from tonga. *Earth Planet. Sci. Lett.* **227**, 135–154.

BUSH, J. W. M. & HU, D. L. 2006 Walking on water: Biolocomotion at the interface. *Annu. Rev. Fluid Mech.* **38**, 339–369.

BUSH, J. W. M., HU, D. L. & PRAKASH, M. 2007 The integument of water-walking arthropods: Form and function. *Adv. Insect Physiol.* To Appear.

CHADWICK, R. A., ARTS, R. & EIKEN, O. 2005 4D seismic imaging of a $CO_2$ plume. In *Petroleum Geology: North-West Europe and Global Perspectives—Proceedings of the 6th Petroleum Geology Conference* (ed. A. G. Doré & B. A. Vining), pp. 1385–1399. The Geological Society, London.

CHEN, H. H. & BRENNER, M. P. 2004 The optimal faucet. *Phys. Rev. Lett.* **92**, 166106.

CHOI, I. S., WECK, M., XU, B., JEAN, N. L. & WHITESIDES, G. M. 2000 Mesoscopic, templated self-assembly at the fluid–fluid interface. *Langmuir* **16**, 2997–2999.

CHRISTOPHERS, S. R. 1945 Structure of the *Culex* egg-raft in relation to function (Diptera). *Trans. R. Ent. Soc. Lond.* **95**, 25–34.

CLAUSER, C. & KIESNER, S. 1987 A conservative, unconditionally stable, second-order, three-point differencing scheme for the diffusion-convection equation. *Geophys. J. R. Astr. Soc.* **91**, 557–568.

CORLESS, R. M., GONNET, G. H., HARE, D. E. G., JEREY, D. J. & KNUTH, D. E. 1996 On the Lambert $W$ function. *Adv. Comput. Math.* **5**, 329–359.

DAI, Z., FORNASIERO, D. & RALSTON, J. 2000 Particle-bubble collision models — a review. *Adv. Colloid Interface Sci.* **85**, 231–256.

DUEZ, C., YBERT, C., CLANET, C. & BOUCQUET, L. 2007 Making a splash with water repellency. *Nature Phys.* **3**, 180–183.

FINN, R. 1986 *Equilibrium Capillary Surfaces*. Springer (Berlin).

GAO, X. & JIANG, L. 2004 Water-repellent legs of water striders. *Nature* **432**, 36.

GAUDET, S. 1998 Numerical simulation of circular disks entering the free surface of a fluid. *Phys. Fluids* **10**, 2489–2499.

Glasheen, J. W. & MacMahon, T. A. 1996a A hydrodynamical model of locomotion in the basilisk lizard. *Nature* **380**, 340–342.

Glasheen, J. W. & MacMahon, T. A. 1996b Vertical water entry of disks at low Froude numbers. *Phys. Fluids* **8**, 2078–2083.

Greenhow, M., Vinje, T., Brevig, P. & Taylor, J. 1982 A theoretical and experimental study of the capsize of Salter's duck in extreme waves. *J. Fluid Mech.* **118**, 221–239.

Grzybowski, B. A., Bowden, N., Arias, F., Yang, H. & Whitesides, G. M. 2001 Modeling of menisci and capillary forces from the millimeter to the micrometer size range. *J. Phys. Chem. B* **105**, 404–412.

Hesla, T. I. & Joseph, D. D. 2004 The maximum contact angle at the rim of a heavy floating disk. *J. Colloid Interface Sci.* **279**, 186–191.

Heyligers, P. C. 2001 Dispersal and monoecy in *Atriplex cinerea* (Chenopodiaceae). *Aus. J. Bot.* **49**, 501–508.

Hinch, E. J. 1990 *Perturbation Methods*. Cambridge University Press.

Hu, D. L. 2006 The hydrodynamics of water-walking insects and spiders. PhD thesis, MIT.

Hu, D. L., Chan, B. & Bush, J. W. M. 2003 The hydrodynamics of water strider locomotion. *Nature* **424**, 663–666.

Huppert, H. E. 1982 The propagation of two-dimensional and axisymmetric viscous gravity currents over a rigid horizontal surface. *J. Fluid Mech.* **121**, 43–58.

Huppert, H. E. 2006 Gravity currents: A personal perspective. *J. Fluid Mech.* **554**, 299–322.

Huppert, H. E. & Woods, A. W. 1995 Gravity-driven flows in porous layers. *J. Fluid Mech.* **292**, 55–69.

Johnson, W. 1998 Ricochet of non-spinning projectiles, mainly from water. *Int. J. Impact Engng* **21**, 15–24.

Jokiel, P. L. 1989 Rafting of reef corals and other organisms at Kwajalein Atoll. *Mar. Biol.* **101**, 483–493.

von Kármán, T. 1929 The impact of seaplane floats during landing. *Tech. Rep.*. N. A. C. A.

KELLER, J. B. 1998 Surface tension force on a partly submerged body. *Phys. Fluids* **10**, 3009–3010.

KELLER, J. B. & MIKSIS, M. J. 1983 Surface tension driven flows. *SIAM J. Appl. Math.* **43**, 268–277.

KING, J. R., OCKENDON, J. R. & OCKENDON, H. 1999 The Laplace–Young equation near a corner. *Q. Jl. Mech. Appl. Math.* **52**, 73–97.

KLUG, C. & CASHMAN, K. V. 1996 Permeability development in vesiculating magmas: Implications for fragmentation. *Bull. Volcanol.* **58**, 87–100.

KOROBKIN, A. A. 1996 Water impact problems in ship hydrodynamics. In *Advances in Marine Hydrodynamics* (ed. M. Ohkusu), pp. 323–371. Southampton: Computational Mechanics Publications.

KOROBKIN, A. A. & PUKHNACHOV, V. V. 1988 Initial stage of water impact. *Annu. Rev. Fluid Mech.* **20**, 159–185.

KRALCHEVSKY, P. A. & NAGYAMA, K. 2000 Capillary interactions between particles bound to interfaces, liquid films and biomembranes. *Adv. Colloid Interface Sci.* **85**, 145–192.

LAGO, M. & ARAUJO, M. 2001 Capillary rise in porous media. *J. Colloid Interface. Sci.* **234**, 35–43.

LEE, D.-G. & KIM, H.-Y. 2007 Impact of a superhydrophobic sphere onto water. *Phys. Rev. Lett.* In Preparation.

LEPPINEN, D. & LISTER, J. R. 2003 Capillary pinch–off in inviscid fluids. *Phys. Fluids* **15**, 568–578.

LI, J., HESSE, M., ZIEGLER, J. & WOODS, A. W. 2005 An Arbitrary Lagrangian Eulerian method for moving-boundary problems and its application to jumping over water. *J. Comp. Phys.* **208**, 289–314.

LISTER, J. R. 1992 Viscous flows down an inclined plane from point and line sources. *J. Fluid Mech.* **242**, 631–653.

LO, L. L. 1983 The meniscus on a needle — a lesson in matching. *J. Fluid Mech.* **132**, 65–78.

LONGUET-HIGGINS, M. S. & COKELET, E. D. 1976 The deformation of steep surface waves on water. I: A numerical method of computation. *Proc. R. Soc. London A* **350**, 1–26.

LYLE, S., HUPPERT, H. E., HALLWORTH, M. A., BICKLE, M. & CHADWICK, A. 2005 Axisymmetric gravity currents in a porous medium. *J. Fluid Mech.* **543**, 293–302.

MANSFIELD, E. H., SEPANGI, H. R. & EASTWOOD, E. A. 1997 Equilibrium and mutual attraction or repulsion of objects supported by surface tension. *Phil. Trans. R. Soc. Lond. A* **355**, 869–919.

MANVILLE, V., WHITE, J. D. L., HOUGHTON, B. F. & WILSON, C. J. N. 1998 The saturation behaviour of pumice and sedimentological implications. *Sediment. Geol.* **119**, 5–16.

MCBIRNEY, A. R. & WILLIAMS, H. 1969 Floating pumice as a means of biological dispersion. *Mem. Geol. Soc. Am.* **118**, 113–116.

MILNE-THOMSON, L. M. 1949 *Theoretical Hydrodynamics*. MacMillan.

NGUYEN, A. V., PUGH, R. J. & JAMESON, G. J. 2006 Collection and attachment of particles by air bubbles in froth flotation. In *Colloidal Particles at Liquid Interfaces* (ed. B. P. Binks & T. S. Horozov), pp. 328–382. Cambridge University Press.

NICOLSON, M. M. 1949 The interaction between floating particles. *Proc. Camb. Philos. Soc.* **45**, 288–295.

OĞUZ, H. N. & PROSPERETTI, A. 1990 Bubble entrainment by the impact of drops on liquid surfaces. *J. Fluid Mech.* **219**, 143–179.

PEPERZAK, L., COLIJN, F., KOEMAN, R., GIESKES, W. W. C. & JOORDENS, J. C. A. 2003 Phytoplankton sinking rates in the Rhine region of freshwater influence. *J. Plankton Res.* **25**, 365–383.

PHILIP, J. R. 1969 Theory of infiltration. *Adv. Hydrosci.* **5**, 215–305.

PRESS, W. H., FLANNERY, B. P., TEUKOLSKY, S. A. & VETTERLING, W. T. 1992 *Numerical Recipes in FORTRAN 77: The Art of Scientific Computing*. Cambridge University Press.

PREUSS, M. & BUTT, H. J. 1998 Measuring the contact angle of individual colloidal particles. *J. Colloid Interface Sci.* **208**, 468–477.

RAPACCHIETTA, A. V. & NEUMANN, A. W. 1977 Force and free-energy analyses of small particles at fluid interfaces. II: Spheres. *J. Colloid Interface Sci.* **59**, 555–567.

RAPACCHIETTA, A. V., NEUMANN, A. W. & OMENYI, S. N. 1977 Force and free-energy analyses of small particles at fluid interfaces. I: Cylinders. *J. Colloid Interface Sci.* **59**, 541–554.

SAIF, T. A. 2002 On the capillary interaction between solid plates forming menisci on the surface of a liquid. *J. Fluid Mech.* **473**, 321–347.

SCHELUDKO, A., TOSHEV, B. V. & BOJADJIEV, T. 1976 Attachment of particles to a liquid surface (capillary theory of flotation). *J. Chem. Soc. Faraday Trans. I* **72**, 2815–2828.

SIEROU, A. & LISTER, J. R. 2004 Self-similar recoil of inviscid drops. *Phys. Fluids* **16**, 1379–1394.

SINGH, P. & HESLA, T. I. 2004 The interfacial torque on a partially submerged sphere. *J. Colloid Interface Sci.* **280**, 542–543.

SUTER, R. B. 2003 Trichobothrial mediation of an aquatic escape response: Directional jumps by the fishing spider, *Dolomedes triton*, foil frog attacks. *J. Insect Sci.* **3**, 19.

SUTER, R. B. & GRUENWALD, J. 2000 Predator avoidance on the water surface? Kinematics and efficacy of vertical jumping by *Dolomedes* (Araneae, Pisauridae). *J. Arachnol.* **28**, 201–210.

SYMONDS, G. J. 1888 *The Eruption of Krakatoa and Subsequent Phenomena, Report of the Krakatoa Committee of the Royal Society*. Harrison and Sons.

TSAI, W.-T. & YUE, D. K. P. 1996 Computation of nonlinear free-surface flows. *Annu. Rev. Fluid Mech.* **28**, 249–278.

VAUGHAN, R. G., ABRAMS, M. J., HOOK, S. J. & PIERI, D. C. 2007 Satellite observations of new volcanic island in Tonga. *EOS Trans. AGU* **88**, 37–41.

VÁZQUEZ, G., ALVAREZ, E. & NAVAZA, J. M. 1995 Surface tension of alcohol + water from 20 to 50 °C. *J. Chem. Eng. Data* **40**, 611–614.

VELLA, D., AUSSILLOUS, P. & MAHADEVAN, L. 2004*a* Elasticity of an interfacial particle raft. *Europhys. Lett.* **68**, 212–218.

VELLA, D. & HUPPERT, H. E. 2006 Gravity currents in a porous medium at an inclined plane. *J. Fluid Mech.* **555**, 353–362.

VELLA, D. & HUPPERT, H. E. 2007 The waterlogging of floating objects. *J. Fluid Mech.* **585**, 245–254.

VELLA, D., KIM, H.-Y. & MAHADEVAN, L. 2004*b* The wall-induced motion of a floating flexible train. *J. Fluid Mech.* **502**, 89–98.

VELLA, D., LEE, D.-G. & KIM, H.-Y. 2006*a* The load supported by small floating objects. *Langmuir* **22**, 5979–5981.

VELLA, D., LEE, D.-G. & KIM, H.-Y. 2006b Sinking of a horizontal cylinder. *Langmuir* **22**, 2972–2974.

VELLA, D. & MAHADEVAN, L. 2005 The 'Cheerios effect'. *Am. J. Phys.* **73**, 814–825.

VELLA, D. & METCALFE, P. D. 2007 Surface tension dominated impact. *Phys. Fluids* **19**, 072108.

VELLA, D., METCALFE, P. D. & WHITTAKER, R. J. 2006c Equilibrium conditions for the floating of multiple interfacial objects. *J. Fluid Mech.* **549**, 215–224.

VINJE, T. & BREVIG, P. 1981 *Breaking Waves on Finite Water Depths: A Numerical Study*. Ship Research Institute of Norway.

VOGEL, S. 2004 Living in a physical world I: Two ways to move material. *J. Biosci.* **29**, 391–397.

WASHBURN, E. W. 1921 The dynamics of capillary flow. *Phys. Rev.* **17**, 273–283.

WHITESIDES, G. M. & BONCHEVA, M. 2002 Beyond molecules: Self-assembly of mesoscopic and macroscopic components. *Proc. Natl. Acad. Sci. USA* **99**, 4769–4774.

WHITESIDES, G. M. & GRZYBOWSKI, B. 2002 Self-assembly at all scales. *Science* **295**, 2418–2421.

WHITHAM, A. G. & SPARKS, R. S. J. 1986 Pumice. *Bull. Volcanol.* **48**, 209–223.

WIGGLESWORTH, V. B. 1966 *Insect Physiology*. New York: Wiley.

WINCHESTER, S. 2003 *Krakatoa: The Day The World Exploded*. London: Penguin.

WOODS, A. W. 1999 Liquid and vapour flow in superheated rock. *Annu. Rev. Fluid Mech.* **31**, 171–199.